Analysis and Design of Ultra-Wideband Antennas in the Spectral and Temporal Domains

THÈSE N^{O} 4719 (2010)

PRÉSENTÉE LE 4 JUIN 2010

À LA FACULTÉ SCIENCES ET TECHNIQUES DE L'INGÉNIEUR
LABORATOIRE D'ÉLECTROMAGNÉTISME ET ACOUSTIQUE
PROGRAMME DOCTORAL EN GÉNIE ÉLECTRIQUE

ÉCOLE POLYTECHNIQUE FÉDÉRALE DE LAUSANNE

POUR L'OBTENTION DU GRADE DE DOCTEUR ÈS SCIENCES

PAR

Gabriela QUINTERO DÍAZ DE LEÓN

acceptée sur proposition du jury:

Prof. T. Ebrahimi, président du jury
Prof. A. Skrivervik Favre, directrice de thèse
Prof. Ö. A. Civi, rapporteur
Dr C. Dehollain, rapporteur
Prof. M. Mazanek, rapporteur

ÉCOLE POLYTECHNIQUE
FÉDÉRALE DE LAUSANNE
Suisse
2010

Abstract

Formal research on Ultra-wideband (UWB) technology started in the U.S. in 2002; where its definition was formulated and the frequency allocation in that country established. However, the first ultra-wideband transmission was done during the confirmation of Maxwell's equations by Heinrich Hertz in 1886, the first ever reported radio transmission. Sparks or very short pulses were sent and received at a distance away from its source. UWB antennas have existed since those times, but technology has been mostly focused on the transmission of continuous wave narrowband signals.

The largest problematic encountered in today's UWB antennas is that characterization methods were, since the beginning, meant to describe narrowband antennas. The frequency characteristics of these antennas are constant over their operational bandwidth, hence they can be fully characterized in the frequency domain. UWB antennas, on the other hand, are meant to transmit pulsed signals. Analyzing them only in the frequency domain is not enough to fully evaluate their performance, as pulse distortion is an important parameter that should be controlled. An extended literature review is included in the first part of this thesis, where the available UWB antenna characterization methods are evaluated. Many limitations were encountered, showing that the available techniques do not analyze simultaneously the most important parameters of an UWB antenna.

A new characterization method is proposed: the System Fidelity Factor (SFF). Its main purpose is to incorporate frequency, time and space characteristics of a two-antennas system to compare UWB antennas in an efficient way. This is achieved with the correlation between the received and the input pulses, quantifying the distortion produced by the system. The SFF is an interesting tool because both simulations and measurements can be done in a simple and straight-forward manner, using tools that are commonly available in any antenna lab. Any combination of antennas can be analyzed and the free-space channel can be easily replaced with any other environment.

Several UWB antennas were designed and used to prove the efficiency of the SFF. A good agreement between the proposed simulation techniques and the measurements was achieved. The antennas are novel designs specially developed for UWB applications under the American or European regulations. The last part of the thesis presents these antennas and analyzes them using the SFF to compare their performance.

Keywords: Ultra-wideband, UWB antennas, antenna characterization, time-domain, pulse distortion.

Résumé

La recherche formelle sur la technologie à Ultra-large bande (ULB) a débuté aux Etats-Unis en 2002 où sa définition et l'allocation des fréquences pour ce pays ont été établis. Néanmoins, la première transmission à bande ultra-large a été effectuée durant la confirmation des équations de Maxwell par Heinrich Hertz en 1886; la première transmission radio reportée dans la littérature. Des impulsions très courtes ont été émises et reçues à une certaine distance de la source. Les antennes ULB ont existé depuis ces temps-ci, mais la technologie s'est principalement concentrée sur la transmission de signaux continus à bande étroite.

Le principal problème des antennes ULB est le fait que les méthodes de caractérisation, depuis les débuts, ont étés dévelopées dans le but décrire le fonctionnement d'antennes à bande étroite. La caractérisation fréquentielle de ces antennes est constante sur leur bande opérationnelle. Elles peuvent donc être totalement définie dans le domaine fréquentiel. Les antennes ULB, au contraire, transmettent des signaux pulsés. Les analyser dans le domaine fréquentiel seulement n'est pas suffisant pour évaluer leur performance, car la distortion du signal est un important paramètre qui devrait être controlé. Dans la première partie de cette thèse, une recherche approfondie de la littérature est donnée. Les méthodes existantes de caractérisation d'antenne ULB y sont évaluées. Beaucoup de limitations ont été trouvées, démontrant que les techniques disponibles ne permettent pas d'analyser simultanément les paramètres les plus importants d'une antenne ULB.

Nous proposons une nouvelle méthode de caractérisation: le System Fidelity Factor (SFF). En incorporant les caractéristiques spectrales, temporelles et spatiales d'un système composé de deux antennes, le SFF permet de comparer efficacement les performances d'antennes ULB. Par une corrélation du signal transmis et reçu, le SFF peut être obtenu. Le SFF est un outil important car les simulations et les mesures peuvent-être effectuées de manière simple et efficace avec du matériel de laboratoire standard. Toutes les combinaisons d'antennes peuvent être analysées et le canal de transmission peut facilement être remplacé et intégré au SFF.

Plusieurs antennes ULB ont été développées pour évaluer le SFF. Un bon accord entre les techniques de simulations proposées et les mesures effectuées en laboratoire a été trouvé. Ces antennes sont de nouvelles architectures spécialement developpées pour des applications soumises aux régulations américaines et européennes. Dans la dernière partie de cette thèse les antennes sont analysées et leurs performances comparées en utilisant le SFF.

Mots-clés: Ultra Large Bande, ULB, antennes ULB, caracterisation des antennes, analyse temporelle, distorsion de signaux pulsés.

Acknowledgements

I would like to thank all the people that were somehow involved in this thesis. Prof. Juan R. Mosig for giving me the opportunity to come to LEMA. My supervisor Prof. Anja Skrivervik for her good advice and supervision over all these research years. J.F. Zürcher for his valuable help to give life to my antennas and for his guidance to make accurate measurements. Eulalia Durussel, for the coffee breaks shared, which motivated me everyday to come early to school. Michael Mattes, for all his good advices.

My appreciation goes to the thesis committee members. The external jury of my thesis Prof. Özlem Civi and Prof. Milos Mazenek, for reading this thesis and giving their approval. Dr. Catherine Dehollian who apart from being the internal jury, was part of the MICS UWB group. A big thank you goes to all the members of this group with whom I grew into the wonderful knowledge of an Ultra-wideband radio. Specially the EPFL people with whom I spent more time having interesting discussions: Jérôme Rousselot, James Colli-Vignarelli, Prakash, Hai Zahn, Ruben Merz and Manuel Flury.

My colleagues at LEMA were important and crucial elements on this work. Huge hugs go to Katarina, Ivica and Pedro, for being a model to follow, in the academic and in the personal. To my roomy Fred, for all his advices, time and patience, and for keeping the door at 45°. To the girls in the lab Laleh, Ruzica and Madda, for all the laughs and good moments spent together. To the Spanish guys, for all the discussions we had together, some more philosophical (coming from Roberto and Edén) and others more rude (from Sergio). To the Italian guys: Francesco, Marco and Gabriele, the Greek guys: Thanos and Ioannis, and to all other LEMA members that are no longer here: Grégoire, Juliane, Olivier. Thanks to all of them for teaching me something new every day, for sharing all these years and for making my time in LEMA unforgettable.

Thanks to all the acousticians, for making the lab more musical. To my first office-mate Thomas, for introducing me into the world of PhD Comics.

To my friends Mario, Alejandra, Magalli, Tatiana y los Luises: Gracias por todo!

To my Martin, for being the reason and for being there always. To his parents and family, for the Sundays spent together and for making me feel like at home: Merci vielmals!

Last but not least, I would like to deeply thank my parents, for teaching me the most important things in life, for all their support and love. To my sisters Malú and Liliana, to my brother Rogelio and to my niece Natalia, for motivating me and always being with me despite the distance. To them all, my family, I dedicate this thesis.

Table of Contents

List of Acronyms

BPSK	Binary Phase Shift Keying
CPS	Coplanar Strip
CPW	Coplanar Waveguide
ECC	Electronic Communications Committee
EIRP	Effective Isotropic Radiated Power
FCC	Federal Communications Commission
FF	Fidelity Factor
FFT	Fast Fourier Transform
FWHM	Full Width at Half Maximum
IEC	International Electrotechnical Commission
IFFT	Inverse Fast Fourier Transform
IR-UWB	Impulse Radio Ultra-wideband
ITU	International Telecommunications Union
MAC	Medium Access Control
MB-OFDM	Multiband Orthogonal Frequency Division Multiplexing
OFDM	Orthogonal Frequency Division Multiplexing
PED	Planar Elliptical Dipole
PHY	Physical Layer
PRF	Pulse Repetition Frequency
PSD	Power Spectral Density
RBW	Resolution Bandwidth
RF	Radio Frequency
Rx	Receiving
SFF	System Fidelity Factor
Tx	Transmitting
UWB	Ultra-wideband
VNA	Vector Network Analyzer
WUSB	Wireless Universal Serial Bus

1. Introduction

Antennas are a fundamental element of today's wireless world. Electromagnetic waves need the correct structure to be transmitted in a reliable manner. An antenna consists usually of conductive parts and may contain dielectric elements too, as it was the case for the radio systems in the beginning of the last century. The exponential advances in technology over the last century have resulted in miniaturized components, increase of information transmitted, higher data rates and almost a complete saturation of the frequency spectrum among others. As technology advances, devices become more complex and antennas need to be smaller.

Ultra-wideband is a clear example of all these technological advances. It tries to mitigate the saturation of the spectrum, transmitting at very low power over a frequency band that is already occupied. Its low power characteristics make it invisible for the radio systems sharing the same spectrum. Its ultra-wideband spectrum allow transmitting information at high data rates, increasing with this the amount of information transmitted per second. However, its implementation is very complex, as the devices work with lower input power and have to be very fast. The antennas should also be able to receive and transmit the ultra-broad spectrum required and be of considerably small size.

Antennas fabricated in planar substrates have been of increased demand. Using this technology, antennas can be of reduced size and easily manufactured. The large variety of substrates in the market allow the designer to choose between different thicknesses, permittivities, materials, etc., to make a specific antenna. Due to all these characteristics, and the vast experience our laboratory has on this technology, the antenna research in this thesis focuses on the implementation of planar antennas.

Until the implementation of UWB technology (and with exception of radar systems), antennas have been characterized mostly in the frequency domain. Standard parameters such as reflection coefficient, gain, radiation efficiency, etc. have been defined for narrowband antennas. This is also evident on the measurement equipment used in antenna analysis, as well as in most of the simulation softwares available today. Measurement equipments like the vector network analyzer (VNA) and the spectrum analyzer work in the frequency domain. Most simulation tools present the results in the frequency domain, even if they use a time-domain technique to compute the fields.

Due to the frequency characteristics of Ultra-wideband technology, the antennas should be analyzed in the time domain as well. One important characteristic of Ultra-wideband technology is the transmission of very short pulses in time having a very broad frequency spectrum. This is therefore a strong motivation to analyze the antennas behavior when transmitting pulsed signals. An antenna should not only be able to radiate over all the

desired frequency band, it should also radiate a pulse without any distortion, or as small distortion as possible.

1.1. Objectives

This study started as part of a project funded by the Swiss National Science Foundation (SNSF) in the MICS Ultra-wideband group. The principal objective was to implement an ad-hoc radio system sending UWB pulses. The antenna design was an important part of the project, as it involved not only the antenna but the radiation of the signal as well, and thus the transmission of the information. Since the application of the project was on ad-hoc networks, the focus was to study and implement omnidirectional antennas. The components of the network will be located in the same plane, but in different positions from each other, mobile or fixed.

The main objective of this thesis is to implement a characterization method for UWB antennas. Different characterization methods available today were studied in detail in order to identify the most important parameters describing UWB antennas. Due to the specific application of the antennas, we were concerned about characterizing them in a complete plane. We soon realized that a single method did not exist which could be used at every angle of radiation and included frequency and time domain characteristics. Furthermore, measurements of the available methods are not always possible to realize using the available equipment, which is typically in frequency domain for antenna analysis.

The new characterization method should analyze the antenna characteristics in the frequency and time domains, as well as over a given plane of radiation (omnidirectional antennas), using the available measurement equipment and simulation tools. Using the latter, an effective comparison between antennas should be performed, which may lead to a proper classification of UWB antennas.

In order to demonstrate the capacity of the method, antennas need to be designed and tested. The second objective of the thesis is then to design novel UWB antennas with excellent omnidirectional performance that could be implemented on planar substrates. The designs are meant to work in the American band regulated by the FCC and/or in the European band established by the ECC. From the designing process, an evaluation of the most important physical characteristics of UWB antennas should be performed and presented as a guidance for future antenna designs.

1.2. Thesis Outline

The chapters of this thesis are summarize in this section. Each chapter contains a literature review which references are presented at the end of the chapter.

Chapter 2: Ultra-wideband Technology

This chapter gives a general introduction of Ultra-wideband technology. It explains

the two main technological approaches used today to cover the UWB band: OFDM and IR-UWB. Some of the main applications of this technology are briefly described. The standards and regulations that rule the technology around the world are specified. A brief description of the spectrum analyzer settings required to measure transmitted power according with the regulations is given.

Chapter 3: Ultra-wideband Antenna Characterization

The chapter starts with a small story about antennas, how they have evolved and when in history the first UWB antenna was used. This helps us understand the differences between conventional antenna characterization and the specific methods that should be applied to UWB antennas. The antenna characteristics that promote a good UWB pulse transmission are described. The calculation of these parameters via measurements and/or simulations is explained. An omnidirectional and a directional antenna are used to exemplify the methods.

Chapter 4: System Fidelity Factor

In this chapter a new characterization method for UWB antennas is presented: the System Fidelity Factor (SFF). Its main purpose is to incorporate frequency and time domain characteristics of an antenna system into a comparison method for UWB antennas. The procedure to derive the SFF is described in detail. Two approaches to calculate the system transfer function are described. The first one uses the antenna effective height in the time domain, while the second approach derives the system transfer function from the Friis transmission equation. Simulation results of a single antenna are combined to obtain the transfer function of the two antenna system. The required post-processing to calculate the received pulse and compare it with the input pulse is explained in detail. Measurements of the SFF are done using a two port VNA. Two examples are given where the UWB performance of three antenna systems are compared. In the first example antenna systems composed of two identical monopoles are studied. In the second example the transmitting antenna is a Vivaldi and the receiving antenna a monopole. The polar representation of the SFF allows an equitable comparison between antennas.

Chapter 5: Novel Antenna Designs

This chapter presents three novel designs of UWB antennas. Their UWB performance is analyzed using the methods described in Chapter 3 and using the proposed method in Chapter 4. The results show that the System Fidelity Factor is an efficient method to compare antennas in any desired plane. Two of the antennas are designed to work in the American FCC band and the last antenna to works in the European ECC band. Designing tips are derived from the designs of the three antennas. The hints are a useful tool for starting a design from the basics, taking in consideration important aspects of UWB antennas.

Chapter 6: Conclusions

This chapter summarizes the thesis and highlights its most important findings. It discusses also the possible future work directions that might be followed, inspired by this thesis.

1.3. Original contributions

The original contributions of this thesis are summarized in this section.

Chapter 3 gives a complete literature overview of the characterization methods for UWB antennas that exist today. The measurements and/or simulations techniques to calculate them are described and exemplified.

Chapter 4 a complete new characterization method is formulated. It is shown to be an excellent method to compare UWB antennas. Simulation and measurement processes are described, which can be done with the most conventional equipment and tools available in any antenna design laboratory. The method to calculate the antenna system transfer function from simulations of one antenna is described for the first time. Short computational time is required and the results match perfectly with measurements of the transmission coefficient using a VNA.

Chapter 5 presents three novel antennas designs, whose UWB characteristics were analyzed. An increase in directivity of UWB dipoles radiation was achieved, which is an important characteristic for applications such as body area networks. Tips and hints were derived from the designing knowledge acquired, they are described at the end of the chapter, and are a useful tool when designing UWB antennas.

2. Ultra-wideband Technology

2.1. Introduction

Antenna analysis and design is a topic that has been used for many dissertations and has fostered many publications. What makes this thesis different is the application that the antennas will have. We cannot start writing about Ultra-wideband antennas without having understood the meaning of Ultra-wideband, what is the technology behind it, which are its applications, how it is regulated and what are the standards that govern it.

This chapter presents Ultra-wideband technology and the different approaches that have been used to cover its requirements. The technology itself would not be important without its implementation, therefore the main applications that have been developed and studied over the past years will be described.

The standards and regulations that norm the use of this technology around the world will be introduced. Every region has a different spectrum allocation for unlicensed Ultra-wideband systems, the main players in these regions will be identified. It is important to have a clear idea of how the technology is ruled, but it is not the center of investigation of this thesis. Therefore, a small introduction on the standards that exist today will be given, focusing on the emitted radiated power and the frequency allocation, as are the factors that are closely related to the antennas.

During these years of research we realized that the correct measurement techniques to fulfil the standards requirements were not clearly understood. In earlier versions of the standards, the meaning of average and peak power was not well defined and created some confusion. Section 2.6 of this chapter deals with this issue by introducing the measurement procedures to obtain the radiated power using a spectrum analyzer, based on spectrum analysis of pulsed signals.

A summary of the chapter is given in the last section, where the most important points to retain for the rest of the document will be emphasized.

2.2. Ultra-wideband Systems

Higher data rates, saturation of the frequency spectrum, low power consumption, etc. are some of the reasons why Ultra-wideband has been of increased interest over the past years. Ultra-wideband (UWB), in comparison with conventional or narrowband systems, uses a large bandwidth to transmit information. The power used over the whole band is much lower than the power used by narrowband systems, as shown in Fig. 2.1(a). Therefore almost no

interference is produced, as the power level transmitted is almost at the noise level of the systems using the same spectrum, making it possible to share the spectrum and space with other established technologies.

The Federal Communications Commission (FCC) first defined UWB as any system having a bandwidth of at least 500 MHz or a fractional bandwidth larger than 0.20. Fractional bandwidth is defined as:

$$bw = 2\frac{f_H - f_L}{f_H + f_L} \tag{2.1}$$

where f_H and f_L are the higher and lower frequencies of operation, respectively. These frequencies are defined as the points where the power is reduced by -10 dB from the frequency with maximum power f_M.

In 2002 the FCC allowed the frequency band between 3.1 and 10.6 GHz for unlicensed Ultra-wideband transmission. The Effective Isotropic Radiated Power (EIRP) should be below -41.3 dBm inside the frequency band. The FCC regulation will be more deeply discussed in Section 2.4.

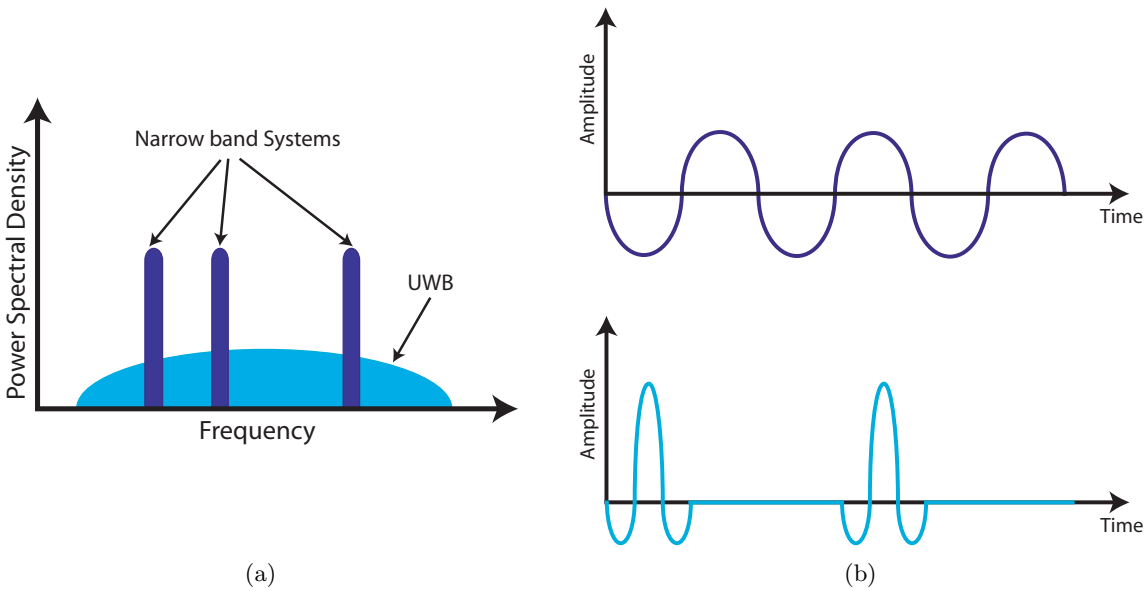

Figure 2.1.: Gain Pattern of Narrow band and Ultrawideband systems: (a) Frequency and, (b) Time domain.

In order to cover the ultra-wide band, two different approaches have been investigated by the industry and academic researchers. The first approach covers the band using several sub-bands and the second consists in sending very narrow pulses having the desired bandwidth. These two methods are described in the following subsections.

2.2.1. MB-OFDM

MultiBand Orthogonal Frequency Division Multiplexing (MB-OFDM) consists on dividing the frequency spectrum in several sub-bands using different carriers. This approach is the more widely used and where the industry has put most of its attention. The WiMedia Alliance [1] was founded in September 2002, just after the FCC assigned the UWB frequency allocations. It has today more than 350 members, among whom are some of the most renown companies, and is maybe the strongest promotor of UWB standardization around the world.

MB-OFDM divides the 7.5 GHz spectrum into 14 bands each having a bandwidth of 528 MHz. The first 12 bands are grouped in 4 band groups consisting of 3 bands each. The last 2 bands form the fifth band group. A last band group (# 6) contains the bands 9-11. Fig. 2.2 shows the frequency allocation of the bands and band groups. In order to transmit the information, OFDM distributes the data over a large number of carriers that are spaced apart at precise frequencies. This method had been widely investigated and it have been implemented by several companies.

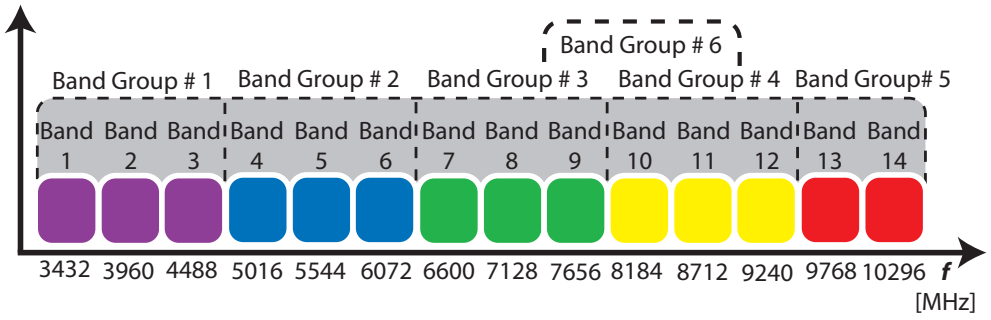

Figure 2.2.: OFDM frequency band plan.

2.2.2. IR-UWB

The broad spectrum in Fig. 2.1(a) can be covered using very short pulses in time, as in Fig. 2.1(b). This type of UWB is called Impulse Radio UWB (IR-UWB) [2], and consists in sending pulses or a group of pulses representing one bit* of a coded signal. The pulses, in order to cover the specifications by the FCC should be at least 2 ns wide (BW = 500 MHz) and have small amplitude (low transmitted power).

This approach is maybe less attractive for the industry, but is the favorite of researchers in universities or investigation centers. Its time dependance promotes the investigation in this domain, extending its complexity on implementation and analysis.

*It is possible to send more complex codes, but for the sake of simplicity we consider the case of binary systems.

2.2.2.1. Modulation

Several modulation techniques are used to send the information of the impulse signal. Among the most studied and with higher possibilities of implementation are the ones shown in Fig. 2.3. A small description of each technique is given below.

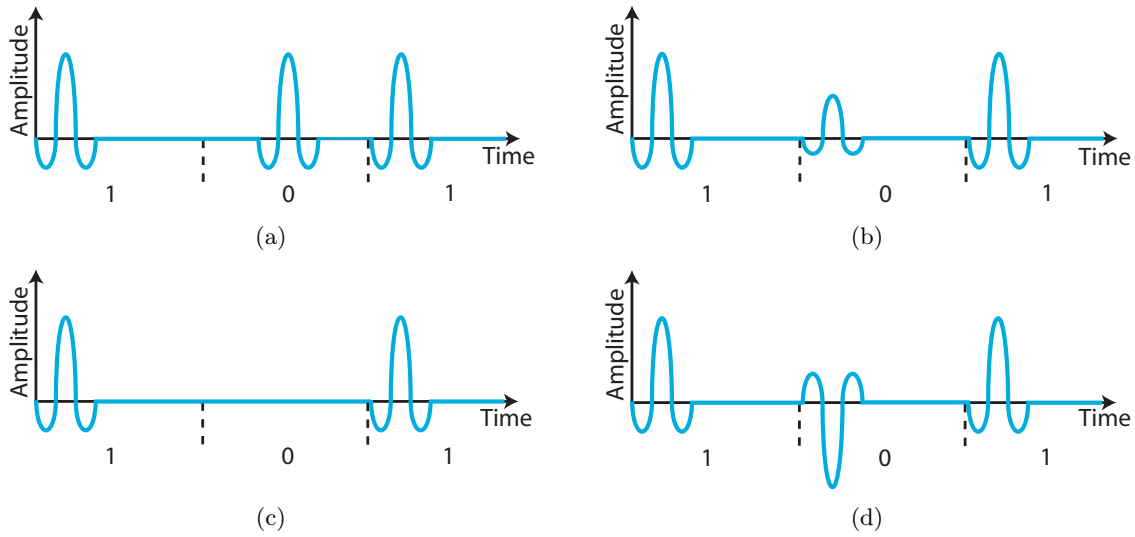

Figure 2.3.: Modulation techniques of IR-UWB: (a) PPM, (b) PAM, (c) OOK, and (d) BPSK.

- **PPM** – Pulse Position Modulation is maybe the most common modulation scheme used for IR-UWB. It consists on sending the pulses at different times, each position representing a different bit value. In Fig. 2.3(a) a 1 is sent at the beginning, whereas the 0 is sent in the middle of the period.
- **PAM** – Pulse Amplitude Modulation uses pulses with different amplitudes, each amplitude is related to a specific bit value. In Fig. 2.3(b) a 1 has a higher amplitude than the bit representing the 0.
- **OOK** – On-Off Keying is maybe the simplest modulation and the less power consuming. A 1 is represented with a pulse, and the 0 is the absence of a pulse, as shown in Fig. 2.3(c).
- **BPSK** – Binary Phase Shift Keying consists on changing the phase of the pulse, according to the bit value to be transmitted. A 1 has 180°phase difference from a 0. Fig. 2.3(d) shows a 1 having positive amplitude and a 0 that has the same magnitude but negative.

More complex modulations could be used, depending on the type of information to be sent or the transceiver to be used. Modulations can be as well used for higher levels of information, and not only binary systems.

2.2.2.2. Pulse shapes

Radar technology have a large experience in UWB pulses [3],[4], generating high power pulses in the order of kV. Low power ultra-wideband waveforms are an important topic of study, from the antenna point of view [5] as well as from the generator approach [6]. The former looking for an optimum pulse to be transmitted without distortion, the latter looking for low power technology that can generate such pulses.

There exist many different types of pulses that can cover the UWB band [7] within the FCC Spectrum mask. The most common pulse shapes known and the ones used in the following sections of this thesis, are described below.

- **Gaussian Signals** – The Gaussian pulse is described by the exponential:

$$T(t) = Ae^{-\frac{t^2}{\tau^2}} \tag{2.2}$$

where A is the amplitude, τ denotes the width of the pulse and t is the duration of the pulse. When τ becomes larger, the pulse width increases. The signal produced by equation (2.2) is a base band pulse, therefore its central frequency is located at 0 Hz.

To move the signal to higher frequencies, the derivative of the pulse needs to be obtained. The signal will have higher frequency when increasing the derivative number n in the following equation:

$$T_n(t) = A\frac{d^n}{dt^n}e^{-\frac{t^2}{\tau^2}} \tag{2.3}$$

Fig. 2.4 shows a gaussian family in time and its corresponding power spectral density. The value of τ is 0.137. The fourth derivative is centered at 6 GHz and has a -10 dB bandwidth between 3 and 10.5 GHz.

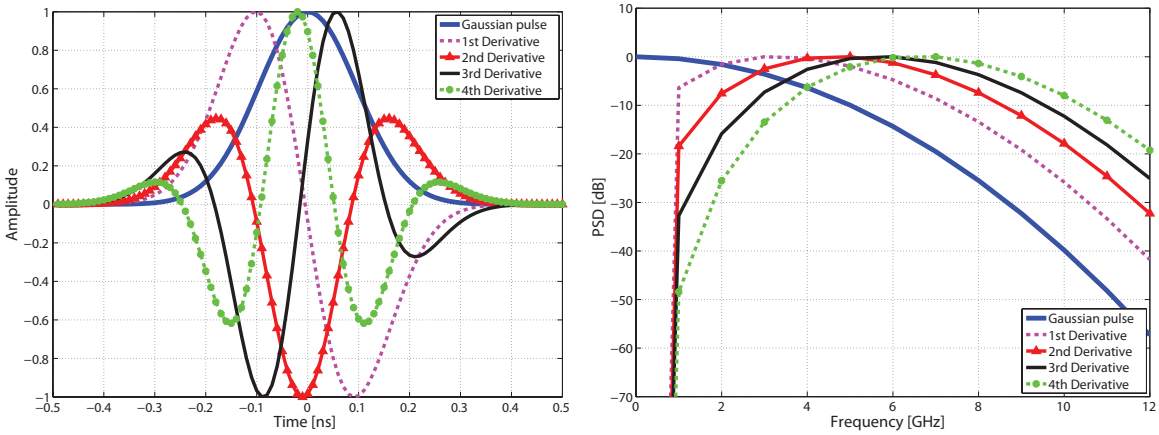

(a) (b)

Figure 2.4.: Modulation techniques of IR-UWB: (a) Time signal, (b) Power spectral density

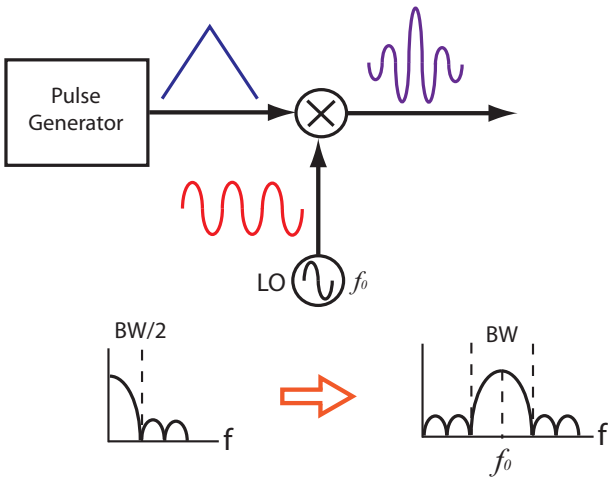

Figure 2.5.: Carrier-based pulse generation.

- **Carrier-Based** – A simple way of generating an UWB pulse is by modulating a baseband pulse [8], up-converting it to the targeted frequency. The baseband pulse is generated by a pulse generator. The pulse is then multiplied with a signal coming from a local oscillator at a frequency equal to the center frequency of the desired pulse. This proceeding and its frequency effect on the signal is shown in Fig. 2.5.

  The shape of the baseband pulse varies depending on the application and simplicity to generate the pulse. The length of the pulse is inversely proportional to the bandwidth of the signal. Triangular or square signals are simple to generate and some integrated circuits have already been implemented which generate this carrier-based approach pulse to cover a 500 MHz bandwidth [9].

  A carrier-based pulse having a 528 MHz bandwidth and modulated with the correct carrier, can represent a band on the MB-OFDM allocation. Meaning that a band group of MB-OFDM can be decomposed using two or three carrier-based pulses.

2.3. Ultra-wideband Applications

Different applications can benefit from the UWB characteristics. Applications can be grouped in four main classes according to [10], which are:

- High-data-rate communications
- Low-data-rate communications
- Imaging
- Automotive radar

Since the approval of UWB technology by the FCC, many applications have been investigated. Its characteristics (low power, narrow pulses, etc.) make it unique and many areas of investigation started to look for the benefits that this technology could bring. Among all the

applications that are studied today, the most innovative and demanded by antenna designers are listed here:

- **WUSB** – Wireless Universal Serial Bus is based on the WiMedia Alliance's Ultra-WideBand (UWB) common radio platform [1], and is capable of sending 480 Mbit/s at distances up to 3 meters and 110 Mbit/s at up to 10 meters. The second generation of these devices (USB 2.0) is already in the market and has been produced by Intel [11]. Due to its small size and large capabilities it has been widely studied in the antenna domain, where many designs have been investigated [12],[13]. This application requires small omnidirectional antennas, where monopoles and dipoles are the most suitable models.
- **UWB Radar Imaging** – is a hot field of study, specially in detection systems of unwanted objects. Ground penetrating radar (GPR) was maybe the first area of study, where its capabilities on landmine detection were of interest to many researchers [14], [15]. Its application on the biomedical domain can highly benefit cancer detection due to its good penetration and resolution characteristics [16],[17], [18]. Its low power radiated makes it less aggressive than X-Rays [19]. Arrays using directional antennas are frequently used, due to its higher gain which means as well a good reflected signal. Patch antenna arrays have as well been of interest [20], mainly due to its reduced size compared to directive antennas.
- **Ranging** – Fine time resolution of UWB signals enables potential applications in high-resolution ranging [21]. Ranging and location awareness is a desirable feature in wireless networks, with applications such as tracking, finding people, safety, emergency, and robotics [22]. Pulse distortion should be avoided as multiple reflections may exist and contribute to its deformation, therefore a good antenna design is fundamental [23]. Antennas for ranging highly depend on the specific purpose of the system. Where ranging has to be done among mobile users, the antenna pattern is expected to be omnidirectional. In other cases, a fix antenna might try to localize a specific user in the space. A directive antenna at the base station and an omnidirectional one at the user would be the optimum antenna configuration.

Other examples of UWB communications include Personal Area Networks (PAN), Wireless Local Area Networks (WLAN), home entertainment, multimedia interfaces and high precision location RFID.

2.4. Regulations

Ultra-wideband may be used to refer to any radio technology having a bandwidth of at least 500 MHz or 20% of the arithmetic center frequency, according to Federal Communications Commission (FCC). In February 14, 2002 a first Report and Order by the FCC authorized the unlicensed use of UWB in the range of 3.1 to 10.6 GHz. The FCC power spectral density emission limit for UWB emitters is -41.3 dBm/MHz inside the UWB band. However, this limits are only valid in the USA, as will be seen in the following sections, but as it was the first

administration to define the term Ultra-wideband, it is common to refer to this definition.

Between 2002 and 2007, several other administrations have adopted unlicensed frameworks for the adoption of UWB communications including Europe and various Asia Pacific nations. These frameworks include the requirement to conform with specific spectral masks and operational conditions in order to protect existing radiocommunication services. Spectrum masks were defined for spectrum limits of UWB system transmission [24]. These masks vary from country to country and they will be as well shown in the following sections.

2.4.1. United States

The United States of America was the first country to develop and release a regulatory framework for the open use of UWB technology. Numerous compatibility studies were carried out to assess the impact of UWB emissions sharing spectrum with other services.

The FCC's First Report and Order, subpart F was created specifically to cover UWB devices. It defines UWB transmitters in the following way [25]: "An intentional radiator that, at any point in time, has a fractional bandwidth equal to or greater than 0.20 or has a UWB bandwidth equal to or greater than 500 MHz, regardless of the fractional bandwidth". The spectrum available is between 3.1GHz to 10.6 GHz for unlicensed UWB communications devices (indoor or hand held) with a maximum power emission limit of -41.3 dBm/MHz. The FCC spectrum mask for UWB communications devices (Fig. 2.6) specifies the allowed limits for indoor and outdoor UWB operation. According to the FCC, this limit ensures the appropriate unlicensed operation of UWB devices without causing interference to existing licensed users of the $3.1 - 10.6$ GHz frequency band. To provide additional protection to GPS users, the FCC has also mandated that spurious emissions between 0.96 GHz and 1.61 GHz be limited to -75 dBm/MHz.

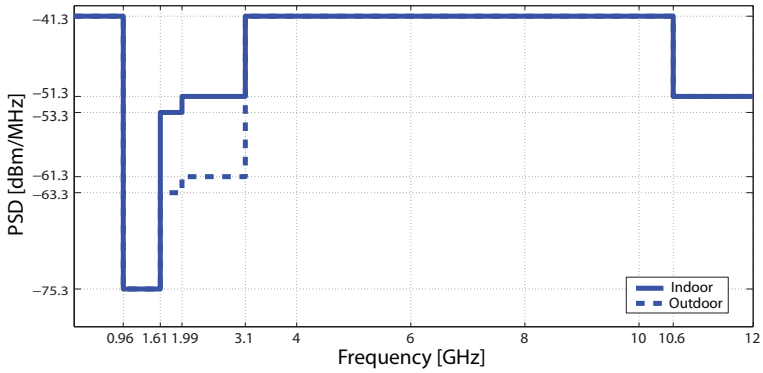

Figure 2.6.: FCC mask for outdoor and indoor UWB applications in the USA.

The peak level emissions contained within a 50 MHz bandwidth centered on the frequency at which the highest radiated emission occurs, f_M is limited to 0 dBm EIRP. It is acceptable to employ a different resolution bandwidth, and a correspondingly different peak emission limit, following the procedures described in Section 2.6 of this thesis.

FCC has published the following documents regarding UWB communication devices under Part 15 and Subpart F [25]:

- 15.501 Scope
- 15.503 Definitions
- 15.505 Cross reference
- 15.507 Marketing of UWB equipment
- 15.517 Technical requirement for indoor UWB devices
- 15.519 Technical requirements for handheld UWB systems
- 15.521 Technical requirements applicable to all UWB devices
- 15.250 Operation of wideband systems within the band $5.925 - 7.250$ GHz

2.4.2. Europe

The ETSI (European Technical Standard Institute) and CEPT (European Conference of Postal and Telecommunications Administration) are the organizations involved in the regulation of UWB in Europe. The Electronic Communications Committee (ECC) of the CEPT conduces UWB compatibility and spectrum sharing studies in order to develop harmonized standards for short range devices using UWB technology. According to the ECC studies, UWB equipment should be used predominantly indoors and thus avoid interference. Equipments must cease transmission within 10 s unless they receive acknowledgement from an associated transceiver that its transmission is being received. The regulations state also that the outdoor use of UWB technology should not include a fixed outdoor location or connected to a fixed outdoor antenna or in vehicles.

The final decision on UWB regulation in Europe was published in February 2007. This decision specifies the final emission limits for UWB communications, makes provisions for the utilization of mitigation techniques including low duty cycle considerations and other operational conditions. The limits are for indoor UWB communication. In order to compare the ECC and FCC limits, both masks are illustrated in Fig. 2.7. It is seen that the European approach to UWB emission is more restrictive than FCC, and only in the $6 - 8.5$ GHz band the emission level is the same as the FCC.

2.4.3. Japan

The preliminary Japanese UWB radiation mask for indoor devices was announced in September 2005. It has two bands: 1) from 3.4 to 4.8 GHz and 2) from 7.25 to 10.25 GHz. Compatibility studies showed that devices operating in the $3.4 - 4.8$ GHz band should use a technology to reduce interference with other radio services. This technology is called Detect And Avoidance (DAA). It is required to ensure the coexistence with existing systems and new services such as 4G systems. For devices not equipped with any interference mitigation techniques, the average power shall be -70 dBm/MHz and the peak power shall be -64 dBm/MHz in the $3.4 - 4.8$ GHz Band [26].

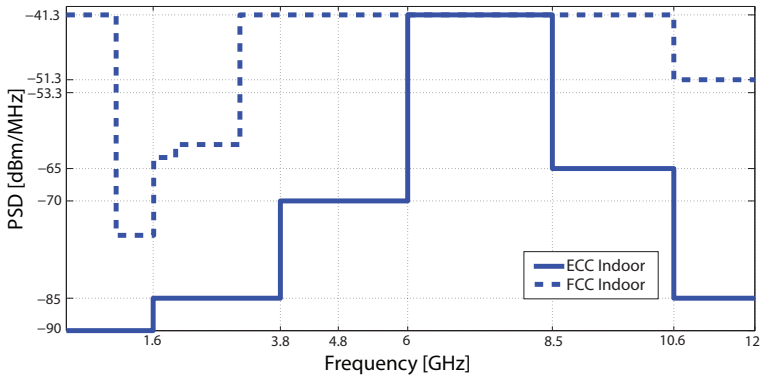

Figure 2.7.: Comparison between the FCC and ECC indoor masks.

The second band ($7.25 - 10.25$ GHz) does not require a DAA. The Japanese UWB emission mask is depicted together with the FCC mask in Fig. 2.8. The average power spectral density is limited to -41.3 dBm/MHz or lower on both bands, similar to the FCC mask. The emission mask is limited to indoor usage, outdoor usage and the 24 GHz band for use in automotive radars is being discussed by Japanese authorities.

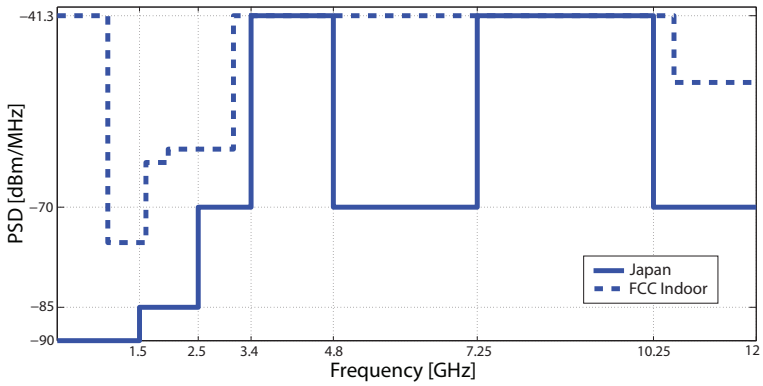

Figure 2.8.: Comparison between the FCC and Japanese indoor masks.

2.4.4. International Telecommunications Union

The International Telecommunications Union Radiocommunication Sector(ITU-R) [27] released in 2006 a series of recommendations on UWB, identifying unlicensed approaches as best suited for UWB communications. The series provide a guidance to administrations on the introduction of UWB communication devices. Following the outcome of a number of study initiatives carried by ITU-R (TG1/8), it has been concluded by the ITU that the introduction of UWB devices is subject to operation on a non-interference and non-protection basis. The published recommendations are:

- **SM.1754: Measurements techniques of ultra-wideband transmissions.** Rec-

ommends measurement techniques of UWB signals in the frequency domain and in the time domain.

- **SM.1755: Characteristics of ultra-wideband technology.** Provides the terms and definitions employed in UWB technology, as well as information on technical and operational characteristics of UWB.
- **SM.1756: Framework for the introduction of devices using ultra-wideband technology.** Provides guidance to administrations when considering the introduction of devices employing UWB. It considers the issues to take into account in order to protect all radiocommunication services from interference. Recommends deployment of short range UWB communications under a general licence regime and provides information on emission masks adopted by relevant administrations.
- **SM.1757: Impact of devices using ultra-wideband technology on systems operating within radiocommunications services.** Includes a compilation of studies and results that may be considered in order to assess the impact of UWB devices on existing radiocommunications. It describes deterministic and statistical methodologies used in interference analysis.

The ITU-R recommendation SM.1756, considers that a generalized regulatory regime is best suited for short range UWB communications. It does not recommend a particular spectral mask, as it recognizes the rights of administrations for regulating UWB communication devices within their territorial boundaries. The ITU-R recommends as well the adoption of rigorous product certification provisions.

2.5. Standards

UWB has to share the spectrum with several other radio communication systems in the market. The UWB transmitted power is much lower than the other systems which makes it appear as noise to the narrowband applications which transmission power is high. The spectrum sharing between UWB and other important narrowband systems is shown in Fig. 2.9. The 802.11a standard, which is responsible of Wireless Local Area Networks (WLAN) such as Wi-Fi, has the largest allocated bandwidth.

Two international organizations have published a standard or part of a standard devoted to UWB technology. The first organization is the well known American based IEEE. The second is the European based Ecma International. An extract of standards is given in the following sections.

2.5.1. IEEE802.15.4a

This IEEE802.15.4a standard [28] gives the specifications for Wireless Medium Access Control (MAC) and Physical Layer (PHY) of Low-Rate Wireless Personal Area Networks (LR-WPAN), which uses IR-UWB technology. It defines three independent bands which are:

- The sub-gigahertz band, which consists of a single channel and occupies the spectrum

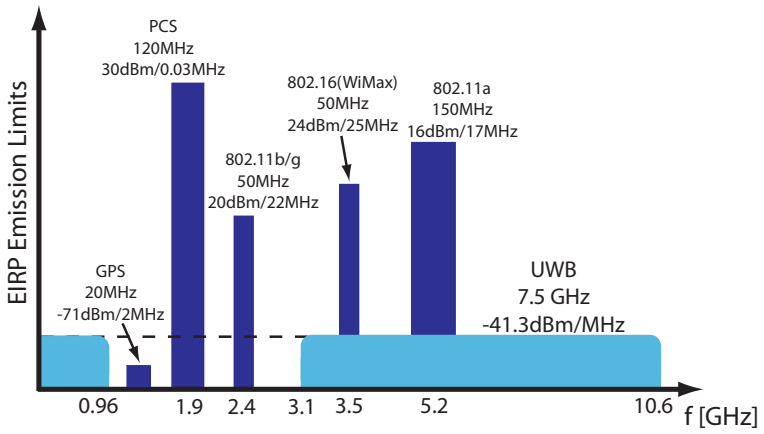

Figure 2.9.: Frequency allocation of UWB and other existing wireless systems.

from 249.6 MHz to 749.6 MHz

- The low band, which consists of four channels and occupies the spectrum from 3.1 GHz to 4.8 GHz
- The high band, which consists of eleven channels and occupies the spectrum from 6.0 GHz to 10.6 GHz

Table 2.1 contains the characteristics of each of the channels composing the UWB band according to the IEEE802.15.4a standard.

Table 2.1.: UWB band allocation

Channel Number	Center frequency [MHz]	Bandwidth [MHz]	Mandatory/Optional
0	499.2	499.2	Mandatory below 1 GHz
1	3494.4	499.2	Optional
2	3993.6	499.2	Optional
3	4492.8	499.2	Mandatory in low band
4	3993.6	1331.2	Optional
5	6489.6	499.2	Optional
6	6988.8	499.2	Optional
7	6489.6	1081.6	Optional
8	7488.0	499.2	Optional
9	7987.2	499.2	Mandatory in high band
10	8486.4	499.2	Optional
11	7987.2	1331.2	Optional
12	8985.6	499.2	Optional
13	9484.8	499.2	Optional
14	9984.0	499.2	Optional
15	9484.8	1354.97	Optional

A compliant UWB device should be capable of transmitting in at least one of three specified bands. A UWB device that implements the sub-gigahertz band shall implement channel 0. A UWB device that implements the low band shall support channel 3. The remaining low-band channels are optional. A UWB device that implements the high band shall support channel 9. The remaining high-band channels are optional.

It leaves the power spectral density (PSD) in accordance with regulations for UWB in different parts of the world, which are mentioned in the previous sections. The extremely wide bandwidth characteristics (UWB) can provide very robust performance under harsh multipath and interference conditions

The peak pulse repetition (PRF) states the highest frequency in megahertz at which a compliant transmitter shall emit pulses. It is set to 499.2 MHz for all the channels. The mean PRF is defined as the total number of pulses emitted during a symbol period divided by the length of the symbol duration. There are three possible mean PRFs (15.6 MHz, 3.90 MHz, and 62.4 MHz).

UWB channels 4, 7, 11, 15 are all optional channels and are differentiated from other UWB channels by the larger bandwidth ($>$ 500 MHz) of the transmitted signals. These channels overlap the existing lower bandwidth channels. The larger bandwidth enables devices operating in these channels to transmit at a higher power (for fixed PSD constraints), and thus they may achieve longer communication range. The larger bandwidth pulses offer enhanced multipath resistance.

2.5.2. Ecma International: Standard ISO/IEC

The International Electrotechnical Commission (IEC) approved in 2007 two ISO/IEC international standard specifications for high data rate UWB. These were based on specifications released by the European Computer Manufacturers Association [29] (Ecma International) in 2005 (ECMA 368 and ECMA 369). These standards relate to UWB technology employing MB-OFDM. The ISO/IEC standards, their name and a short description are:

- **ISO/IEC 26907:2007. Information technology - Telecommunications and information exchange between systems - High rate UWB PHY and MAC standard.** Specifies a distributed MAC sublayer and a physical layer for wireless networks. The PHY and MAC specified in this standard are compatible to high data rate communications between a diverse set of mobile and fixed electronic devices. (Based on the ECMA 368 Standard)
- **ISO/IEC 26908:2007. Information technology - MAC–PHY interface for ISO/IEC 26907.** Specifies the MAC–PHY interface for a high rate, ultra-wideband wireless transceiver. (Based on ECMA-369 Standard)

The standards specify the UWB physical layer and medium access control sublayer for a high-speed, short-range wireless network, using all or part of the spectrum between 3 100−10 600 MHz supporting data rates of up to 480 Mb/s. It divides the spectrum into 14 bands, each with a bandwidth of 528 MHz. The first 12 bands are then grouped into four band groups consisting of three bands. The last two bands are grouped into a fifth band group. A

sixth band group is also defined within the spectrum of the first four, consistent with usage within worldwide regulatory regulations (Fig. 2.2). A MB-OFDM scheme is used to transmit information, using 110 sub-carriers.

The standard also specifies a transmitted spectral mask (for every band), that shall have the following break points: an emissions level of 0 dBr (dB relative to the maximum spectral density of the signal) from -260 MHz to 260 MHz around the center frequency, -12 dBr at 285 MHz frequency offset, and -20 dBr at 330 MHz frequency offset and above. For all other intermediate frequencies, the emissions level is assumed to be linear in the dB scale. The spectral density of the transmitted signal shall fall within the spectral mask, as shown in Fig. 2.10. Dependent on local regulations, additional limitations on the permitted transmissions and on the absolute transmit power levels may apply.

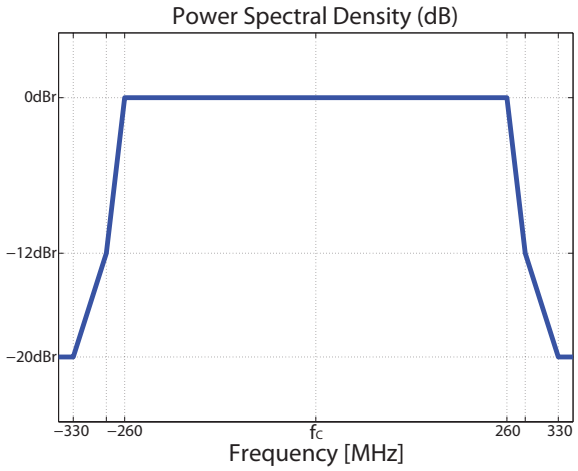

Figure 2.10.: Transmit power spectral density mask.

The standard defines a symbol length T_{SYM} of 312.5 ns which traduces to a symbol rate F_{SYM} of 3.2 MHz.

2.6. Power Measurements

Low transmission power together with ultra large bandwidth are the main characteristics of UWB technology. The power restrictions are given by the administration of each region, as defined in the previous sections. These restrictions are important in order to avoid interference between the different systems sharing the 3.1−10.6 GHz spectrum.

The ITU in its recommendation SM.1754: Measurements techniques of ultra-wideband transmissions, defines the procedure to measure PSD from an UWB transmitter, as well as the effective isotropic radiated power (EIRP). It defines two PSD values which are used for different purposes, they are the peak and average power.

The ITU-R recommends a distance of 3 m to do the emission measurement. This distance can be decreased if the signal is too weak, taking care of not decreasing it below the far field

condition. The measurement distance should satisfy then the following equation

$$R > \frac{2D^2}{\lambda} \tag{2.4}$$

where R is the distance in meters, D the diameter of the sphere enclosing the device under test, and λ the wavelength.

Frequency domain measurements are usually done using a spectrum analyzer. A diagram containing its main components is shown in Fig. 2.11. The spectrum analyzer represents the fundamental and each harmonic contained in the input signal. This is done by sweeping a filter over all the frequencies containing the pulse. The IF filter is in charge of doing this sweep. Its resolution bandwidth (RBW) should be wisely defined, in order to measure the correct power spectrum of the signal.

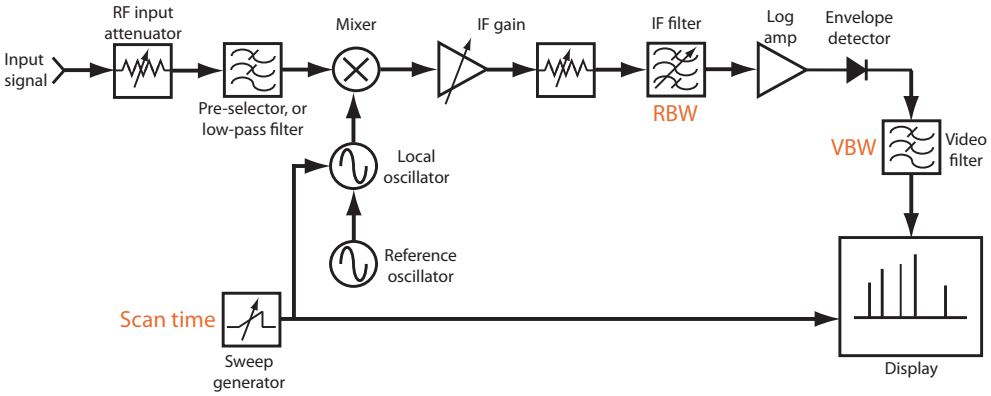

Figure 2.11.: Schematics of a Vector Network Analyzer.

The definition of peak and average power can be obtained from Fig. 2.12. The average power is equal to the peak power multiplied by the duty cycle:

$$P_{avg} = P_{peak}\frac{\tau_{eff}}{T} = P_{peak}\tau_{eff}PRF \tag{2.5}$$

Written as a ratio in dB:

$$\frac{P_{avg}}{P_{peak}} = 10log_{10}(\tau_{eff}PRF) \tag{2.6}$$

Considering the RF pulse in Fig. 2.12, its pulse repetition frequency (PRF) is equal to 1/T. The bandwidth of the IF filter can be manually set in the spectrum analyzer. When RBW is smaller than PRF (Fig. 2.13(a)), the display is a frequency domain display of the actual Fourier components of the input signal. When the RBW is larger than the PRF (Fig. 2.13(b)), the Fourier-transform response of the pulsed signal is displayed. The first setup is called "Line" spectrum and the second is named "Pulse" spectrum in [30].

The standards in Section 2.5 define different values of PRF, the smallest value defined by

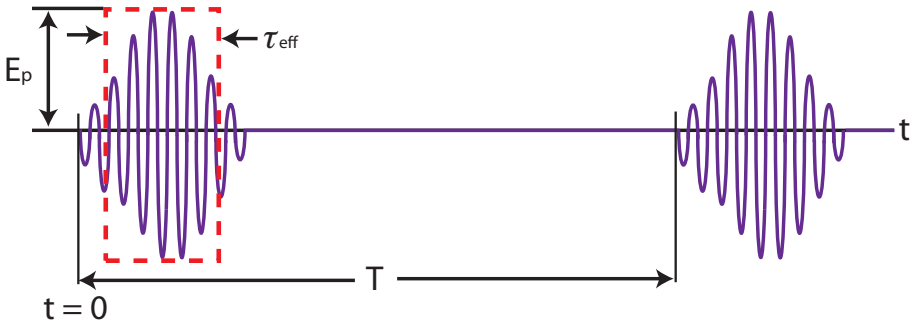

Figure 2.12.: Basic RF pulse (Figure adapted from [30]).

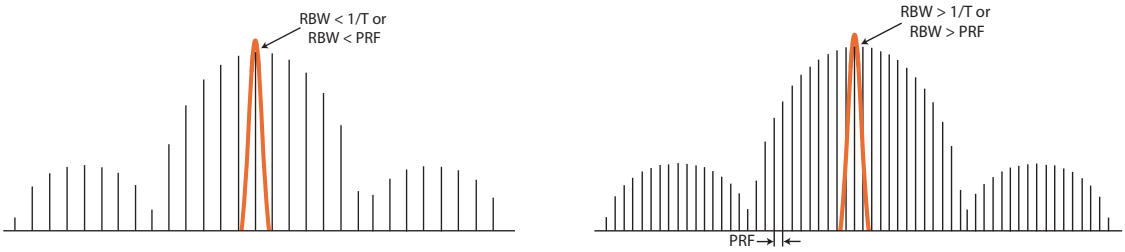

Figure 2.13.: IF bandwidth (RBW) and pulse repetition frequency (PRF): (a) Line Spectrum, (b) Pulse Spectrum.

the IEEE as 3.9 MHz. Standard spectrum analyzers have a highest RBW of 3 MHz. Therefore when measuring an UWB signal, the PRF will be always smaller than the RBW. For this reason, the measurements should be done using a "Line" Spectrum setup.

In this setup, the display has the normal true frequency domain characteristics. The amplitude of each line will not change when the RBW is changed as long as it remains considerably below the PRF (RBW $<$ 0.3 PRF). When the width of the pulse τ_{eff} is very small, the power of the modulated signal is distributed over a number of spectral components (carrier and sidebands) and its power seems to be reduced. Each spectral line containing only a fraction of the total power. The reduction in power is given by the line spectrum pulse desensitization factor α_L, which is equal to the duty cycle τ_{eff}/T in decibels:

$$\alpha_L = 20 \log_{10}\left(\frac{\tau_{eff}}{T}\right) \tag{2.7}$$

This equation is only valid for a true Fourier line spectrum (RBW $<$ 0.3 PRF). If a 500 MHz pulse is used (τ_{eff} = 2 ns) and a 3.9 MHz PRF, the pulse desensitization will be of -42.16 dB, which is considerably large. This shows that the real signal to be measured is a pulsed signal which has to be measured using a "Pulse" spectrum setup. To achieve this, the PRF of the UWB signal should be decreased to a level of about RBW/1.7.

With a PRF lowered so that RBW $>$ 1.7 PRF, the pulse spectrum is used to measure peak and average powers. In the "Pulse" spectrum setup, the displayed spectrum is a combination of time and frequency information. The lines that form the envelope are pulse lines in time domain, each line is displayed when a pulse occurs (separation between lines is equal to PRF). The spectrum envelope is displayed in the frequency domain. The amplitude of the envelope increases linearly as RBW increases, as long as RBW $< 0.2/\tau_{eff}$. When the IF filter bandwidth is equal to $1/\tau_{eff}$ (or half of the main-lobe width), the display amplitude is practically the peak amplitude of the signal.

The different setups of the spectrum analyzer required to do the correct peak and average power measurements (using the "Pulse" spectrum setup) will be given in the following subsections. The exact definitions of the EIRP, peak power and average power, given by the FCC and IEEE are given, as well as the proposed limitations.

2.6.1. EIRP

The definition of EIRP in the "IEEE Standard Definitions of Terms for Antennas" [31] is:

> "In a given direction, the gain of a transmitting antenna multiplied by the net power accepted by the antenna from the connected transmitter."

The FCC describes the EIRP for UWB systems in the Title 47 Part 15, subpart F (15.503) [25] as:

> "Equivalent isotropically radiated power, i.e., the product of the power supplied to the antenna and the antenna gain in a given direction relative to an isotropic antenna. The EIRP, in terms of dBm, can be converted to a field strength, in dBμV/m at 3 meters, by adding 95.2. As used in this subpart, EIRP refers to the highest signal strength measured in any direction and at any frequency from the UWB device, as tested in accordance with the procedures specified in 15.31(a) and 15.523 of this chapter."

The EIRP value is obtained by

$$EIRP = P_{in} + G_A \qquad [\text{dBm}] \tag{2.8}$$

where $EIRP$ is given in dBm , P_{in} is the power in dBm measured at the antenna terminal, and G_A is the antenna gain in dBi at a given direction. The field strength at 3 meters is then calculated as

$$E\big|_{3\text{m}} = P_{in} + G_A + 95.2 \qquad [\text{dB}\mu\text{V/m}] \tag{2.9}$$

2.6.2. Peak Power

The FCC states the limit for peak power level of the emissions contained within a 50 MHz bandwidth centered on the frequency at which the highest radiated emission occurs, f_M. That limit is 0 dBm EIRP. The value 50 MHz was chosen as it is the widest bandwidth of a victim receiver that is likely to be encountered.

Peak measurements based on a 50 MHz (resolution) bandwidth may not be feasible, as the widest available RBW that can be employed (in standard spectrum analyzers) for peak measurements is 3 MHz. It is acceptable to employ a different resolution bandwidth, and a correspondingly different peak emission limit. The resolution bandwidth shall not be lower than 1 MHz or greater than 50 MHz, and the measurement shall be centered on the frequency at which the highest radiated emission occurs, f_M. If a resolution bandwidth other than 50 MHz is employed, the peak PSD limit shall be calculated using the the following equation.

$$PSD_{Limit-RBW} = PSD_{Limit-BW} + 20\log_{10}\left(\frac{RBW}{BW}\right) \tag{2.10}$$

where $BW = 50$ MHz and RBW is the resolution bandwidth in megahertz that is employed.

The peak emission level stated by the FCC is 0 dBm/50 MHz, which is equivalent to a peak field strength of 58mV/m at 3 meters. Using (2.11), the peak emission level measured with a 3 MHz RBw is -24.44 dBm/3 MHz and a peak field strength of 3.46 mV/m at 3 meters.

Spectrum analyzer setup

Ideally the RBW should be 50 MHz, but as mentioned before, this is not the case for most of spectrum analyzers available to the public. The largest bandwidth available is 3 MHz and the lower usable bandwidth is 1 MHz. The PRF should be set in order to achieve this condition.

The IF filter resolution bandwidth (RBW) should be chosen according to the following restriction [30]

$$1.7PRF < RBW < \frac{0.1}{\tau_{eff}} \tag{2.11}$$

The scan time should be larger than 10/PRF

$$T_s[\text{s/Div}] > \frac{10}{PRF} \tag{2.12}$$

The effective pulse duration τ_{eff} is calculated from the lobe width as:

$$\tau_{eff} = \frac{2}{\text{main lobe width}} \tag{2.13}$$

The pulse desensitization is calculated using the following formula

$$\alpha_p = 20log_{10}(\tau_{eff} \times K \times RBW) \qquad [\text{dB}] \tag{2.14}$$

where K is a correction factor ($K = B_{rect}/RBW$), as a perfect rectangular filter is assumed when the real filter shape is not really rectangular. This correction factor has been measured for Agilnet PSA series as approximately $K = 1.5$.

The peak power will then be the amplitude level displayed by the analyzer plus α_p. It should be smaller than the peak PSD limit found using equation (2.11).

$$PSD_{peak} \leq PSD_{Limit-RBW} \tag{2.15}$$

2.6.3. Average Power

The FCC states that the average limit of a radiated UWB field is 500 μV/m, as measured at 3 meters with a 1 MHz resolution bandwidth (RBW). Using (2.9) it can be proved that this value corresponds to the average power limit of the FCC spectrum mask: -41.3 dBm/MHz.

The average power is calculated from (2.6), adding the peak power and the duty cycle in dB.

$$P_{avg}[\text{dB}] = P_{peak}[\text{dB}] + 10log_{10}(\tau_{eff} \times PRF) \tag{2.16}$$

2.7. Conclusion

In this chapter, an introduction on Ultra-wideband technology was given. The two main systems that cover the UWB band are named MB-OFDM and IR-UWB. While MB-OFDM uses carriers to divide the UWB spectrum in 14 sub-bands, IR-UWB sends very narrow pulses to cover the desired band. The different modulation scenarios for IR-UWB were briefly mentioned, together with the gaussian and carrier-band pulses used to transmit information. These pulses are of special interest in this thesis, as they will be used in the following sections to characterize UWB antennas.

Regulations of Ultra-wideband technology in the U.S., Europe and Japan were discussed. The differences among them are shown when plotting the UWB spectral masks for each region.

A summary of the standards available today was presented. The parameters that are most related to the antenna transmission were mentioned. These parameters are contained in the PHY specifications.

This thesis will focus on IR-UWB. OFDM is maybe more advanced in its commercialization, having already devices in the market. The reason to choose IR-UWB is that an antenna that is capable of transmitting an UWB pulse, will also be able to work for OFDM. But this is not true for the reverse case, as an antenna could have a good performance at some OFDM bands, but not be able to transmit a UWB pulse without deformation. The implication of the time domain analysis and the importance of phase deformation are further motivations to study this approach. Antennas have been mostly studied in the frequency domain, but analyzing their time dependance is essential to evaluate the performance of UWB antennas.

The time and frequency domain methods to characterize UWB antennas are described in detail in the following chapter. A method that incorporates time, frequency and space analysis of antennas is proposed in the subsequent chapter.

References

[1] WiMedia Alliance. [Online]. Available: http://www.wimedia.org/en/index.asp

[2] M. Z. Win and R. A. Scholtz, "Impulse radio: how it works," *IEEE Commun. Lett.*, vol. 2, no. 2, pp. 36–38, Feb. 1998.

[3] F. J. Agee, C. E. Baum, W. D. Prather, J. M. Lehr, J. P. O'Loughlin, J. W. Burger, J. S. H. Schoenberg, D. W. Scholfield, R. J. Torres, J. P. Hull, and J. A. Gaudet, "Ultra-wideband transmitter research," *IEEE Trans. Plasma Sci.*, vol. 26, no. 3, pp. 860–873, Jun. 1998.

[4] W. D. Prather, C. E. Baum, J. M. Lehr, J. P. O'Loughlin, S. Tyo, J. S. H. Schoenberg, R. J. Torres, T. C. Tran, D. W. Scholfield, J. Gaudet, and J. W. Burger, "Ultra-wideband source and antenna research," *IEEE Trans. Plasma Sci.*, vol. 28, no. 5, pp. 1624–1630, Oct. 2000.

[5] D. M. Pozar, "Optimal radiated waveforms from an arbitrary UWB antenna," *IEEE Trans. Antennas Propag.*, vol. 55, no. 12, pp. 3384–3390, Dec. 2007.

[6] Q. Wang and J. Yao, "An electrically switchable optical ultrawideband pulse generator," *J. Lightw. Technol.*, vol. 25, no. 11, pp. 3626–3633, Nov. 2007.

[7] X. Chen and S. Kiaei, "Monocycle shapes for ultra wideband system," in *Proc. IEEE International Symposium on Circuits and Systems ISCAS 2002*, vol. 1, May 26–29, 2002, pp. I–597–I–600.

[8] J. Ryckaert, M. Badaroglu, C. Desset, V. De Heyn, G. ven der Plas, P. Wambacq, B. van Poucke, and S. Donnay, "Carrier-based UWB impulse radio: simplicity, flexibility, and pulser implementation in 0.18-micron CMOS," in *Proc. IEEE International Conference on Ultra-Wideband ICU 2005*, Sep. 5–8, 2005, pp. 432–437.

[9] R. Xu, Y. Jin, and C. Nguyen, "Power-efficient switching-based cmos uwb transmitters for uwb communications and radar systems," *Microwave Theory and Techniques, IEEE Transactions on*, vol. 54, no. 8, pp. 3271 –3277, Aug. 2006.

[10] S. Wood and R. Aiello, *Essentials of UWB*, ser. Cambridge Wireless Essential Series. Cambridge University Press, 2008.

[11] intel. [Online]. Available: http://www.intel.com/technology/usb/

[12] S.-W. Su, J.-H. Chou, and K.-L. Wong, "Internal ultrawideband monopole antenna for wireless usb dongle applications," *Antennas and Propagation, IEEE Transactions on*, vol. 55, no. 4, pp. 1180 –1183, April 2007.

[13] D. Krishna, M. Gopikrishna, C. Aanandan, P. Mohanan, and K. Vasudevan, "Ultra-wideband slot antenna for wireless usb dongle applications," *Electronics Letters*, vol. 44, no. 18, pp. 1057 –1058, 28 2008.

[14] T. G. Savelyev, L. van Kempen, H. Sahli, J. Sachs, and M. Sato, "Investigation of time ndash;frequency features for gpr landmine discrimination," *Geoscience and Remote Sensing, IEEE Transactions on*, vol. 45, no. 1, pp. 118 –129, Jan. 2007.

[15] L. Carin, R. Kapoor, and C. Baum, "Polarimetric SAR imaging of buried landmines," *Geoscience and Remote Sensing, IEEE Transactions on*, vol. 36, no. 6, pp. 1985 –1988, Nov 1998.

[16] X. Li, E. Bond, B. Van Veen, and S. Hagness, "An overview of ultra-wideband microwave imaging via space-time beamforming for early-stage breast-cancer detection," *Antennas and Propagation Magazine, IEEE*, vol. 47, no. 1, pp. 19 – 34, Feb 2005.

[17] S. Salvador and G. Vecchi, "Experimental tests of microwave breast cancer detection on phantoms," *Antennas and Propagation, IEEE Transactions on*, vol. 57, no. 6, pp. 1705 –1712, June 2009.

[18] E. Staderini, "UWB radars in medicine," *Aerospace and Electronic Systems Magazine, IEEE*, vol. 17, no. 1, pp. 13 –18, Jan 2002.

[19] L. Jofre, A. Broquetas, J. Romeu, S. Blanch, A. Toda, X. Fabregas, and A. Cardama, "UWB tomographic radar imaging of penetrable and impenetrable objects," *Proceedings of the IEEE*, vol. 97, no. 2, pp. 451 –464, Feb. 2009.

[20] M. Klemm, I. Craddock, J. Leendertz, A. Preece, and R. Benjamin, "Radar-based breast cancer detection using a hemispherical antenna array - experimental results," *Antennas and Propagation, IEEE Transactions on*, vol. 57, no. 6, pp. 1692 –1704, june 2009.

[21] J.-Y. Lee and R. Scholtz, "Ranging in a dense multipath environment using an UWB radio link," *Selected Areas in Communications, IEEE Journal on*, vol. 20, no. 9, pp. 1677 – 1683, Dec 2002.

[22] E. Saberinia and A. Tewfik, "Ranging in multiband ultrawideband communication systems," *Vehicular Technology, IEEE Transactions on*, vol. 57, no. 4, pp. 2523 –2530, July 2008.

[23] Y. Takeuchi, Y. Shimizu, and Y. Sanada, "Examination of antenna combinations for uwb ranging system," *Microwave Theory and Techniques, IEEE Transactions on*, vol. 54, no. 4, pp. 1858 – 1864, June 2006.

[24] H. Nikookar and R. Prasad, *Introduction to Ultra Wideband for Wireless Communications*, ser. Signals and Communication Technology. Springer Netherlands, 2009. [Online]. Available: http://www.springerlink.com/content/q81q615q34703633/

[25] FCC. Title 47, Section 15 of the Code of Federal Regulations, SubPart F: Ultra-wideband. [Online]. Available: http://www.access.gpo.gov/nara/cfr/waisidx_05/47cfr15_05.html

[26] *Technical Conditions on UWB Radio Systems in Japan*, AWF3/14 Std.

[27] ITU Radiocommunication Sector (ITU-R). [Online]. Available: http://www.itu.int/ITU-R/index.asp?category=information&rlink=rhome&lang=en

[28] *IEEE Standard for Information Technology - Telecommunications and Information Exchange Between Systems - Local and Metropolitan Area Networks - Specific Requirement Part 15.4: Wireless Medium Access Control (MAC) and Physical Layer (PHY) Specifications for Low-Rate Wireless Personal Area Networks (WPANs)*, Std., 2007.

[29] *Standards ECMA 368-369*, ECMA international Std., December 2008. [Online]. Available: http://www.ecma-international.org/publications/standards/Ecma-368.htm

[30] *Application Note 150-2. Spectrum AnalysisĚPulsed RF*, Agilent Spectrum Analyzer Series, Agilnet Technologies.

[31] *IEEE standard definitions of terms for antennas.*, IEEE Std., 21 June 1993.

3. Ultra-wideband Antenna Characterization

3.1. Introduction

Once the general concept of Ultra-wideband technology is understood we should proceed to the main focus of this thesis: Ultra-wideband antennas. This chapter starts with a short introduction about the history of antennas. The evolution of antennas from Hertz to our modern days is summarized. An important link exists between the first antennas and UWB antennas, as the first antennas transmitted sparks or short pulses which can be compared to UWB pulses.

Since the beginning of the radio times it has been important to characterize antennas in order to be able to transmit as much energy and in the most efficient way as possible. These methods were mostly in the frequency domain, as they were meant for narrowband antennas. UWB antenna characterization should be also done in the time domain, as they send pulsed signals and not continuous-wave signals. The two types of characterization, narrowband and UWB, will be described in detail. The most important parameters in the frequency and time domain will be discussed and explained, using as example an omnidirectional and a directional antenna.

From the study of the available characterization methods, several limitations were found and are listed in Section 3.5. Due to these restrictions, a complete and fair comparison of UWB antennas cannot be achieved when analyzing conventional antenna parameters. Therefore being a strong motivation to implement a new characterization method that could be used to characterize and compare UWB antennas in an efficient way. This and other important findings of the chapter are summarized in the last section.

3.2. A brief historical survey on antennas

Heinrich R. Hertz demonstrated in 1886 the generation of electromagnetic waves. He used a gap dipole, which is now considered to be the first antenna, to generate an electrical spark. He was able to detect it using another antenna located at a distance of about 20 m. Hertz constructed dipoles, loop and parabolic antennas as well [1]. In 1901 Marconi did the first trans-Atlantic transmission. The transmitted signals were short or long pulses representing the Morse code. A large wire antenna connected to ground was used for the purpose. Although the main goal of these wireless pioneers was to transmit narrowband signals, they began radiating Ultra-wideband damped impulse signals [2].

Following this success, multiple radio stations started to transmit for the general public.

This proved the great use and success of wireless technology, and since then scientists have not stopped improving the performance of the radios. The bandwidth of the systems was quite narrow, even though radio antennas were able to receive all the AM and FM radio signals. Filtering of the channels was done at the radio system, after being received by the antenna. Channels were transmitted with a bandwidth in the order of kHz. Television entered the market in late 1930's, frequency allocation was in the MHz band and with a channel bandwidth of about 6 MHz. The same antenna approach as the radio was used: wideband antennas able to receive all the channels.

In the 1980's the boom of the mobile telephone mobilized radio engineers and technology started to advance at higher pace. The electromagnetic signals were now at higher frequencies (450 MHz, 900 MHz, 1.8 GHz). The frequency reuse concept started to be used, optimizing the spectrum usage and only a limited number of channels are needed. The information still being sent by continuous waves signals.

Controlled and desired transmission of narrow pulses was first used by military radars in World War II. Radar is an acronym for RAdio Detection And Ranging used by the U.S. Navy. The antennas used are mostly directive, including horns, antenna arrays and lenses. The allocated used bandwidth, designated by the IEEE is given in Table 3.1.

Radar is closely related to UWB and it might be considered as its direct predecessor. Even if the radiated power is much higher compared to UWB, the idea of transmitting very short pulses comes from this technology. Some of the characterization methods used today in UWB antennas were first used to characterize radar antennas. Conventional parameters used to characterize narrowband antennas are discussed in the next section, followed by the methods used in UWB antennas, some of which are as well used for radar applications.

Table 3.1.: Radar IEEE Band Designations

Band Name	**Frequency Range**
HF	3 – 30 MHz
VHF	30 – 300 MHz
UHF	300 – 1000 MHz
L-band	1 – 2 GHz
S-band	2 – 4 GHz
C-band	4 – 8 GHz
X-band	8 – 12 GHz
K_u-band	12 – 18 GHz
K-band	18 – 27 GHz
K_a-band	27 – 40 GHz
Millimeter wave band	40 – 300 GHz

3.3. Characterization of Narrowband antennas

Maybe the largest difference between narrowband and Ultra-wideband antennas is that narrowband antennas have been studied mostly in the frequency domain. Frequency do-

main techniques are well known by antenna designers. Continuous waves were employed since the beginning in the transmission of RF signals. These signals were easily decomposed into their frequency components. Antennas were designed to transmit these frequencies in a proper way.

The following parameters are the most well known and widely used to characterize antennas. Therefore, as accounting for the reader to know them well, only a small summary is presented.

3.3.1. Antenna matching

Antenna matching is one of the most important parameters when designing an antenna, as it defines the amount of energy the latter can radiate. An ideal antenna will radiate all the power injected into its input terminals. Therefore, to avoid reflections at the antenna port, the antenna should be matched to the input transmission line (Fig. 3.1). The voltage reflection coefficient (or S_{11}) at the input port of an antenna is defined as

$$\Gamma = \frac{Z_A - Z_C}{Z_A + Z_C} \tag{3.1}$$

where Z_A and Z_C are the impedances of the antenna and the transmission line, respectively. It can be expressed in power as:

$$\Gamma_{dB} = 20log(\rho) \tag{3.2}$$

where $\rho = |\Gamma|$. A more commonly used expression is the return loss, which is defined as the inverse of the power reflection coefficient [3]:

$$RL = -20log(\rho) \tag{3.3}$$

Another parameter representing the antenna mismatch is the voltage standing wave ratio (VSWR)

$$VSWR = \frac{1+\rho}{1-\rho} \tag{3.4}$$

Typical return loss values are 6 or 10 dB as a limit in the lower and higher edges of the band. Narrowband antennas can be identified from its return loss, as their best match is at the resonant frequency. A broadband antenna, on the other hand, might have multiple resonances.

Measurements of the reflection coefficient can be done directly using a network analyzer (VNA). Simulations of this parameter are very accurate. Depending on the antenna structure and size the differences between simulations and measurements might be large. Special attention has to be done when measuring small monopoles. This will be discussed in detail in Chapter 5.

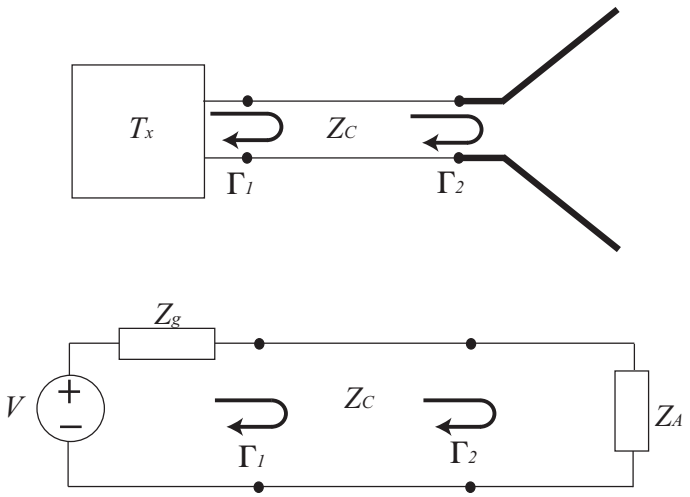

Figure 3.1.: Antenna reflection coefficient in transmission and circuit representation. (Figure adapted from [3])

3.3.2. Radiation pattern

The radiation pattern of an antenna is a graphical representation of its radiation properties as a function of space coordinates [1]. Antenna radiation is commonly characterized by its directivity or gain in the frequency domain. The directivity is defined as:

$$D = \frac{U}{U_0} = \frac{4\pi U}{P_{rad}} \tag{3.5}$$

Where U is the radiation intensity at a given direction from the antenna, U_0 is the radiation intensity averaged over all directions in a sphere and P_{rad} is the total power radiated by the antenna [4].

The antenna gain is another useful parameter that takes in consideration the antenna radiation efficiency e. As defined in [4] gain does not include losses arising from impedance and polarization mismatches. It is then related to the directivity as:

$$G = eD \tag{3.6}$$

The radiation patterns are normalized to a an isotropic antenna, therefore the values of directivity and gain are given in dBi. Idealized radiation patterns of a directional antenna and an omnidirectional antenna are shown in Fig. 3.2(a) and Fig. 3.2(b), respectively. Each of the lines represent a different frequency at which the pattern was calculated.

Radiation pattern measurements are done inside an anechoic chamber and at given number of frequencies. Special attention should be made as well when measuring small antennas.

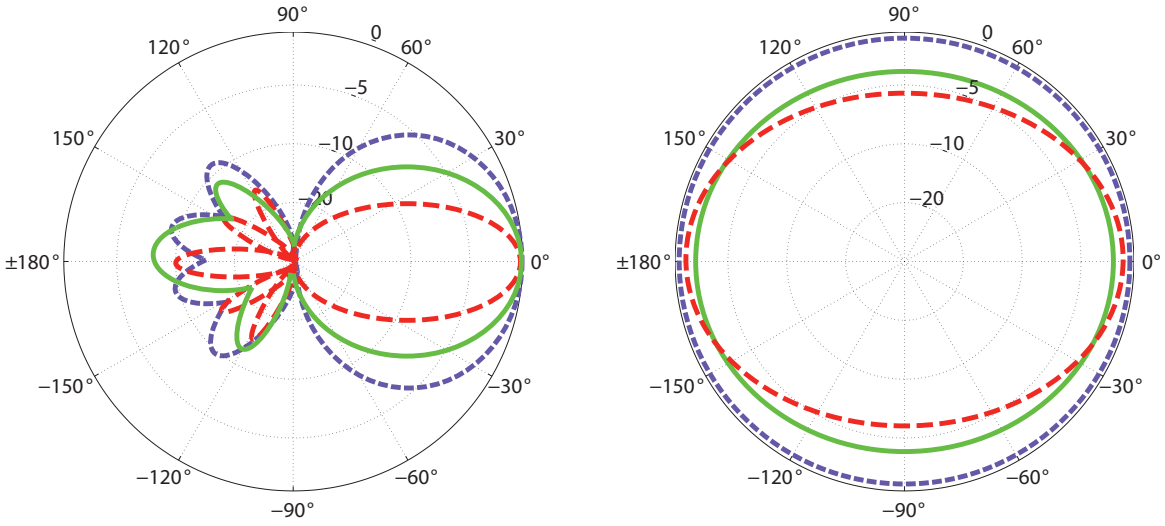

Figure 3.2.: Radiation Pattern of an: (a) Directive antenna, (b) Omnidirectional antenna.

We can say from our experience that simulation tools available today are less accurate in modeling the radiation pattern than the reflection coefficient. The number of assumptions made by the solver (boundary conditions, currents in edges, etc.) is large and might be the reason for this miss-evaluation of the radiated field. The simulated values might differ from the measured ones, but they are accurate enough to compare the radiated signals, as will be shown in Chapter 4.

3.3.3. Radiation Efficiency

Radiation efficiency is the ratio of the total power radiated by an antenna to the net power accepted by the antenna from the connected transmitter [4].

$$e = \frac{P_{rad}}{P_{in}} = \frac{P_{rad}}{P_{rad} - P_{loss}} \tag{3.7}$$

where P_{loss} is the power loss in the antenna structure, P_{rad} the radiated power and P_{in} the input power at the antenna terminals.

Measurements using the Wheeler cap method are widely used to calculate the efficiency of narrowband patch antennas [5],[6]. The cap is a metallic or conducting hemisphere surrounding the antenna. The antenna is located inside the cap with a ground plane common to both structures. The impedance of the antenna with and without the cap is measured and

the efficiency is obtained as [7]:

$$e = \frac{R_{no-cap} + R_{cap}}{R_{no-cap}} \tag{3.8}$$

The method is only valid for resonant antennas that have a characteristic impedance of the type RLC. The size of the Wheeler cap depends on the resonant frequency, its radio being $r \approx \lambda/2\pi$ [8]. The effect of the cap size and shape has been investigated in [7], where cubic caps are used instead of semi-spheres. Efficiency calculation methods of UWB antennas had been studied, and will be discussed in the following section, where characterization methods for UWB antennas are discussed.

Today's simulation tools can directly calculate radiation efficiency. It is recommended to check the definition used by each software, as sometimes it might be different from the one given in this section.

3.4. Characterization of Ultra-wideband antennas

There exist different parameters that are used to characterize UWB antennas. Some of them were already mentioned in the previous section and are used for narrowband antenna characterization. Others have been utilized and formulated only to characterize wideband antennas which may or not transmit short pulses (IR-UWB or MB-OFDM). This last group was first used in radar applications, where the radiating pulse has a duration of nanoseconds and spectral bandwidth larger than 100% [9]. When UWB was born in 2002, these characterization methods were applied to the novel antenna designs and new methods started to be investigated.

A summary of the most commonly used characterization techniques of UWB antennas is presented in the following sections. The techniques are either in the frequency or time domain and can be obtained from simulations or measurements. Some examples are included in order to better understand their meaning.

3.4.1. Gain Pattern

The most common way of representing the directivity or gain is to plot them in a polar plot. This is done for a given frequency and it represents the antenna radiation in one plane, therefore it is normally called "Radiation Pattern" (Section 3.3.2). The antenna type could be easily identified by seeing its pattern, as directive antennas have a main lobe radiating more at a given angle than at other angles (Fig. 3.2(a)), and the omnidirectional antennas radiate with the same intensity in all directions in the plane (Fig. 3.2(a)). The radiation pattern can be only plotted at a given frequency at a time, therefore it is ideal for narrow-band antennas which radiation do not change much over frequency.

The radiation pattern is often used as well to characterize UWB antennas. Plotting it for every frequency is almost impossible, so it is only shown at some frequencies. Most designers

prefer to represent every frequency in a different plot in order to make it more clear and neat. This takes more space and it is many times not evident to find the differences between the plots. Ideally the pattern should be identical at every frequency inside the band, but this is rarely the case for UWB antennas.

A more visual manner of representing the changes of Gain over frequency and angle is what we call the "Gain Pattern". It consists of a 2D plot of frequency versus angle, having as a third parameter the antenna gain. The plot will then contain the Gain information both in frequency and angle of radiation, and it will be easy to identify where and at which frequencies the antenna radiates best (or worst). Again, for an ideal omnidirectional antenna, the whole plot should be in the same color, showing that the gain is frequency independent in a given plane. The gain pattern of an ideal directional antenna will have a higher gain value concentrated at the main beam width and the gain will be zero at angles outside the main lobe.

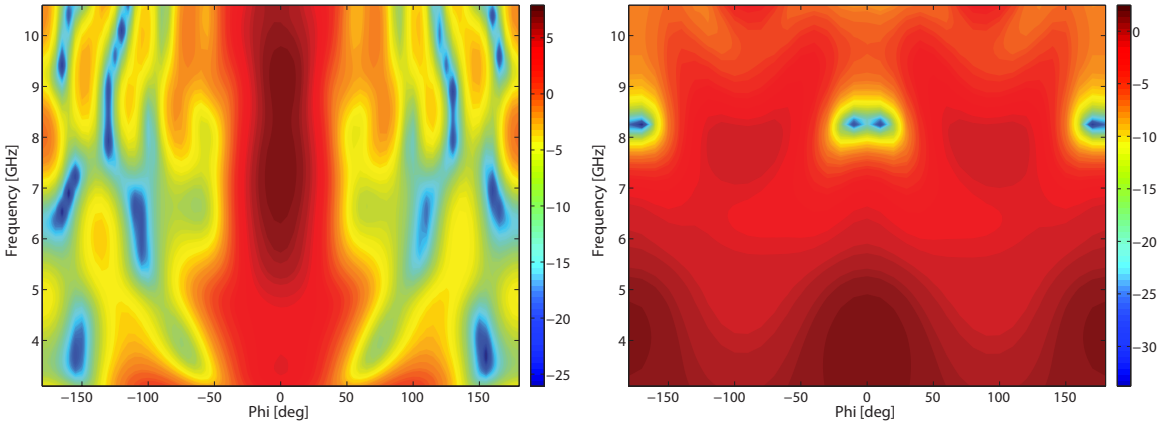

(a) (b)

Figure 3.3.: Total Gain Pattern of: (a) Vivaldi antenna, (b) Circular Monopole.

In Fig. 3.3 the simulated gain pattern of a circular monopole (omnidirectional) and a Vivaldi antenna (directive) are shown. The gain was calculated every 5°in the azimuthal plane ϕ over the UWB band. The bad radiation points can be identified easily for each frequency. The Vivaldi antenna has a constant gain over the whole band at the main beam direction while it is very low outside the main beam at every frequency. On the other hand, the circular monopole pattern (Fig. 3.3(b)) has an almost constant color at all frequencies and angles. Nevertheless, some very low gain points are seen around 8.2 GHz. The planar monopole antenna will be thoroughly studied in the next chapters, where these low gain points are analyzed in more detail and its effect on UWB pulse distortion described.

3.4.2. UWB Radiation Efficiency

New methods to calculate the efficiency over a wider bandwidth, based on the Wheeler cap method have been investigated in [10] and [11]. They used a cap size larger than the one

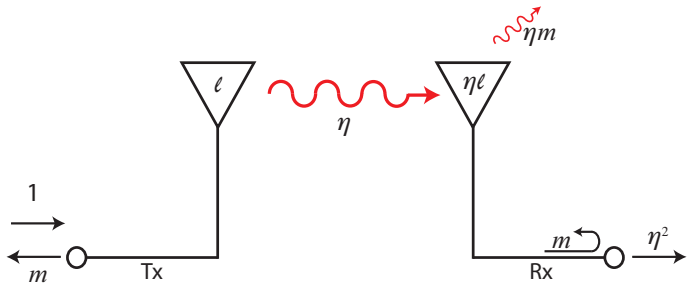

Figure 3.4.: Power budget for a Tx-Rx antenna pair. (Figure adapted from [11])

needed for narrowband antennas. The "UWB Wheeler Cap", proposed by Schantz [11] allows the antenna to radiate freely and then receive its own reflected signal.

The power budget of a transmitting antenna can be separated in power fractions: a fraction of the input power is dissipated in losses ($\ell = P_{loss}/P_{in}$), another fraction is reflected due to mismatch ($m = P_{reflected}/P_{in}$) and another fraction is radiated ($\eta = P_{rad}/P_{in}$). Then the sum of these powers over a suitable time interval and applying conservation of energy is: $\ell + m + \eta = 1$. This power budget is shown in Fig. 3.4, where a two identical antenna system is illustrated. All the radiated power is available at the receiving antenna (Rx). The factor ηm represents the part of the transmitted power reflected at the Rx antenna terminals.

Inside the Wheeler cap, the antenna receives the reflected signals from the cap (Fig. 3.5), these reflections are almost ideal time reversal of the transmitted signal. Therefore the reflected power inside the UWB wheeler cap is equal to the reflection coefficient in free-space $m = |S_{11FS}|^2$, and the scattering parameters inside the UWB Wheeler cap becomes:

$$\begin{aligned} |S_{11WC}|^2 &= m + \eta^2 + \eta^2 m^1 + \eta^2 m^2 + \eta^2 m^3 \cdots \\ &= |S_{11FS}|^2 + \eta^2 \sum_{n=0}^{\infty} |S_{11FS}|^{2n} = |S_{11FS}|^2 + \eta^2 \frac{1}{1 - |S_{11FS}|^2} \end{aligned} \tag{3.9}$$

where S_{11FS} refers to the reflection coefficient in free-space and S_{11WC} inside the UWB Wheeler cap.

Calculating from it the radiation coefficient η yields:

$$\eta = \sqrt{(1 - |S_{11FS}|^2)(|S_{11WC}|^2 - |S_{11FS}|^2)} \tag{3.10}$$

The approach assumes that the reflections inside the Wheeler cap are orthogonal to each others.

Simulation tools available today calculate the radiation efficiency at a given frequency only. However, the Wheeler cap can be implemented inside the simulation environment and the efficiency calculated from the antenna return loss inside it and in free-space [12].

Other methods are based on time domain measurements inside a reverberation chamber

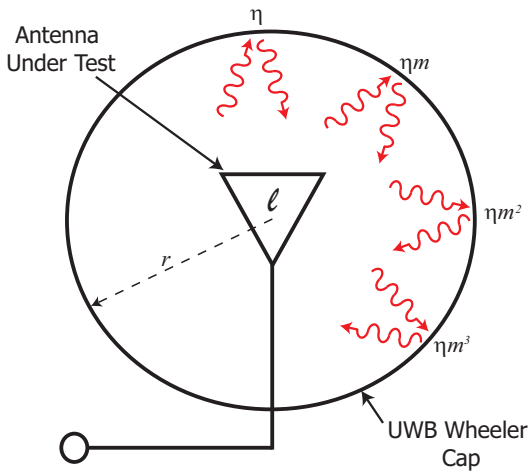

Figure 3.5.: Reflections inside UWB Wheeler Cap. (Figure adapted from [11])

[13],[14]. Therefore also taking in consideration multiple reflections inside the chamber.

3.4.3. Fidelity Factor

Ultra-wideband systems radiate very short pulses in time. Transmission of these pulses on a multi obstacle environment will lead to a high dispersion. Antenna designers cannot control the dispersion produced by the environment, but can take into consideration the distortion produce by the antenna itself, which in many cases is considerable. Therefore the antenna distortion should be quantified in time.

The term Fidelity was first used in 1970 by Susman and Lamensdorf, its first public paper being [9]. In 1994 when the interest on short-pulse-measurement systems and impulse radar technologies increased, they made an abbreviate version [15]. It is this latest document that Ultra-wideband antenna designers have been using as reference, and from where the concept of Fidelity Factor started.

Fidelity (or alternately, distortion) is, as stated in [15], a useful measure of distortion between two signals, preserving amplitude weighting and time shifting of the signal. The input signal at the antenna terminals $r(t)$ and radiated field $f(t)$, are normalized as shown in (4.45) and (4.46). The normalization is done in order to compare only the shape of the pulses, and not their magnitude, as the $f(t)$ is expected to be much lower than $r(t)$.

$$\hat{r}(t) = \frac{r(t)}{\left[\int_{-\infty}^{\infty} |r(t)|^2 dt\right]^{1/2}} \tag{3.11}$$

$$\hat{f}(t) = \frac{f(t)}{\left[\int_{-\infty}^{\infty} |f(t)|^2 dt\right]^{1/2}} \tag{3.12}$$

The cross-correlation between both signals is done at every point in time and the maximum value of this correlation is obtained when both pulses overlap. The fidelity factor (FF) is therefore calculated as:

$$FF = \max_{\tau} \int_{-\infty}^{\infty} \hat{f}(t)\hat{r}(t+\tau)dt \tag{3.13}$$

CST Microwave Studio [16] made it very simple and straightforward to obtain this value using its Transient solver. The user can add Probes at a given radial position around the antenna, choosing the desired distance from the origin. The radiated field component in time domain will be obtained by the probe. The user can define the orientation of the probes in order to obtain the desired field polarization.

Fig. 3.6 shows the setup of the probes to measure the E-field component radiated by the circular monopole. They are located every 20°in the ϕ and θ planes and in a radius of 30 mm from the center of the monopole. The radial distance as well as the separation between probes can be changed according the resolution and distance required. The orientation of the probes (θ) is according to the monopole structure, which has a vertical polarization.

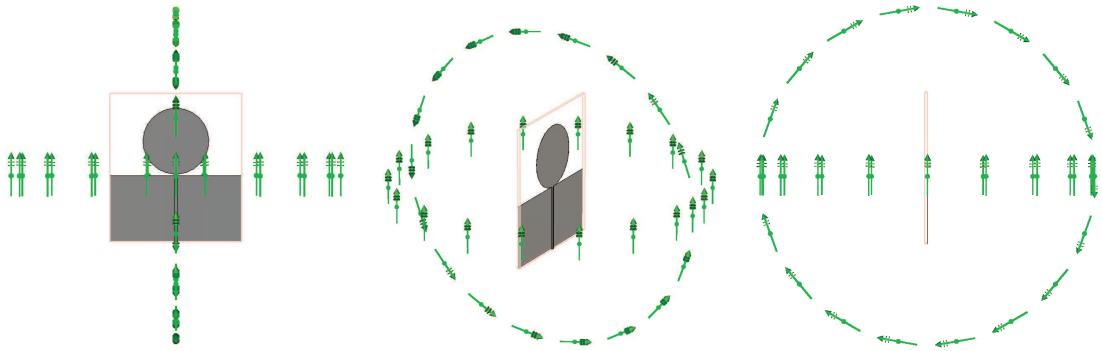

(a) (b) (c)

Figure 3.6.: CST probes.

The Fidelity Factor of the circular monopole is calculated for every radiated E-field obtained by probes located 500 mm apart from the center of the structure and separated ever 10°. The monopole is almost omnidirectional in the azimuthal plane (see gain pattern in Fig. 3.3(b)), nevertheless its fidelity (Fig. 3.7(c)) is lower at $\phi = 0°, 180°$ than at the other directions by almost 20%. The low fidelity coincides with the low gain points in its gain pattern and the same occurs for the high fidelity values and constant gain at $\phi = \pm 90°$. Therefore the fidelity of an antenna is proportional to the flatness of the gain over the desired band. This is again the case for the Vivaldi antenna, whose gain is constant over the UWB band at bore-sight, and so its fidelity is almost unity in this direction (Fig. 3.7).

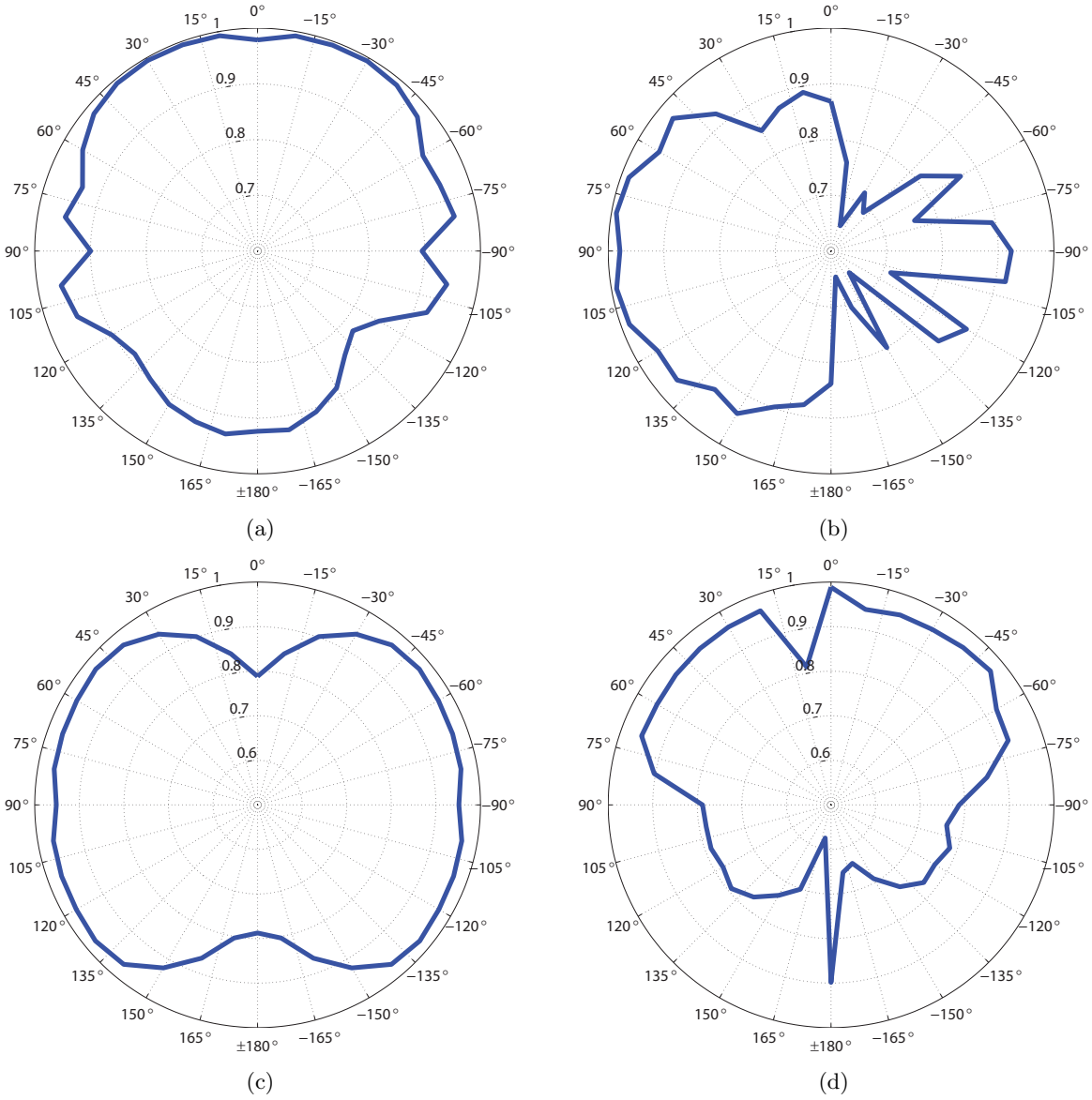

Figure 3.7.: Fidelity Factor of: (a) Vivaldi antenna in the azimuthal plane ($\theta = 90°, \phi$), (b) Vivaldi antenna in the elevation plane($\theta, \phi = 0°$) (c) Circular monopole in the azimuthal plane ($\theta = 90°, \phi$), (d) Circular monopole in the elevation plane($\theta, \phi = 0°$).

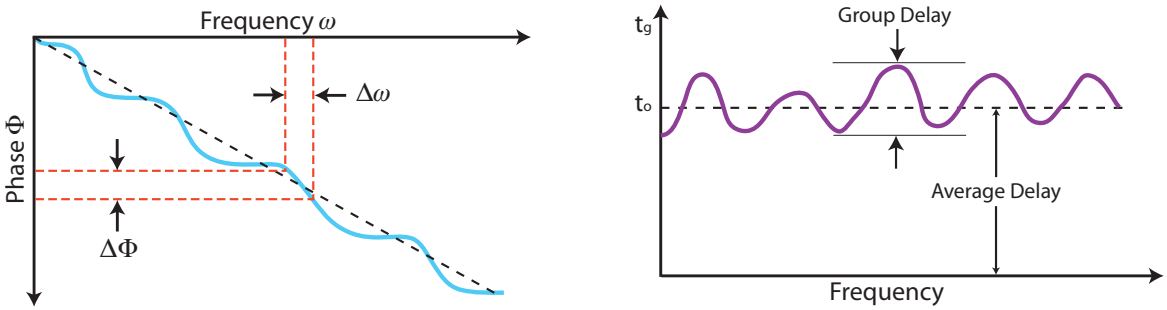

Figure 3.8.: What is group delay? (Figure adapted from [18]) (a) Phase response, (b) Group Delay.

3.4.4. Group Delay

Group delay is commonly used to characterize two port devices (filters, amplifiers, mixers, etc). It measures the absolute signal delay and the phase distortion between the input and the output of the device.

The frequency dependent complex transfer function $H(\omega)$ (equivalent to the impulse response $h(t)$) on a given device can be expressed as follows

$$H(\omega) = A(\omega)e^{j\Phi(\omega)} \tag{3.14}$$

where $A(\omega)$ is the amplitude and $\Phi(\omega)$ the phase response of the device.

The group delay is defined as the derivative of the phase response versus frequency [17].

$$\tau = -\frac{d\Phi(\omega)}{d\omega} = -\frac{1}{360^\circ}\frac{d\Phi(f)}{df} \tag{3.15}$$

A graphical representation of (3.15) is shown in Fig. 3.8. The linear portion of the phase response is reduced to a constant value, and the deviations from linear phase are transformed into deviations from constant group delay. The average delay represents the average signal transit time through a device or a two ports system [18].

Phase non-linearities (or deviations from linear phase) produce signal distortion in communications systems. A phase ripple in a device can be measured specifying its maximum peak-to-peak. Nevertheless, this may not be sufficient to completely characterize it, as the slope of the phase ripple depends on the number of ripples that occur per unit of frequency. Group delay takes this into account, and it is often a better indicator of phase distortion. In Fig. 3.9 an example is shown where two phases have the same maximum peak-to-peak but different group delay. The phase in Fig. 3.9(a) has few ripples per unit of frequency, hence a small peak-to-peak group delay. Fig. 3.9(b) on the other hand has more ripples per unit of frequency and a large peak-to-peak group delay. The group delay in Fig. 3.9(a) is more constant than the one in Fig. 3.9(b), having the same phase peak-to-peak.

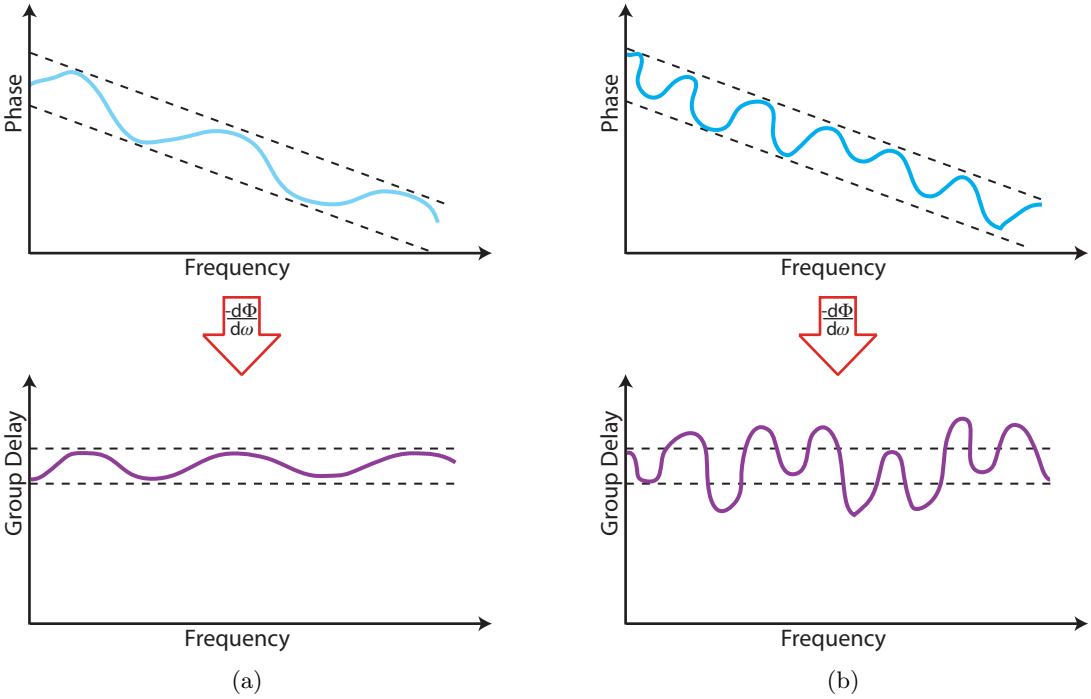

Figure 3.9.: Same peak-to-peak phase ripple can result in different group delay.(Figure adapted from [18])

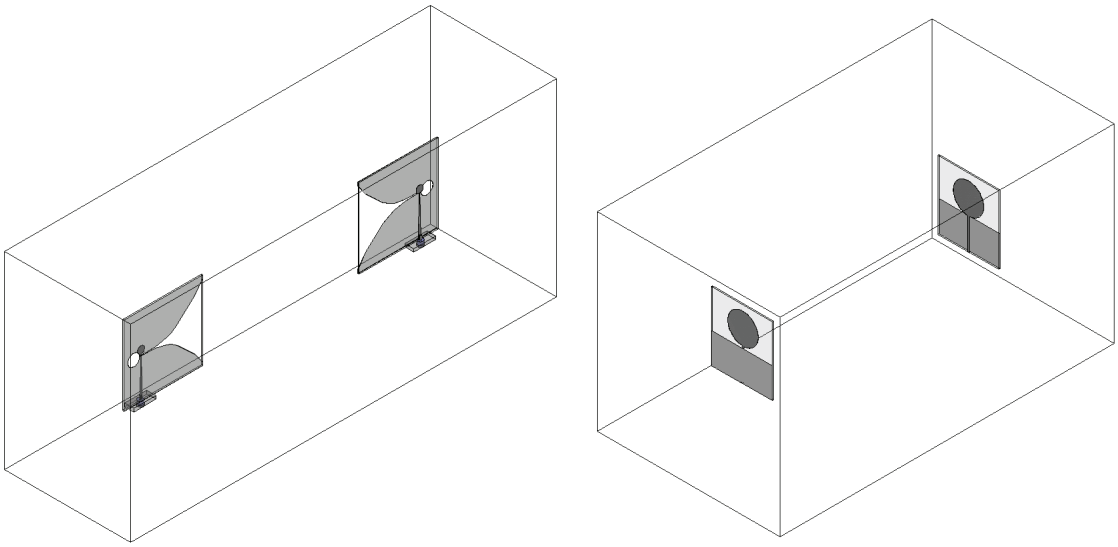

(a) (b)

Figure 3.10.: Group delay simulation setup in HFSS.

Vector network analyzers (VNA) can calculate the group delay directly from phase measurements [19],[18]. They measure a different quotient rather than the differential on (3.15), which yields to a good approximation if the phase Φ is not too non-linear in the observation frequency range Δf.

$$\tau_g = -\frac{\Delta\Phi(\omega)}{\Delta\omega} = -\frac{1}{360^\circ}\frac{\Phi(f+\Delta f/2)-\Phi(f-\Delta f/2)}{\Delta f} \tag{3.16}$$

The transfer function $H(\omega)$ between two antennas can be measured and from it the group delay of the system can be obtained. The group delay measures the total phase distortion of the antenna system, and the dispersion of the transmitted signal can be inferred. The average of the group delay being the time taken to the signal to travel from one antenna terminal to the other. The phase response of two antennas can be obtained using available simulations tools [16],[20] even though it is time consuming and a large computer capacity is needed. Measurements can be done straight forward using a conventional VNA, therefore it is a simple way to characterize an antenna in the time domain. A big constraint of this characterization method is that there is no standardization of the delay allowed in an UWB system, therefore it is up to the designer to decide whether the delay is good or bad for the transmitted signal.

Two antenna systems composed of two circular monopoles and two Vivaldi antennas were simulated using CST and HFSS [20]. The antennas are located like shown in Fig. 3.10, 150 mm apart from each other. The system phase response was converted into group delay using the Matlab code from [21]. The distance between antennas was the largest value accepted by HFSS to run the simulation with the available computer resources. CST could manage a

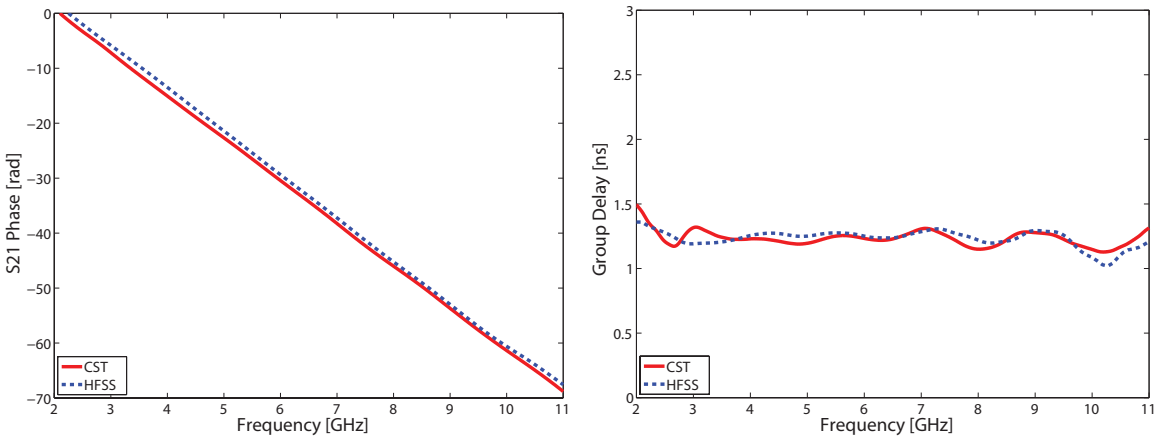

(a) (b)

Figure 3.11.: Simulation of an antenna system composed of two Vivaldi antennas: (a) S21 Phase, (b) Group delay.

maximum distance of 750 mm, but 150 mm was used in order to make a fair comparison between simulations. The computational time is considerable large (> 30 min) for each system, and the group delay is only obtained at one orientation. This is the optimal orientation of the vivaldi system, but it might be interesting to calculate the group delay of the monopole system at other directions.

The phase of the Vivaldi system is linear over all the frequency band and the results obtained from CST and HFSS are similar, as shown in Fig. 3.11(a). Even if the phases are almost identical and linear, the group delay is not completely linear (Fig. 3.11(b)), but is clearly more linear than that of the monopole system (Fig. 3.12(b)). The larger delay in the Vivaldi system, compared to the monopole system, is due to the distance between the antennas, as it is 150 mm between the edges closer to each antenna and not from its feeding lines.

Fig. 3.12(a) shows the phase response of the simulated S21 parameters. A difference between CST and HFSS is clear between 8 and 10 GHz. This difference is better appreciated in Fig. 3.12(b), where the system group delay is plotted. The HFSS value is almost constant at all frequencies, while the line of CST has a large delay at 8.5 GHz. Below 7 GHz both lines are almost identical, it is only on frequencies above 7.5 GHz where the group delay obtained by CST is no longer constant and abrupt changes appear. HFSS is a frequency dependent software while CST is time dependent, this could one reason for the large difference between the simulated values.

3.4.5. Impulse Response

The meaning of impulse response will be explained in depth in Chapter 4. We consider important to mention it here, as this is a well know characterization method used particularly

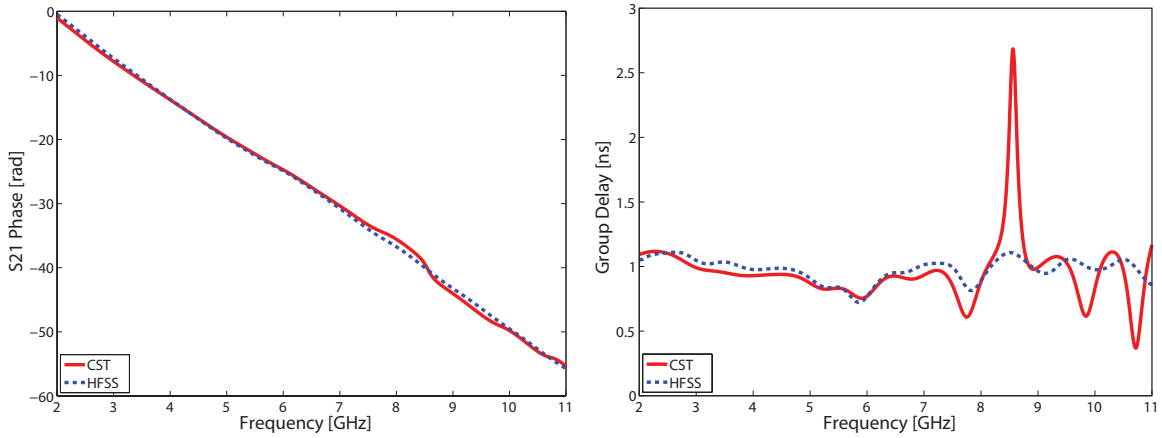

(a) (b)

Figure 3.12.: Simulation of antenna systems composed of two circular monopoles: (a) S21 Phase, (b) Group delay.

for UWB antennas parametrization.

Several important parameters concerning the impulse response of an antenna system are described by Wiesbeck et al. in [22]. The impulse response $h(t, \theta, \phi)$ or the transfer function in the frequency domain $H(\omega, \theta, \phi)$ contains all the information about the performance of an antenna system. The envelope of the analytic impulse response is obtained using the Hilbert transform as

$$h^+(t) = h(t) + j\mathcal{H}\{h(t)\} \tag{3.17}$$

where $h(t)$ is the system impulse response and $\mathcal{H}$ represents the Hilbert transform. The envelope $|h^+(t)|$ represents the distribution of the energy versus time. A direct measure of the dispersion could be derived from this value.

The peak value of the envelope is defined as

$$p(\theta, \phi) = \max_t |h^+(t, \theta, \phi)| \qquad [\mathrm{m/ns}] \tag{3.18}$$

It represents the highest value of the time domain response of the antenna system. A high value is desirable, as it is related to the amount of power the antenna is able to radiate.

The envelope width, measured at the full width at half maximum (FWHM*) of the analytic envelope $|h^+(t)|$, describes the broadening of the radiated impulse or the time required by the system to transmit half of the power. It is defined as:

$$\tau_{FWHM} = t_1|_{|h^+(t_1)|=p/2} - t_2|_{t_1<t_2, |h^+(t_2)|=p/2} \qquad [\mathrm{ns}] \tag{3.19}$$

*The FWHM is used to calculate the difference between the two extreme values of an independent variable at which the dependent variable is equal to half of its maximum value.

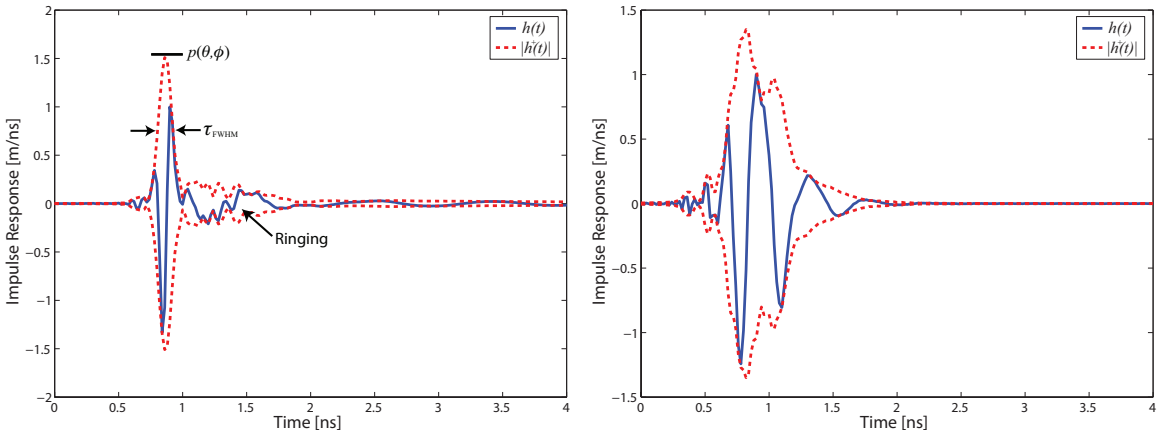

Figure 3.13.: Simulated Impulse response of: (a) Vivaldi antenna, (b) Circular monopole.

A narrow envelope is desired to enhance high data rates in communications and high resolution in radar applications [22].

The ringing is defined as the time needed for the envelope to decrease from its peak value $p(\theta, \phi)$ to a certain level $\alpha p(\theta, \phi)$. It is mathematically defined as:

$$\tau_{r=\alpha} = t_1|_{|h^+(t_1)|=\alpha p} - t_2|_{t_2<t_1, |h^+(t_2)|=p} \qquad [\text{ns}] \tag{3.20}$$

The ringing might be a factor of undesired resonances due to energy storage or multiple reflections inside the antenna. It is important to analyze it as it might cause inter symbol interference (ISI) when radiating a group of pulses.

Two examples, using the same antennas as in the previous subsections (Vivaldi and planar circular monopole) are given. The simulated impulse response of the antennas systems composed of two identical antennas (Vivaldi or monopole) was obtained. A distance of 0.25 m between them is used. The antennas are located like in Fig. 3.10, the Vivaldis have the maximum directive points facing each others.

The normalized impulse responses and their envelopes are shown in Fig. 3.13. As the signals are normalized, we cannot distinguish the real peak value of the signals, but the peak value of the Vivladi antenna is much higher than that of the monopole.

3.5. Available characterization methods: Limitations

The methods described in the previous section can be divided in single antenna and two-antennas system characterization. The single antenna methods are those who characterize the

radiation characteristics of the antenna under test by itself. In this group we can include the following parameters: radiation efficiency, gain pattern and fidelity factor. Antenna system methods use commonly two identical antennas to characterize the transmission properties of the system. Inside this group are the group delay and the impulse response.

The five methods mentioned above are not good enough to fully characterize UWB antennas. Lets remember that to fully characterize an omnidirectional antenna, its frequency and time domain characteristics have to be analyzed over a complete radiation plane. Table 3.2 enumerates the main limitations of these methods.

A new characterization method is needed that combines the most important information given by the methods above. This is achieved, as shown in the following chapter, with the System Fidelity Factor. It is the two-antennas system version of the Fidelity Factor. The receiving pulse at the Rx antenna is used instead of the radiated E-field. The input and receiving pulses are correlated, therefore quantifying the total dispersion produced by the antenna system.

3.6. Conclusion

A brief historical overview of antennas since the beginning of radio transmission until our days was given at the beginning of the chapter. The importance of radar technology was emphasized, and related to UWB antennas. Even though, short pulses were already used by the radio pioneers (Hertz and Marconi), it was not until World War II and the invention of the radar, that desirable pulse transmission and time domain analysis of antennas started.

Narrowband characterization methods can be used as well for UWB antennas. The reflection coefficient is maybe the first parameter to consider when designing an antenna, as it defines its bandwidth of operation and is easy to calculate from both simulations and measurements. The radiation pattern is another important parameter to analyze in the desired frequency band. The radiation efficiency might be more difficult to calculate but can be essential to analyze the total antenna behavior. Nevertheless, these two last parameters are more useful to characterize narrowband antennas. Other methods are used to characterize UWB antennas, which are based in the radiation pattern and efficiency.

The gain pattern plots the gain at every frequency and angle of radiation (ϕ or θ). It is the UWB version of the radiation pattern, and is very useful for analyzing the antenna gain over the whole bandwidth. The radiation efficiency of UWB antennas has to be evaluated in a different way than for narrowband antennas, some methods include a UWB Wheeler cap or a reverberation chamber. The fidelity factor correlates the input pulse at the transmitting antenna terminals with the radiated field in the time domain. It allows to effectively quantify the distortion produced by a transmitting antenna over a given plane. The impulse response of an antenna system in time domain is a good descriptor of systems transmitting pulses. The envelope of the impulse response can be calculated and from it the dispersion produced by the system calculated. Its peak value, envelope width and ringing were discussed.

Table 3.2.: Limitations of UWB characterization methods

Method	Limitations
Radiation Efficiency	There is not at this moment, a simulation tool that gives the radiation efficiency over a complete frequency range, as this method was first defined for narrowband antennas. Measurements require a complex structure such as the Wheeler Cap. The metallic case needs to be of a specific size according to antenna under test, therefore a new fabricated cap has to be done for each antenna which might be expensive and time consuming.
Gain Pattern	This method plots antenna gain versus frequency. By definition it does not include any information about the phase, which is a crucial determinant of pulse distortion. Even if the frequency range and the direction where the gain is lowest can be easily identified, a conclusion about pulse distortion cannot be driven. Distortion depends on where in the frequency band the lowest gain is, and the value of this gain. For example: a gain decrease of 10 dB will produce distortion, but if this occurs in the middle of the band, the distortion will be larger than if this occurs near the upper edge of the band.
Fidelity Factor	This method is a good indicator of pulse distortion over a given plane. However, its main limitation is that it is not evident to measure the radiated E-field in the time domain. Time domain equipments of our days have low dynamics which make it difficult to measure a signal with the bandwidth used by the FCC, but it might be possible to measure a signal in the ECC band. Nevertheless, antenna designers use normally frequency domain equipment and are usually more familiarized with this type of instruments. On the other hand, direct simulations cannot be made with all available simulation tools.
Group Delay	There exists no definition on the maximum variation allowed to achieve good transmission performance. Pulse dispersion depends on the location inside the frequency band where the maximum delay occurs, as well as its magnitude. Standard values of maximum variation and frequency position can be approved according to each specific application. Nevertheless, this can be done only at one direction at a time, and several plots might be needed to represent the group delay at every angle in the desired plane.
Impulse Response	The main constraint about this method is, like for the group delay, the fact that for each angular direction in the desired plane, a new plot is needed. The peak value $p(\theta, \phi)$ is a good indicator of the power transmitted by the system. It could be calculated for every direction and plotted in polar format. This gives a more visual result where the peak value at each direction can be seen directly. This could as well be implemented for τ_{FWHM}. Nevertheless, the results in most of the papers are only shown for a given direction.

A new characterization method will be proposed in the next chapter. It combines some of the methods described before and allows a fair comparison of UWB antennas over a given radiation plane.

References

[1] C. A. Balanis, *Antenna Theory. Analysis and Design.*, Third ed. Wiley-Interscience, 2005.

[2] H. Schantz, *The Art and Science of Ultrawideband Antennas.* Artech House, 2005.

[3] P.-S. Kildal, *Foundations of Antennas. A Unified Approach.* Studentlitteratur, 2000.

[4] *IEEE standard definitions of terms for antennas.*, IEEE Std., 21 June 1993.

[5] G. Smith, "An analysis of the wheeler method for measuring the radiating efficiency of antennas," *Antennas and Propagation, IEEE Transactions on*, vol. 25, no. 4, pp. 552 – 556, jul 1977.

[6] D. Pozar and B. Kaufman, "Comparison of three methods for the measurement of printed antenna efficiency," *Antennas and Propagation, IEEE Transactions on*, vol. 36, no. 1, pp. 136 –139, jan 1988.

[7] H. Choo, R. Rogers, and H. Ling, "On the wheeler cap measurement of the efficiency of microstrip antennas," *Antennas and Propagation, IEEE Transactions on*, vol. 53, no. 7, pp. 2328 – 2332, july 2005.

[8] H. Wheeler, "The radiansphere around a small antenna," *Proceedings of the IRE*, vol. 47, no. 8, pp. 1325 –1331, aug. 1959.

[9] D. Lamensdorf and L. Susman, "An analysis of some directive antennas using time domain measurements," in *Proc. Antennas and Propagation Society International Symposium*, vol. 9, Sep. 1971, pp. 307–310.

[10] P. Miskovsky, J. Gonzalez-Arbesu, and J. Romeu, "Antenna radiation efficiency measurement in an ultrawide frequency range," *Antennas and Wireless Propagation Letters, IEEE*, vol. 8, pp. 72 –75, 2009.

[11] H. Schantz, "Radiation efficiency of UWB antennas," 2002, pp. 351 – 355.

[12] R. Johnston, "Efficiency simulations on a vivaldi antenna in a wheeler cap," in *Antennas and Propagation Society International Symposium, 2009. APSURSI '09. IEEE*, 1-5 2009, pp. 1 –4.

[13] A. Khaleghi, "Time-domain measurement of antenna efficiency in reverberation chamber," *Antennas and Propagation, IEEE Transactions on*, vol. 57, no. 3, pp. 817 –821, march 2009.

[14] G. Le Fur, P. Besnier, and A. Sharaiha, "Efficiency measurement of UWB antennas using time reversal in reverberation chambers," *Electronics Letters*, vol. 44, no. 17, pp. 1002 –1003, 14 2008.

[15] D. Lamensdorf and L. Susman, "Baseband-pulse-antenna techniques," *IEEE Antennas Propag. Mag.*, vol. 36, no. 1, pp. 20–30, Feb. 1994.

[16] CST Microwave Studio 2009. [Online]. Available: http://www.cst.com/Content/Products/MWS/Overview.aspx

[17] X. Zhu, Y. Li, S. Yong, and Z. Zhuang, "A novel definition and measurement method of group delay and its application," *IEEE Trans. Instrum. Meas.*, vol. 58, no. 1, pp. 229–233, Jan. 2009.

[18] *Understanding the Fundamental Principles of Vector Network Analysis*, Application note 1287-1 ed., Agilnet Technologies, 2005.

[19] O. Ostwald, *Group and Phase Delay Measurements with Vector Network Analyzer ZVR*, application note 1ez35_1e ed., Rohde & Schwarz, Munich, Germany, July 1997.

[20] Ansoft High Frequency Structure Simulator (HFSS) v12.0 (2009). [Online]. Available: http://www.ansoft.com/products/hf/hfss/

[21] A. Pintado Rodríguez, "Ultrawideband antenna characterization," Master's thesis, Ecole Polytechnique Fédérale de Lausanne, 2008.

[22] W. Wiesbeck, G. Adamiuk, and C. Sturm, "Basic properties and design principles of UWB antennas," *Proceedings of the IEEE*, vol. 97, no. 2, pp. 372 –385, feb. 2009.

4. System Fidelity Factor

4.1. Introduction

This chapter presents a new method for characterizing UWB antennas: the System Fidelity Factor. UWB antennas should be studied in frequency domain as well as in time domain, as UWB systems radiate very short pulses. The parameters described in Chapter 3 characterize an antenna either in the frequency or time domain at a given point in the space, but they do not present all these important characteristics together. The only parameter that analyzes time, space and frequency together is the Fidelity Factor [1]. There are several limitations in the calculation of this parameter, since the radiated E-field in time is needed. Not all simulation tools can directly obtain the time domain E-field, and special measurement equipment is required, which in most cases has limited dynamics.

The System Fidelity Factor (SFF) calculates the distortion produced by an antenna when transmitting a pulse to another antenna. The transmission coefficient S_{21} which is equal to the system transfer function is calculated. It is then multiplied by the input pulse (in frequency domain) at the transmitting antenna terminal and later translated into the time domain, obtaining with this the received pulse. This is done for a complete plane (ϕ or θ) and does not take more time, effort or computer power than analyzing a single antenna. A method similar to the SFF was presented in [2]. They used a time domain software and measurements to obtain the radiated signal, but it was only done at some points in the azimuth plane and the results were presented in a table form, making the comparison difficult.

In the first part of the chapter, the procedure to derive the SFF will be described in the following way. First a definition of the transfer function in frequency and time domain is given, followed by the simulation and measurement methods to calculate it. The post-processing needed to obtain the received pulse and the SFF will be described afterwards.

The second part of the chapter consists of the application of the proposed method on UWB antennas analysis. Two examples are given where the UWB performance of three antenna systems are compared using the SFF. In the first example, three antenna systems composed of two identical monopoles are studied. In the second example, the transmitting antenna is a Vivaldi and the receiving antenna a monopole. Conclusion will be shown in the last section. The first monopole as well as the Vivaldi antenna were introduced in the previous chapter to illustrate the most common characterization methods of UWB antennas.

4.2. Transfer Function

The transfer function of a two antenna system is analogue to the impulse response used in communication theory to describe Linear Time-Invariant (LTI) Systems [3]. It relates the input and the output signals of the system. A representation of a continuous time system is given in Fig. 4.1, where *x(t)*, *y(t)* and *h(t)* are respectively the input, output and impulse response of the system.

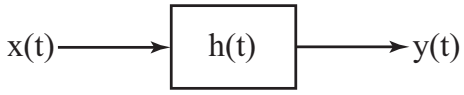

Figure 4.1.: Impulse response of a continuous time system.

The output of the system in Fig. 4.1 is obtained from the convolution between the input and the system impulse response. This is represented in the frequency domain as a multiplication, as shown in (4.1). The term transfer function $H(s)$ is defined by Oppenheim [3] in the Laplace domain ($s = j\omega$), and refers to $H(\omega)$ as the frequency response of the system, which is the Fourier transform of the system impulse response. It should be emphasized that in the domain of this thesis we will refer to $H(\omega)$ as the transfer function.

$$y(t) = h(t) * x(t) \overset{\mathfrak{F}}{\longleftrightarrow} Y(\omega) = H(\omega)X(\omega) \tag{4.1}$$

The same definition is applied in antenna technology, where an input signal at the transmitting antenna (Tx) passes through the system and is recovered by a receiving antenna (Rx). The system transfer function in Fig. 4.2 includes the antenna systems and the channel, which means that the effect of both antennas and the channel will have an impact on the signal transmission. $H(\omega)$ is identical to the transmission coefficient between the two antennas S_{21}.

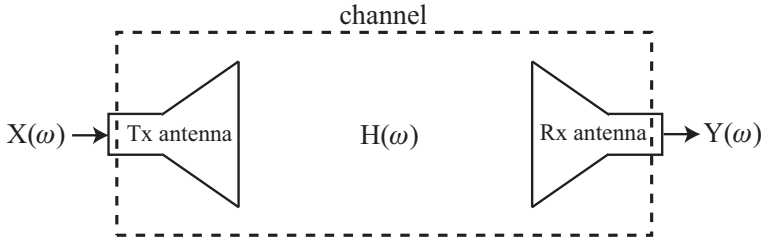

Figure 4.2.: Transfer function of two antennas system.

Two different methods to obtain the transfer function of a two antenna system are described in the following subsections. The first is based on the antenna effective height which is described in [1],[4] and is mostly used for antenna characterization in the time domain, but it can be used as well in the frequency domain. The second method is defined in the frequency domain and is derived from the Friis transmission equation. It has been studied by Pozar in [5].

4.2.1. Effective Height Approach

The impulse response of an antenna system is obtained from the definition of effective height of both transmitting and receiving antennas. Balanis [6] uses the term *effective length* $\boldsymbol{\ell}_e$ instead of effective height $\mathbf{h}$. It relates the radiated electric field $\mathbf{E}$ to the current at the transmitting antenna terminals I_{in} (4.2) and the incident field $\mathbf{E}^i$ to the open-circuit voltage V_{oc} of the receiving antenna (4.3).

$$\mathbf{E}(\hat{\mathbf{r}},\omega) = -j\frac{k\eta}{4\pi r} I_{in}(\omega)\mathbf{h}^t(\hat{\mathbf{r}},\omega)e^{-jkr} \tag{4.2}$$

$$V_{oc}(\omega) = \mathbf{E}^i(\hat{\mathbf{r}},\omega)\mathbf{h}^r(\hat{\mathbf{r}},\omega) \tag{4.3}$$

where $\eta = \sqrt{\mu/\epsilon}$ is the characteristic impedance of the medium, k the wave number ($k = 2\pi/\lambda$), r is the distance from the antenna to the point were the radiated field is measured and $\hat{\mathbf{r}} = \mathbf{r}/r$. To avoid confusion, we distinguish the transmitting antenna effective height $\mathbf{h}^t$ from the receiving antenna effective height $\mathbf{h}^r$.

Considering a two antenna system where the radiated field of the transmitting antenna is the incident field at the receiving antenna, the following expression is derived:

$$V_{oc} = -j\eta\frac{kI_{in}(\omega)}{4\pi r}\mathbf{h}^t(\hat{\mathbf{r}},\omega)\mathbf{h}^r(\hat{\mathbf{r}},\omega)e^{-jkr} \tag{4.4}$$

where r now represents the distance between the two antennas. The ratio of the received to input signal V_{oc}/I_{in} represents the transfer function of the system.

Equations (4.4),(4.3) and (4.2) use only scalar and static values of current, voltage and field. As mentioned before, the system impulse response is a time domain expression, therefore in order to calculate it we must also define the corresponding time domain variables. This is done in the following subsections using the antenna circuit representation as in [4].

4.2.1.1. Transmitting antenna

Considering the circuit representation of a transmitting antenna in Fig. 4.3, the effective height of a transmitting antenna $\mathbf{h}^t$ [m/s^2] relates the incident current at the antenna terminal $I^+(t)$ and the electric field in the far-field via the following convolution*:

$$\mathbf{E}(\mathbf{r},t) = -\frac{\mu}{4\pi r}\Big[I^+(t-r/c) * \mathbf{h}^t(\hat{\mathbf{r}},t-r/c)\Big] \tag{4.5}$$

From Fig. 4.3, $I^+(t)$ is related to the source voltage $V_g(t)$ by

* $f(t) * g(t) = \int f(t')g(t-t')dt'$

$$I^{+}(t) = \frac{V_g(t - t_g)}{2Z_0} \tag{4.6}$$

where t_g is the time delay along the input line. Replacing $I^{+}(t)$ in (4.5), the radiated field at far-field is given by

$$\mathbf{E}(\mathbf{r}, t) = -\frac{\eta}{8\pi r c Z_0}\Big[V_g(t - t_g) * \mathbf{h}^t(\hat{\mathbf{r}}, t - t_g)\Big] \tag{4.7}$$

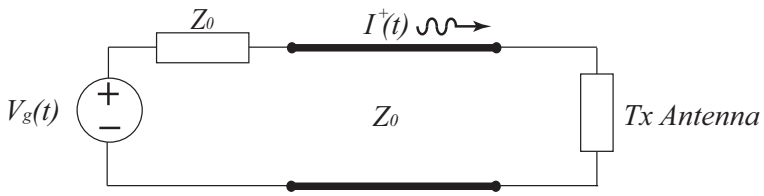

Figure 4.3.: Transmitting antenna circuit

4.2.1.2. Receiving antenna

Assuming that the incident field at the receiving antenna

$$\mathbf{E}^i(\mathbf{r}, t) = \mathbf{E}_0(t - \hat{\mathbf{r}}^i \cdot r/c) \tag{4.8}$$

is a pulsed plane wave where $\mathbf{E}_0(t)$ has a an arbitrary wave form and is polarized perpendicular to the propagation direction $\hat{\mathbf{r}}^i$. The traveling wave $V^{-}(t)$ at the antenna terminal connected to a frequency-independent impedance Z_0 and terminated by a matched load, can be defined by

$$V^{-}(t) = -[\mathbf{E}_0(t) \star \mathbf{h}^r(\hat{\mathbf{r}}, t)] \tag{4.9}$$

where $\star$ denotes a temporal convolution with a spatial scalar product[†].

From the reciprocity theorem (developed in Appendix **??**) the relation between antenna effective heights of a transmitting and a receiving antenna is

$$\frac{1}{2}\mathbf{h}^t(\hat{\mathbf{r}}, t) = \partial_t \mathbf{h}^r(\hat{\mathbf{r}}, t) \tag{4.10}$$

[†] $\mathbf{f}(t) \star \mathbf{g}(t) = \int \mathbf{f}(t') \cdot \mathbf{g}(t - t')dt'$

The current at the antenna terminals in Fig. 4.4 when the antenna is matched to the line ($Z = Z_0$) is given by

$$I_L(t) = \frac{V^-(t - t_L)}{Z_0} \tag{4.11}$$

where t_L is the propagation delay in the line. Combining (4.9) and (4.10)

$$I_L(t) = -\frac{1}{2Z_0}[\mathbf{h}^t(\hat{\mathbf{r}}, t - t_L) \star \partial_t^{-1}\mathbf{E}_0(t - t_L)] \tag{4.12}$$

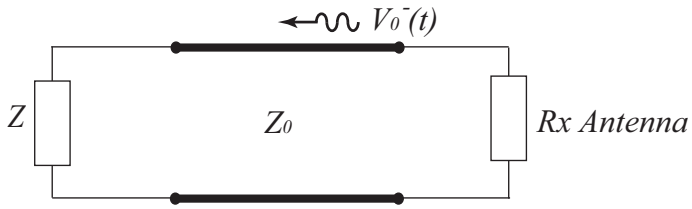

Figure 4.4.: Receiving antenna circuit

4.2.1.3. Transmit-Receive antenna system

Considering the two antenna system in Fig. 4.2 and assuming that the antennas are in the far field from each other, the current at the Rx antenna load is obtained combining (4.7) and (4.12)

$$I_L(t) = -\frac{\eta}{16\pi r c Z_{0_T} Z_{0_R}}[\mathbf{h}_T^t(\hat{\mathbf{r}}_{TR}, \tau - t_g - t_L) \star \mathbf{h}_R^t(\hat{\mathbf{r}}_{RT}, \tau - t_g - t_L) * \partial_t^{-1} V_g(\tau - t_g - t_L)] \tag{4.13}$$

where $\tau = t - r/c$ and ∂^{-1} and the convolution operations are commutable. This equation (4.13) is of the type $y(t) = h(t) * x(t)$. Where the current at the receiving antenna load is the output of the system ($I_L(t) = y(t)$), and the voltage at the transmitting antenna generator its input ($V_g(t) = x(t)$). Therefore the impulse response $h(t)$ is a factor of the convolution between the effective heights of the antennas ($\mathbf{h}_T^t(\hat{\mathbf{r}}_{TR}, \tau - t_g - t_L) \star \mathbf{h}_R^t(\hat{\mathbf{r}}_{RT}, \tau - t_g - t_L)$).

Lets now define the gain of a transmitting antenna using the definition in [4] as:

$$\mathbf{g}^t(\hat{\mathbf{r}}, \xi) = \frac{1}{4\pi c^2}\frac{\eta}{Z_0}\mathcal{R}_{\mathbf{g}^t}(\hat{\mathbf{r}}, \xi) \tag{4.14}$$

where $\mathcal{R}_{\mathbf{g}^t}(\hat{\mathbf{r}},\xi)$ is the vector auotcorrelation[‡] of $\mathbf{h}^t$. Defining the power received at the load as $P_L(t) = ||I_L(t)||^2 Z_{0_R}$ and input power at the transmitting antenna as $P_{in} = \frac{1}{4}||V_g(t)||/Z_{0_T}$, and replacing in (4.13)

$$P_L(t) = -\left(\frac{2\pi c}{4\pi r}\right)^2 \mathbf{g}_T^t(\hat{\mathbf{r}},\xi) \star \mathbf{g}_R^t(\hat{\mathbf{r}},\xi)\partial_t^{-2} * P_{in}(t) \tag{4.15}$$

We will now change the equation above into the frequency domain. Applying the Fourier transform and knowing that $\partial_t^{-2} \overset{\mathfrak{F}}{\longleftrightarrow} (-j\omega)^{-2}$ the following expression is obtained:

$$P_L(\omega) = -\left(\frac{\lambda}{4\pi r}\right)^2 \mathbf{g}_T^t(\hat{\mathbf{r}},\omega)\mathbf{g}_R^t(\hat{\mathbf{r}},\omega)P_{in}(\omega) \tag{4.16}$$

which is the Friis transmission equation.

We have shown that the impulse response of an antenna system is formed by the antennas effective height in time domain. Further more, the relation between the impulse response (time domain) and the Friis transmission equation (frequency domain) was demonstrated. In the following section, the Friis transmission equation will be used to calculate the transfer function of an antenna system.

4.2.2. Friis Transmission Equation Approach

The effective height is a time domain parameter which could be difficult to obtain with conventional antenna measurement equipment. The induced current in the antenna surface cannot be directly measured, but it can be calculated with computational electromagnetic techniques. Most antenna definitions and measurement equipments are in the frequency domain. Therefore a frequency definition of transfer function is more practical to obtain for antenna designers.

4.2.2.1. Friis Transmission Equation

The Friis equation [7] or Friis transmission equation [6] is fundamental for the analysis and design of radar and wireless communications systems. It relates the received power to the transmitted power between two antennas that are separated by a distance R which is larger than the far-field condition ($R > 2D^2\lambda$, where D is the largest dimension of the antennas).

If the transmitting antenna in Fig. 4.5 is isotropic, the power density radiated by the antenna at a distance R is given by

$$S_{iso} = e_{Tx}\frac{P_{Tx}}{4\pi R^2} \qquad [\mathrm{W/m^2}] \tag{4.17}$$

where e_{Tx} is the radiation efficiency of the Tx antenna and P_{Tx} the input power at the antenna terminals. The radiated power density of a non-isotropic antenna in the direction θ_{Tx}, ϕ_{Tx}

[‡] $\mathcal{R}_X(\xi) = \int X(t)X(t-\xi)dt, \qquad ||X(\xi)||^2 = \mathcal{R}_X(0)$

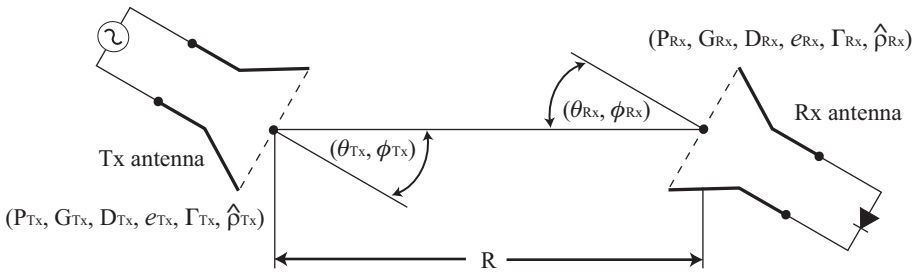

Figure 4.5.: Geometrical orientation of Tx and Rx antennas for Friis transmission equation. (adapted from [6] pp.94)

depends on the antenna gain $G_{Tx}(\theta_{Tx}, \phi_{Tx})$ and hence its directivity $D_{Tx}(\theta_{Tx}, \phi_{Tx})$. It can be written as

$$S_{Tx} = \frac{P_{Tx} G_{Tx}(\theta_{Tx}, \phi_{Tx})}{4\pi R^2} = e_{Tx} \frac{P_{Tx} D_{Tx}(\theta_{Tx}, \phi_{Tx})}{4\pi R^2} \tag{4.18}$$

The effective area of the receiving antenna is related to its directivity as

$$A_{Rx} = e_{Rx} D_{Rx}(\theta_{Rx}, \phi_{Rx}) \left(\frac{\lambda^2}{4\pi} \right) \tag{4.19}$$

where e_{Rx} is the radiation efficiency of the Rx antenna and $D_{Rx}(\theta_{Rx}, \phi_{Rx})$ its directivity.

The received power P_{Rx} is proportional to the incident power density and the antenna effective area ($P_{Rx} = A_{Rx} S_{iso}$). Using (4.18) and (4.19) we can write the ratio of the received to input power as

$$\frac{P_{Rx}}{P_{Tx}} = e_{Tx} e_{Rx} \frac{D_{Tx}(\theta_{Tx}, \phi_{Tx}) D_{Rx}(\theta_{Rx}, \phi_{Rx}) \lambda^2}{(4\pi R)^2} \tag{4.20}$$

The equation above is called the Friis transmission equation. It assumes that the antennas are matched to their loads and that the polarization of the receiving antenna is matched to the incident wave. If these two conditions are not satisfied equation (4.20) becomes

$$\frac{P_{Rx}}{P_{Tx}} = e_{Tx} e_{Rx} (1 - |\Gamma_{Tx}|^2)(1 - |\Gamma_{Rx}|^2) D_{Tx}(\theta_{Tx}, \phi_{Tx}) D_{Rx}(\theta_{Rx}, \phi_{Rx}) \left(\frac{\lambda}{4\pi R} \right)^2 |\hat{\boldsymbol{\rho}}_{Tx} \cdot \hat{\boldsymbol{\rho}}_{Rx}|^2 \tag{4.21}$$

where $|\hat{\boldsymbol{\rho}}_{Tx} \cdot \hat{\boldsymbol{\rho}}_{Rx}|^2$ is the *polarization loss factor*.

The free-space loss factor $(\lambda/4\pi R)^2$ takes into account the losses due to the spherical spreading of the energy by the antenna. It shows as well that the received power decreases by a factor $1/R^2$ when the distance between the Tx and Rx antennas increases.

The transfer function is defined as the ratio between the voltage received at the Rx-antenna terminals (V_L) and the voltage at the input of the Tx-antenna (V_0) [5]. Knowing that $P_{Rx} = V_L^2/Z_L$ and $P_{Tx} = V_0^2/Z_0$ the transfer function $H(\omega)$ can be obtained from the

square root of Friis' transmission equation

$$\left|\frac{V_L}{V_0}\right| = e_{pol}\sqrt{\frac{Z_0}{Z_L}}\sqrt{G_{Tx}(1-|\Gamma_{Tx}|^2)}\left(\frac{\lambda}{4\pi R}\right)\sqrt{G_{Rx}(1-|\Gamma_{Rx}|^2)}|\hat{\boldsymbol{\rho}}_{Tx}\cdot\hat{\boldsymbol{\rho}}_{Rx}| \tag{4.22}$$

where $e_{pol} = \sqrt{e_{Tx}e_{Rx}}$.

The Friis transmission equation relates power, therefore no phase is involved in the calculations. When we calculate the ratio between voltages, the phase of the fields involved is crucial. In order to obtain the phase of $H(\omega)$, the phase of the channel and the phase distortion due to the antennas should be considered. The phase change in the channel is obtained from the universal function e^{-jkr}, which gives the radial dependance of a radiated field. The phase distortion produced by each antenna (Φ_{Tx} and Φ_{Rx}) has an important effect on the pulse shape and the added time delay is considerable. The phase of the transfer function will be given by the channel and the antennas radiated E-field as follows:

$$\angle H(\omega) = -\Phi_{Tx} - kR + \Phi_{Rx} \tag{4.23}$$

The system transfer function $H(\omega)$ can be separated in order to have three transfer functions: of the transmitting antenna H_{Tx}, the receiving antenna H_{Rx} and the channel H_{CH}. It is normally represented in the frequency domain as:

$$H(\omega,\theta,\phi) = H_{Tx}(\omega,\theta,\phi)H_{CH}(\omega)H_{Rx}(\omega,\theta,\phi) \tag{4.24}$$

Where H_{Tx} and H_{Rx} depend on the orientation of the antenna and the frequency. The channel is assumed as free-space, being equal in every direction. Therefore it is not dependent on the direction, but only on frequency.

4.2.2.2. Two-Identical-Antenna System

In order to obtain the transfer functions of the receiving and the transmitting antennas, a two-identical antennas system is analyzed. The input impedance, gain and reflection coefficient are the same for both antennas ($Z_{Tx} = Z_{Rx} = Z_A$, $G_{Tx} = G_{Rx} = G_A$ and $\Gamma_{Tx} = \Gamma_{Rx} = \Gamma_A$). For simplicity the two antennas are located at the same plane and with the same polarization $e_{pol} = 1$ and $|\hat{\boldsymbol{\rho}}_{Tx}\cdot\hat{\boldsymbol{\rho}}_{Rx}| = 1$. Friis transmission equation (4.22) is then simplified to

$$\left|\frac{V_L}{V_0}\right| = (1-|\Gamma_A|^2)\frac{\lambda}{4\pi R}G_A \tag{4.25}$$

From Kern's plane-wave scattering theory [8], the transmitting and receiving transfer functions are defined as:

$$H_{Tx}(\omega) = jkS_{10}(\omega) \tag{4.26}$$

$$H_{Rx}(\omega) = 2\pi S_{01}(\omega) \tag{4.27}$$

where S_{10} and S_{01} represent the scattering matrix elements of the receiving and transmitting properties of an antenna, and are related by the reciprocity theorem

$$Y_0 S_{10}(\omega) = Y_A S_{01}(\omega) \tag{4.28}$$

where Y_0 is the free-space admittance and Y_A the characteristic admittance of the receiving antenna. We can now show that the transmitting transfer function of an antenna is related to the receiving transfer function of the same antenna via [9],[10]

$$H_{Tx} = \frac{jkY_0}{2\pi Y_A} H_{Rx} \tag{4.29}$$

this relation satisfies the reciprocity theorem (Appendix A), as a derivative in time is a multiplication by $j\omega$ in the frequency domain. Substituting $k = \omega/c$, the equation above can then be written as

$$H_{Tx} = \frac{j\omega Y_0}{2\pi c Y_A} H_{Rx} \tag{4.30}$$

The complete definition of the antennas transfer function is then defined as

$$|H_{Tx}|\, e^{-j\Phi_{Tx}} = \frac{Y_0}{Y_A}\frac{\omega}{2\pi c}\, |H_{Rx}|\, e^{j\Phi_{Rx}} e^{-j\frac{\pi}{2}} \tag{4.31}$$

From equations (4.25) and (4.23) the channel transfer function is defined as

$$H_{CH} = \frac{\lambda}{4\pi R} e^{-jkR} \tag{4.32}$$

Substituting (4.32) and (4.31) in (4.24) and (4.23) yields

$$|H(\omega)| = \frac{Y_0}{Y_A}\frac{\omega}{2\pi c}\, |H_{Rx}|\, |H_{CH}|\, |H_{Rx}| \tag{4.33}$$

$$\angle H(\omega) = \Phi_{Rx} - kR + \Phi_{Rx} - \frac{\pi}{2} \tag{4.34}$$

and solving for H_{Rx} and H_{Tx} using (4.25)

$$H_{Rx} = \sqrt{\frac{2\pi c(1-|\Gamma_A|^2)G_A}{\omega}}\, e^{j\Phi_{Rx}} \tag{4.35}$$

$$H_{Tx} = \sqrt{\frac{\omega(1-|\Gamma_A|^2)G_A}{2\pi c}}\, e^{j\Phi_{Rx}} e^{-j\frac{\pi}{2}} \tag{4.36}$$

The term $\sqrt{Y_A/Y_0}$ which represents the antenna mismatch with free-space, is included in the gain definition

$$G_A = \frac{Y_A}{Y_0}\frac{4\pi U_{rad}}{P_{in}} \tag{4.37}$$

where U_{rad} is the radiation intensity and P_{in} the total input (accepted) power.

4.2.3. The two approaches: A Comparison

In order to calculate the SFF from simulation results, the system transfer function has to be obtained. This could be achieved using, as shown before, either of the studied approaches. The pros and cons of each approach are analyzed in this section. A final decision is taken about which approach to implement according to the efficiency of the method and the facility to obtain the results from simulation tools available.

The effective height approach defines the transmission coefficient of an antenna system in the time domain. It can be separated, as shown in Fig. 4.6, in the effective heights of the transmitting antenna $\mathbf{h}^t$ and the receiving antenna $\mathbf{h}^r$. The environment is included in each of the effective heights. The radiated and incident fields are identical, therefore the middle point between the two antennas delimits the separation between the heights. The parameters to be calculated are: induced current at the load of the Rx antenna, the input voltage at the Tx antenna terminals and the impedances of each antenna Z_{0_R} and Z_{0_T}. These parameters are in the time domain, therefore cannot be obtained with every simulation tool.

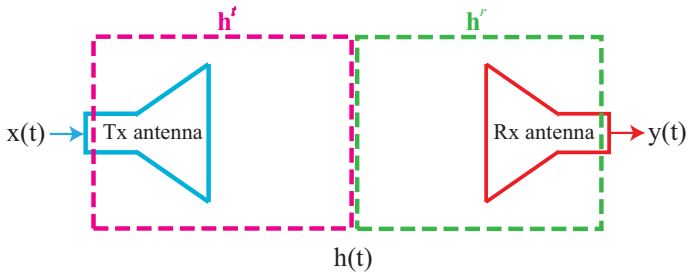

Figure 4.6.: Effective height approach

The parameters needed to calculate the Friis transmission equation for each antenna are: reflection coefficient Γ_A, antenna gain G_A and phase of the radiated E-field Φ_A. These parameters are in the frequency domain and can be calculated with most simulation tools available. An important characteristic of this approach is the fact that the channel is independent of the antennas. The system transfer function can be divided in three transfer functions H_{Tx}, H_{Rx} and H_{CH} (Fig. 4.7), giving one more degree of freedom than with the effective height approach.

Any combination of antennas and channel can be done. Even if for characterizing an antenna (in the conventional manner), the free-space channel is used (anechoic chamber), this approach allows the implementation of the antenna system in any other known environment. This is achieved by the multiplication of the three main elements.

The Friis transmission equation approach was chosen to calculate the transfer function from simulation analysis, due to the following advantages compared with the effective height approach: simulated parameters can be directly calculated with most tools available today and the freedom to select the antennas and the channel separately. Working in frequency

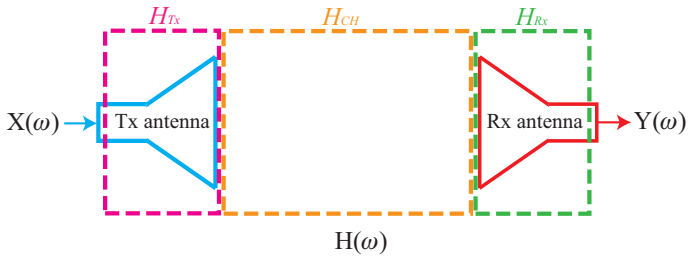

Figure 4.7.: Friis transmission equation approach

domain is as well simpler than in time domain, as noted in (4.1) a convolution in time is a multiplication in frequency. The simulations and post-processing needed to calculate the system's transfer function using the Friis approach are described in the following section.

4.2.4. Simulations

The S_{21} or transfer function of an antenna system can be obtained directly from simulations for a limited distance between antennas and at a large computing cost [11]. One simulation is required for each desired angle in the plane, increasing with this the time needed to obtain the results.

A simple simulation technique to obtain the transfer function is described. From simulations of a single antenna, the transmission coefficient between two identical antennas located at any distance and at any angle of rotation (in the azimuth plane) is calculated. From the two identical antennas transfer function $H(\omega)$, the transfer functions of each antenna H_{Tx} and H_{Rx} are obtained using equations 4.35 and 4.36. The transfer function of an antenna system composed of two different antennas can be directly obtained by combining the Tx and Rx of the desired elements.

The antenna gain G_A and reflection coefficient Γ_A are obtained from simulations of a single antenna. Simulations should be done over a band larger than the UWB. All simulations in this thesis were done using a discrete sweep in the band: 0.05MHz−20.05GHz with 201 points. These values were chosen in order to match with the measured values, covering all the VNA band. The radiation box is set to be at least 25mm ($\lambda/4$ @ 3GHz) larger than the antenna in every direction.

The $H(\omega)$ of a two identical antenna system is calculated using equation (4.25), assuming no polarization losses $e_{pol} = 1$ (antennas pointing angles are the same) and $\Gamma_{Tx} = \Gamma_{Rx} = S_{11}$, as the Tx and Rx antennas are identical. We have

$$H(\omega) = \left|\frac{V_L}{V_0}\right| = (1 - |S_{11}|^2)\frac{\lambda}{4\pi r}G_A(\omega, \theta, \phi)e^{-jkR}e^{2j\Phi_A(\omega,\theta,\phi)} \tag{4.38}$$

The phase distortion of the antennas Φ_A is obtained directly from simulations. In the specific case of HFSS, the value rE is the radiated electric field multiplied by the radial distance, and depending on the orientation of the antenna, the theta or phi component is

used in ang_rad (E-field phase in radians). This value ($rE[ang\_rad]$) can be used directly in (4.38) and the distance dependence (e^{jkR}) is computed separately.

The antenna gain and E-field phase are calculated at every angle of the desired plane.

$$H_{Rx}(\omega,\theta,\phi) = \sqrt{\frac{2\pi c(1-|S_{11}|^2)G_A(\omega,\theta,\phi)}{\omega}}e^{j\Phi_A(\omega,\theta,\phi)} \tag{4.39}$$

$$H_{Tx}(\omega,\theta,\phi) = \sqrt{\frac{\omega(1-|S_{11}|^2)G_A(\omega,\theta,\phi)}{2\pi c}}e^{j\Phi_A(\omega,\theta,\phi)}e^{-j\frac{\pi}{2}} \tag{4.40}$$

From the equations above, the transfer function of the two identical antennas (Tx and Rx) can be simultaneously calculated for any point in the space. The system transfer function can then be obtained with the combination of any two antennas, solving $H(\omega)$ for each antenna and then substituting H_{Rx} and H_{Tx} of the desired antennas in (4.24). If the transmitting antenna is oriented at $\phi = 0°$ and the receiving antenna is rotated every ϕ point, we can characterize the antenna system in the azimuthal plane of the Rx antenna as

$$H(\omega,\theta,\phi) = H_{Tx}(\omega,\theta=90°,\phi=0°)H_{CH}(\omega)H_{Rx}(\omega,\theta,\phi) \tag{4.41}$$

Example:

Calculate the transfer function (S_{21}) of a two-antenna system in free-space. Having: Antenna 1 = Transmitting and Antenna 2 = Receiving. In the azimuthal plane of the Rx antenna, every $\theta = 10°$. The Tx antenna radiating at $\phi = 90°, \theta = 0°$.

Antenna 1
Simulate Antenna 1 and obtain:
$G_1(\phi = 90°, \theta = 0°)$ = Gain
Γ_1 = Reflection coefficient
$\Phi_1(\phi = 90°, \theta = 0°)$ = rE[ang_rad]

Calculate the transfer function of the Tx antenna using the simulated values in (4.40)

$$H_1(\omega,\phi=90°,\theta=0°) = \sqrt{\frac{\omega(1-|\Gamma_1|^2)G_1(\omega,\phi=90°,\theta=0°)}{2\pi c}}e^{j\Phi_1(\omega,\phi=90°,\theta=0°)}e^{-j\frac{\pi}{2}}$$

Antenna 2
Simulate Antenna 2 and obtain:
$G_2(\omega, \phi = 90°, \theta)$ = Gain (for every $\theta = 10°$)
Γ_2 = Reflection coefficient
$\Phi_2(\omega, \phi = 90°, \theta)$ = rE[ang_rad] (for every $\theta = 10°$)

Calculate the transfer function of the Tx antenna using the simulated values in (4.39)

$$H_2(\omega, \phi = 90°, \theta) = \sqrt{\frac{2\pi c(1 - |\Gamma_2|^2)G_2(\omega, \phi = 90°, \theta)}{\omega}} e^{j\Phi_2(\omega, \phi = 90°, \theta)}$$

Free-space Channel
Calculate the transfer function of the free-space channel for the desired distance between the antennas R (it can be chosen freely)

$$H_{CH}(\omega) = \frac{\lambda}{4\pi R} e^{-jkR}$$

S_{21}
Multiply the transfer functions of Antenna 1, Antenna 2 and the Channel:

$$S_{21} = H_1(\omega, \phi = 90°, \theta) H_{CH}(\omega) H_1(\omega, \phi = 90°, \theta = 0°) \tag{4.42}$$

4.2.5. Measurements

Measurements of the S-parameters of the antenna system are done inside an anechoic chamber using a Vector Network Analyzer (VNA). The measurement setup used in this work is shown in Fig. 4.8. Each antenna is connected to a port of the HP 8720D network analyzer with a high quality cable [12]. The cables are 3.5 m long, which allows to connect the antennas to the VNA located outside the chamber as shown in Fig. 2.11. An electronic calibration kit HP85060C is used to calibrate the VNA at the antennas ports. The calibration is done over all its working band (50 MHz - 20.05 GHz). It is important to use all this band because this information will be used later to calculate the received pulse in time domain. A frequency band larger than the pulse spectrum is needed to recover the full information of the signal. This is explained more in detail in Section 4.3, where the Nyquist theorem is defined.

A foam frame was created specially for this application. It is 1.09 m long and can support an antenna on each end. According to the symmetry of the antenna an SMA right angle connector from [13] can be used to arrange the antenna in its optimal position. One of the antennas is fixed (Tx) while the other antenna (Rx) is rotated in the azimuthal plane. A new S_{21} measurement is done at every desired angle. The Rx antenna is connected to the cable using a SMA push-on [12]. This allows the rotation of the antenna without affecting its matching to the cable.

4.3. Time Signal

Ultra-wideband Impulse Radio (UWB-IR) sends very short pulses in time (< 2 ns) covering a very broad frequency spectrum. As the pulses are short, they are greatly affected by dispersion. The pulse at the receiving antenna port (R_S) will never be the same as the transmitted pulse (T_S). However, the receiver should recognize the incoming pulse. For

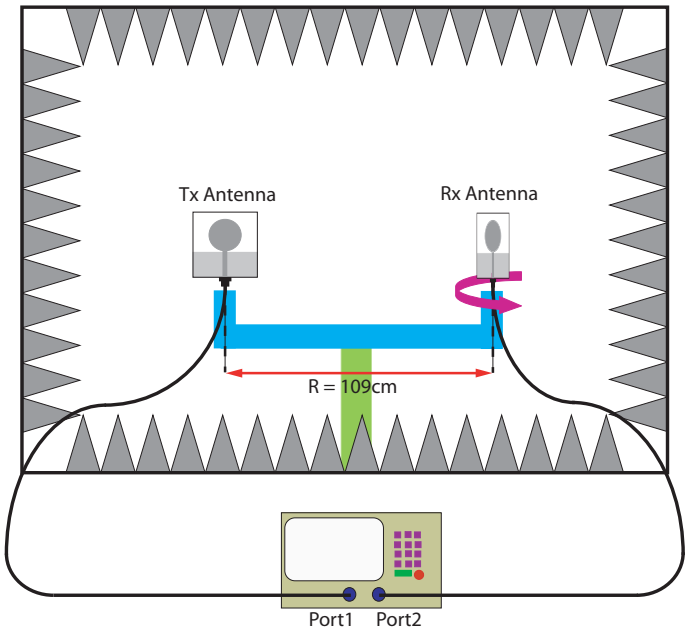

Figure 4.8.: Measurement setup inside an anechoic chamber.

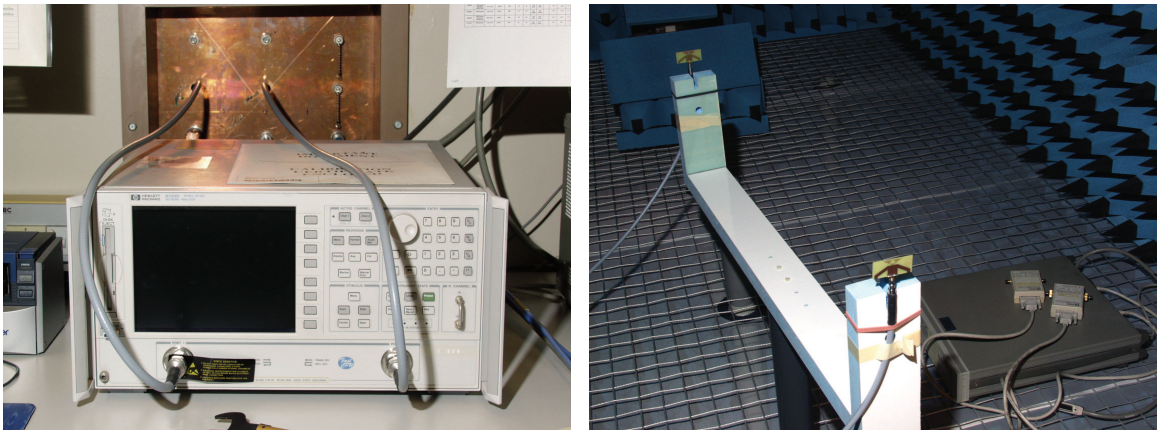

(a) (b)

Figure 4.9.: Measurement setup: (a) Setup of HP 8720D Network Analyzer outside anechoic chamber, (b) Antennas in foam support and calibration kit inside anechoic chamber.

this reason a time domain analysis of the transmitted pulse is done, in order to predict the dispersion produced by the system.

In general it is not possible to have a signal generator inside an anechoic chamber, because of lack of space or the negative effect it has on the measurements. Furthermore, most antenna simulation softwares use frequency techniques analysis. Therefore, the antenna analysis is done in frequency domain and this information is post-processed to obtain the time domain signal. This is a straightforward procedure and any input signal can be used.

The input pulse at the transmitting antenna is defined according to specific requirements (bandwidth, center frequency, amplitude, etc.). The sampling time interval T_S should be set in order to satisfy Nyquist theorem [14] ($F_S > 2f_H$, where f_H is the highest frequency point in the -10 dB bandwidth of the input pulse spectrum), as T_S is inversely proportional to the the sampling frequency $F_S = 1/T_S$. The received pulse will be plotted in the same interval as the input pulse. Therefore extra points should be added at the end in order to have enough points for the delayed received pulse to fit in. The total number of points N is a factor of the frequency interval Δf given by simulations and measurements and the sampling frequency F_S ($N = F_S/\Delta f$). A fast fourier transform FFT is done to calculate the input pulse in the frequency domain, the resulting spectrum containing the same number of points N as the time domain signal.

The input pulse can be defined using Matlab [15]. It can be defined manually or by using the *gauspuls* routine where the central frequency (fc) in Hertz, the fractional bandwidth (bw) and the time interval (t) should be given. The fc and bw depend on the type of pulse needed.

The pulse spectrum is multiplied with the transfer function of the antenna system to obtain the received signal in frequency domain. Applying the inverse fourier transform $IFFT$ the Rx-signal in time is obtained. The following equations denote the mentioned steps

$$R_S(\omega) = FFT(T_S(t))H(\omega) \tag{4.43}$$

$$R_S(t) = IFFT(R_S(\omega)) \tag{4.44}$$

The measured received signal is obtained by substituting the simulated $H(\omega)$ with the measured S_{21}. The received signal will present the distortion and dispersion produced by both antennas and the channel. The best way to quantify this effect is to make a correlation between the input and received pulses. The following subsection describes the proposed System Fidelity Factor, which uses this quantification method.

4.4. System Fidelity Factor

The fidelity factor, as defined in [16], quantifies the degree to which the radiated E-field waveform of a transmitting antenna resembles the driving voltage. This is calculated with the cross-correlation of the radiated E-field and the input signal, as stated in [1]. Nevertheless, it is not always easy to calculate in real applications due to the difficulty to measure or simulate

the radiated E-field. The System Fidelity Factor SFF, on the other hand, uses the standard S_{21} parameter to compare the received R_S and transmitted signal T_S between two antennas, thereby quantifying the degree to which the antenna system affects the input pulse. It takes therefore into consideration the distortion induced by the two antennas, whereas the Fidelity Factor takes into consideration the transmit antenna effect only.

The received and the transmitted pulses, calculated in the subsection above, are normalized as shown in (4.45) and (4.46). The normalization is done in order to compare only the shape of the pulses, and not their magnitude, as R_S is expected to be much lower than T_S.

$$\hat{R}_S(t) = \frac{R_S(t)}{\left[\int_{-\infty}^{\infty} |R_S(t)|^2 dt\right]^{1/2}} \tag{4.45}$$

$$\hat{T}_S(t) = \frac{T_S(t)}{\left[\int_{-\infty}^{\infty} |T_S(t)|^2 dt\right]^{1/2}} \tag{4.46}$$

The cross-correlation between both signals is done at every point in time and the maximum value of this correlation is obtained when both pulses overlap.

$$SFF = \max_{\tau} \int_{-\infty}^{\infty} \hat{T}_S(t)\hat{R}_S(t+\tau)dt \tag{4.47}$$

The SFF in (4.47) has to be computed for every angle (θ or ϕ) and plotted in a polar plot. Because of the normalization of the signals, the results of the cross-correlation are between 0 and 1. An SFF value of 1 indicates that the received pulse is identical to the input pulse, hence no distortion occurred during transmission. A value of 0 means the received pulse is completely different than the one at the Tx-antenna port. The required SFF value needed to accurately detect a desired pulse depends on the application, but we consider that a distortion higher than 50% (SFF < 0.5) will make the pulse almost unrecognizable.

4.5. Application of the SFF

The planar circular monopole was one of the first UWB antenna to be studied [17]. Among the characteristics which make it interesting are its simplicity to design, a good matching across the UWB band and its reduced size, comparable to a dollar cent [18]. Its omnidirectional radiation makes it a good candidate for communication systems. Several designs have been implemented in order to achieve the best antenna performance. Different ground plane topologies have been studied in [2],[19]. It was found that the shape considerably affects the antenna radiation.

UWB directional antennas have been largely studied as well [20], [21]. They consist mostly of tapered or log-periodic antennas that have a high directivity and a constant gain over a large band. These characteristics are of special interest for radar, imaging or base

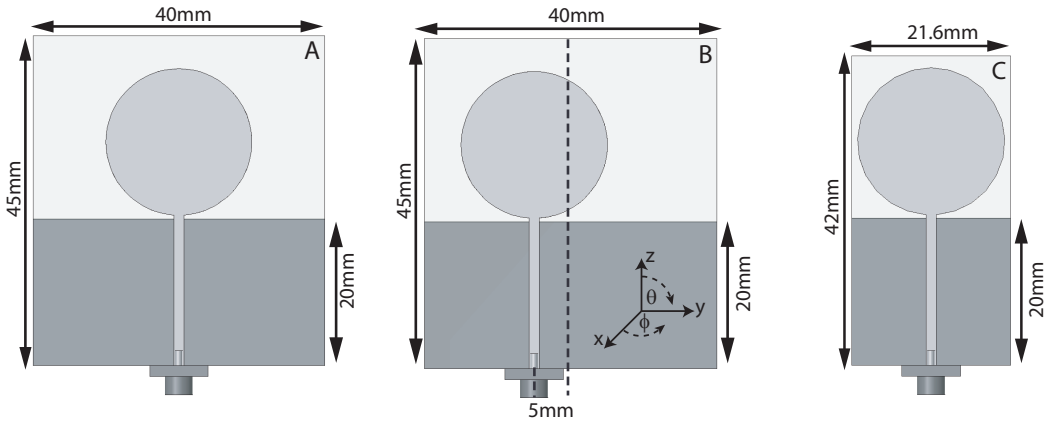

Figure 4.10.: Planar circular monopoles. (a) Monopole A, (b) Monopole B, (c) Monopole C.

station applications. The Vivaldi antenna [22],[23],[24] consists of an exponentially tapered slot fed by a microstrip line. It is a planar structure, therefore has small size compared to other bulky antennas [25].

In this section we will analyze two different systems: the first one is composed of two identical monopoles that are used for transmission and reception, the second system has a vivaldi antenna at transmission and a monopole at reception. We will analyze the systems using the SFF, showing that the method is simple and a good comparison between systems is achieved.

4.5.1. Monopoles

Three circular monopoles with different ground configurations are studied (Fig. 4.10). Monopoles A and B have the same size, but one of them has the radiator shifted from the center of the ground plane. Monopole C has a ground plane considerably smaller. The monopoles were simulated using the full-wave electromagnetic field simulator HFSS, fabricated and measured in an anechoic chamber.

The monopole radiators have a radius of 10 mm and are fed by a 50 Ω microstrip line of 1.4 mm width. They are printed on a FR4-epoxy ($\epsilon_r = 4.4$, $h = 0.8$ mm) substrate. Their S_{11} is lower than -10dB over the UWB band, as shown in Fig. 4.11. The simulated values are shown in dashed lines and the measured values in solid lines. Both results are in good concordance, showing that the antennas are well matched above 2.5GHz. Measurements of Monopole C do not agree with simulations below 3.4 GHz, where the measurement shows that the antenna is not well matched below this value.

From the structure of a circular monopole it can be assumed that the best radiation will be in the direction normal to the antenna surface ($\theta = 90°, \phi = 0°$). However, this is not true for most of planar circular monopoles, as found in [2],[26],[27].

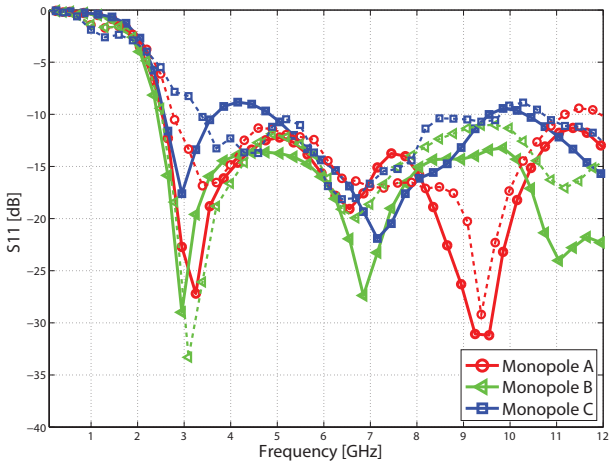

Figure 4.11.: Measured (dashed lines) and simulated (solid lines) reflection coefficient.

Monopole A, shown in Fig. 4.10(a) was first studied by the authors in [27]. Its transfer function $H(\omega)$ with both monopoles facing each other ($\theta = 90°, \phi = 0°$) was calculated and measured. An unexpected behavior at 8.25 GHz was visible, where the amplitude decreased abruptly and the phase presented a non-linearity. This was also found in the three antennas studied in [2]; where a strange radiation behavior was seen at 8.2 GHz. The same artifact was observed in the simulations and measurements made in [26]. This proves that the UWB radiation of the circular monopole is not optimal at boresight, even though this direction could be intuitively thought to be the best.

4.5.2. Vivaldi

In the second system configuration, the Vivaldi antenna is used as a transmitting antenna and the three monopoles described before as receivers. The Vivaldi antenna used is shown in Fig. 4.12(a); it was adapted from the design by Sorgel et al in [28]. Its return loss is below -10 dB in the $4-12$ GHz band (Fig. 4.12(b)). It has been implemented on the same substrate as the monopoles (FR4 $\epsilon_r = 4.4$, $h = 0.8$ mm) with a 50Ω line connected to a SMA connector.

4.5.3. Radiation Pattern

The radiation patterns in the azimuthal plane of the antennas were obtained at 5 frequencies inside the UWB band. The monopoles in Fig. 4.13 have an omnidirectional pattern at the lowest frequencies (3.1, 4.75 and 6.85 GHz) but the pattern is clearly not omnidirectional at 8.725 GHz. Monopole A has a very bad radiation at 8.725 GHz, specially at $\phi = 0°$ and 180°, and it is at this frequency that the cross-polarization level is the highest. Monopole B is clearly not symmetric at the two highest frequency, but at 3.1GHz the asymmetry is not visible and the cross- polarization level is considerably high at all frequencies. Radiation of Monopole C is at least 3dB lower at the sides ($\phi = \pm 90°$) than at the back and forward

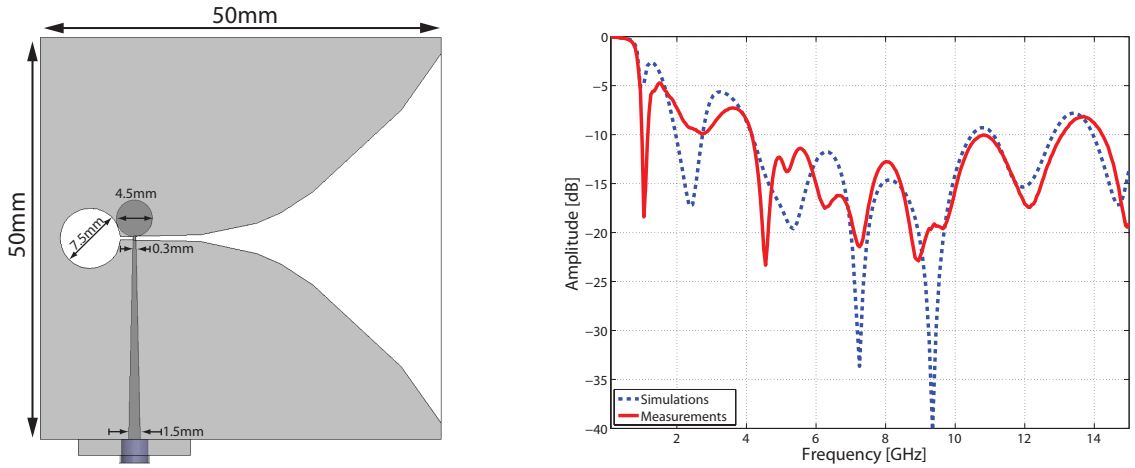

(a) (b)

Figure 4.12.: Vivaldi Antenna. (a) Structure, (b) Return Loss

directions, where it is constant almost at all frequencies. At the highest, frequency the pattern is no longer omnidirectional, but it has a directive shape with around 10 dB higher directivity at $\phi = 0°$ than at $\phi = 180°$. Monopole C presents the lowest cross-polarization at almost all frequencies.

Analyzing the radiation pattern is not very easy, as it is almost impossible to plot all the frequencies of the UWB in the same plot. A big difference in the patterns exist between 8.725 GHz and 10.6 GHz, but the interval between these two frequencies is considerably large (1.85 GHz) and the changes that may occur between the frequencies are unknown. This is the same for almost all omnidirectional UWB antennas, where the pattern changes abruptly in the UWB band.

Directive antennas, on the other hand, have a constant pattern over a broader band at a given aperture angle. This is the case for the studied Vivaldi, as can be seen in Fig. 4.14. The co-polarization in both E and H planes has a constant directivity in the whole the band over at least 10 degrees at boresight ($\phi = 0°$). The backward radiation is at least 10 dB lower for every frequency. At $\phi = \pm 90°$ the pattern is less constant, and has a higher radiation at the lowest frequency (3.1 GHz). The cross-polarization is considerably smaller than with the monopoles, especially in the E-plane. These characteristics are indicators of a small signal distortion over the analyzed band at boresight. However, this is not the only important indicator of distortion, as phase non-linearities might exist but they cannot be analyzed in the radiation pattern.

4.5.4. Gain Pattern

If the antenna radiation pattern is plotted at some frequencies only, the frequency (or frequencies) at which radiation is lower might not be seen. Therefore it is optimal to make a

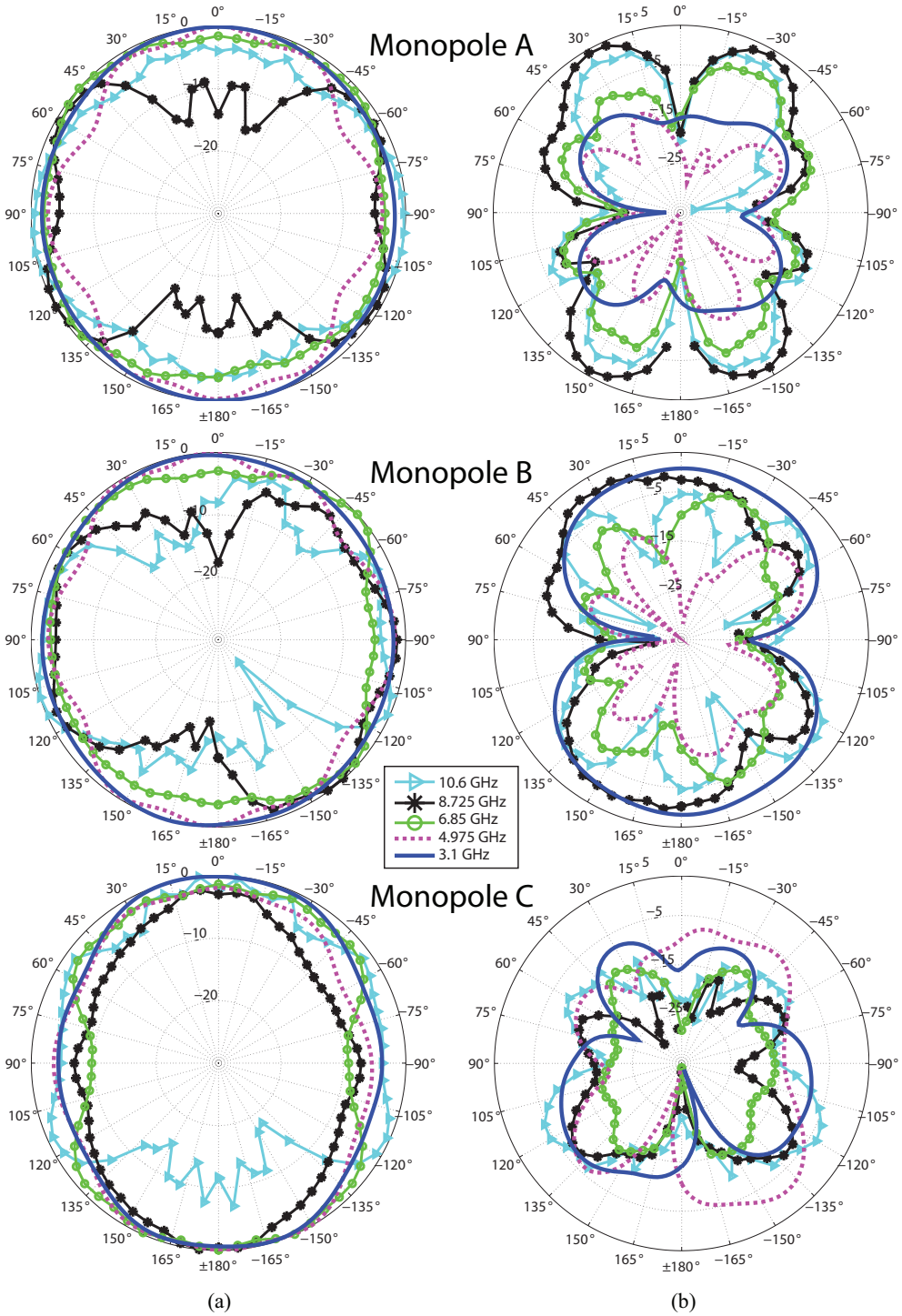

Figure 4.13.: Measured radiation pattern (azimuthal plane ϕ) of Monopole A, B and C. a) Co-polarization, b) Cross-polarization.

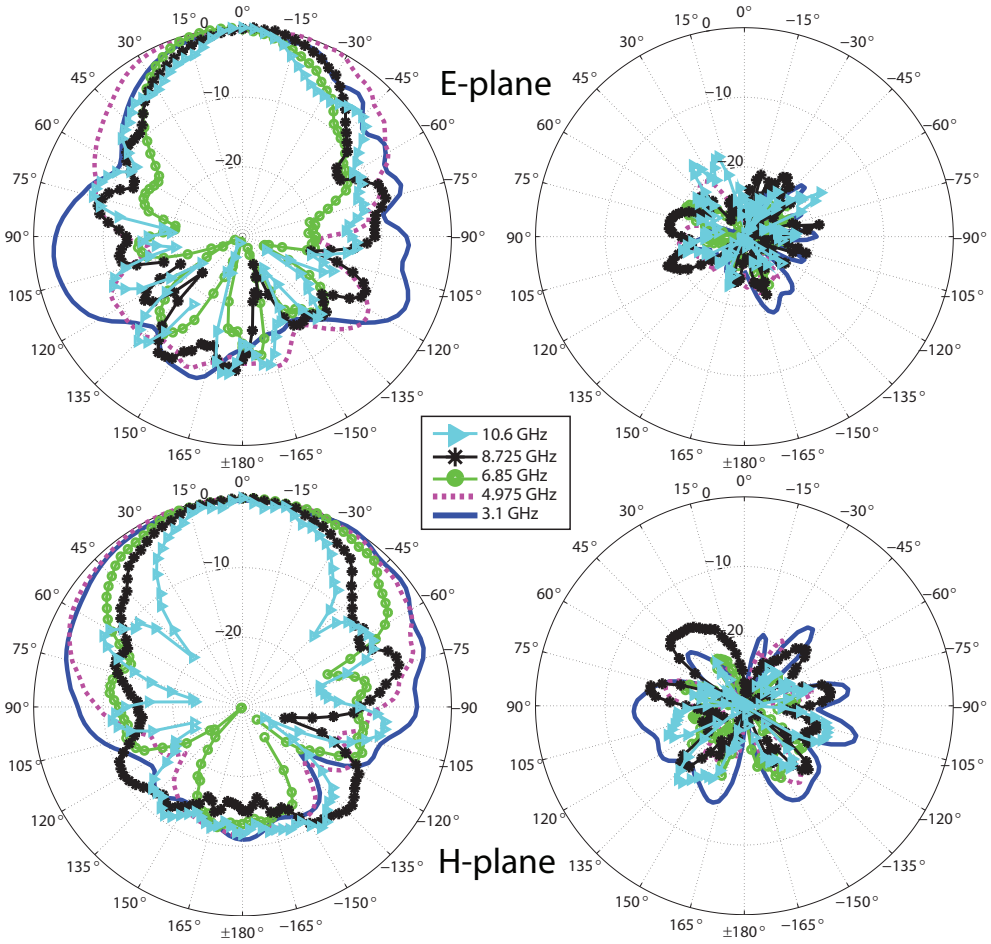

Figure 4.14.: Measured radiation pattern of Vivaldi antenna in the E and H planes. a) Co-polarization, b) Cross-polarization.

pattern analysis at every frequency. One way of representing this is the Gain pattern graph, which plots frequency and angle in a plane.

The gain pattern graph, showing the gain versus frequency and angle in one scan plane, gives a global overview of the radiation performances of an antenna over a frequency band.

The azimuth Gain patterns of each monopole and the Vivaldi antenna are shown in Fig. 4.15. A large difference between the patterns can be observed.

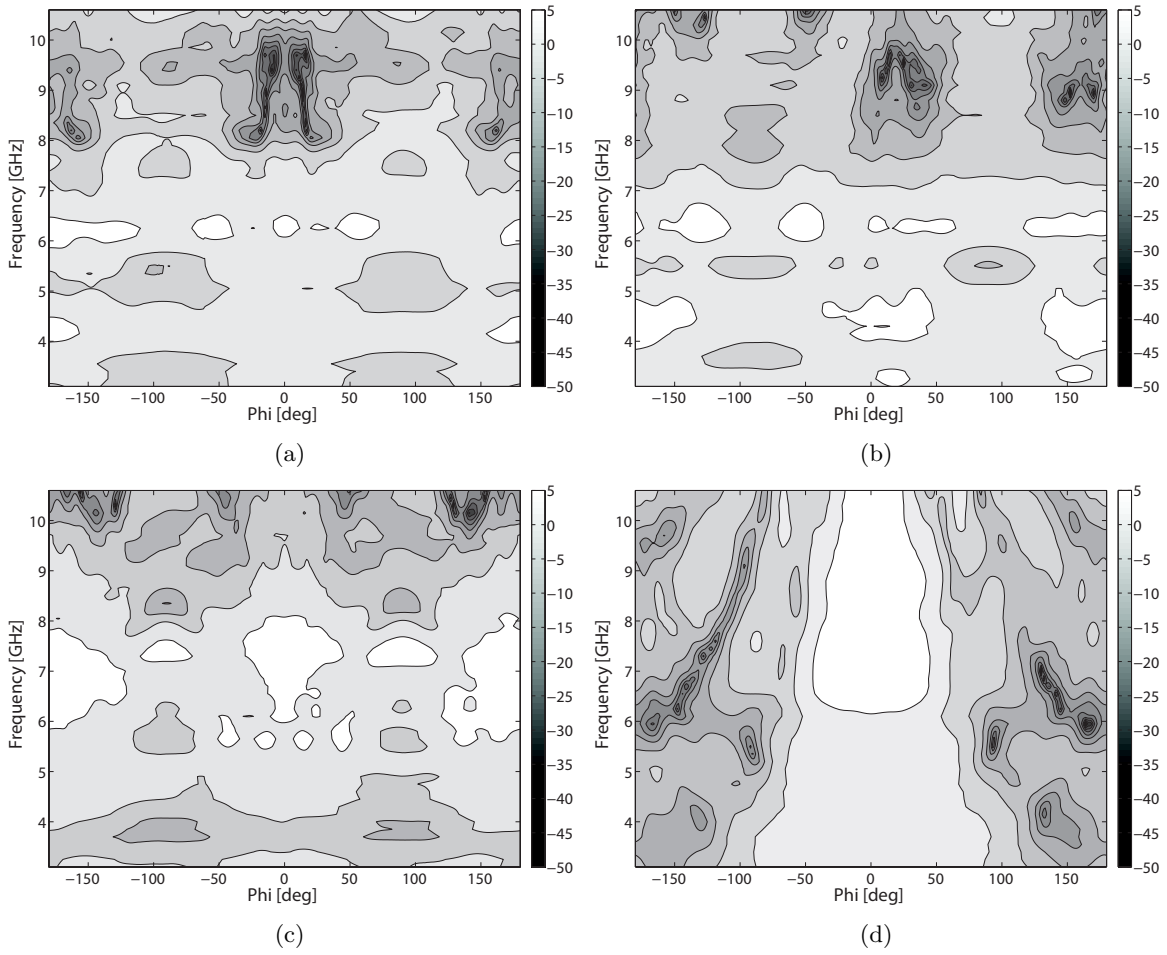

Figure 4.15.: Antenna Gain Pattern. (a) Monopole A, (b) Monopole B, (c) Monopole C, (d) Vivaldi.

Monopole A (Fig. 4.15(a)) has a considerably low gain ($< -40\,\mathrm{dB}$) around $\phi = 0°$, from frequencies above 8.2 GHz and up to 10 GHz. The other monopoles (Fig. 4.15(b) and Fig. 4.15(c)) present as well an important decrease in gain but at different frequencies and angles. As expected, the gain pattern of monopole B is not symmetrical, as it is for the other two. The lowest gain points of the C antenna are located at frequencies above 10 GHz. The Vivaldi antenna has an almost constant gain over the band within the 80°main beam.

Abrupt changes in the gain of an UWB antenna promote dispersion of the transmitted

pulse. This distortion will not be the same in all systems. Gain pattern is a good method to identify where is the optimum radiation of an antenna, but gives no direct information on pulse distortion.

Phase is an important factor that must not be forgotten when analyzing a time signal, but it cannot be obtained with a conventional radiation pattern measurement. One way to obtain the phase in a transmission between two antennas is to measure S_{21}, or the transfer function of the system, which includes both magnitude and phase. This value is the basis to calculate the SFF. The SFF of the proposed monopole systems, together with the intermediate steps described in previous sections (transfer function and time domain signal), are discussed in the following sections.

4.5.5. Monopole-Monopole Systems

The SFF of the antenna systems consisting of two identical monopoles (A, B or C), are presented in this subsection. The transmitting antenna is fixed on one end of the foam support and is facing the Rx antenna ($\phi = 0°$). The Rx antenna is rotated every 10°. The setup is depicted in Fig. 4.16.

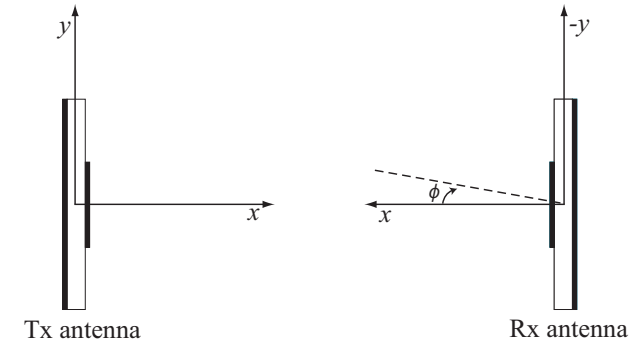

Figure 4.16.: Upper view of Monopole-Monopole system setup.

4.5.5.1. Transfer Function

An ideal UWB antenna has a constant gain over the UWB band. This might be true for $|H(\omega)|$ of an antenna system as well, in order to transmit a pulse without distortion. By plotting $H(\omega)$ over the desired band, we can localize a magnitude drop. If the dip corresponds to a nonlinearity in phase, the transmitted pulse will be distorted. How much will the pulse be distorted? This cannot be answered with $H(\omega)$ alone. Distortion depends on where in the frequency band the dip occurs (a large magnitude drop occurring in the middle of the band might affect more than the same drop at higher frequencies), its magnitude (how deep is the dip) and its phase nonlinearity. This is a further motivation to analyze the system in time domain as well, which contains the phase and magnitude information, and pulse distortion can be quantified.

If the transfer function is analyzed only at some points in the space, the "bad radiation" points might not be seen. Therefore it is important to analyze it in the entire plane. This can be done by plotting $H(\omega)$ for different angles in the same graph, but a conclusion on radiation performance might not be directly obtained. To illustrate this, $H(\omega)$ was obtained at three points in the azimuth plane ($\phi = 0°, 90°$ and $180°$, $\theta = 90°$) and plotted together with the measured S_{21} in Fig. 4.17. This was done for the three antennas.

The dips in magnitude and phase nonlinearities correspond, as expected, to the low gain points in Fig. 4.15.

4.5.5.2. Time Signal

The next step to calculate the SFF is to obtain the received signal in the frequency domain to later transform it into the time domain. This is done, as mentioned in Section 4.3, by multiplying the transfer function (or S_{21}) and the input pulse spectrum. An $IFFT$ is applied to the frequency domain signal and the Rx pulse obtained. The input pulse was obtained using the *gauspuls* matlab function with $fc = 6.85$ GHz, $bw = 0.85$ and a sampling frequency $F_S = 50$ GHz ($T_S = 0.02$ ns).

Again, this result does not infer directly how distorted the transmission will be at any given point. The signal can be obtained for several angles in the plane. This was done for each antenna system, at the same angles used in the previous subsection ($\phi = 0°, 90°$ and $180°$, $\theta = 90°$). As seen in Fig.4.18, the measured and simulated received pulses are almost identical. This confirms the quality of the proposed method.

The Rx signal should be compared to a reference signal, which in our case is the input signal at the Tx antenna port. This is done in order to know how much they differ from each other and in which measure the signal is distorted. In the plots, the Rx signals are clearly different and more dispersed in time than the input signal, however an objective conclusion cannot be drawn. Correlating both signals is one way of quantifying the difference. The SFF uses this method and the results are shown below.

4.5.5.3. System Fidelity Factor

The SFF of the three antennas is plotted in Fig. 4.19. Monopole A has the lowest SFF, which is below 0.75 at every angle. Its radiation in the whole UWB band is clearly not omnidirectional as the SFF is higher at $\phi = \pm 90°$. The simulated values are lower than the measured ones, but both plots are similar in shape. The difference is amplified on the figure by the scale used, having 0.5 at the center of the diagram. This scale is used because we considered that an antenna system having SFF values below 0.5 will distort the pulse in such a way that the received pulse will no longer be recognized.

The main characteristic of antenna B (Fig. 4.19(b)) is its asymmetry. From the plot it is clear that the side of the antenna closer to the ground edge ($\phi = -90°$) presents a better SFF. The difference between the two plots can be attributed to simulation inaccuracies, as phase nonlinearities are not detected by the simulator, as shown in Fig. 4.17(b). Nevertheless, in

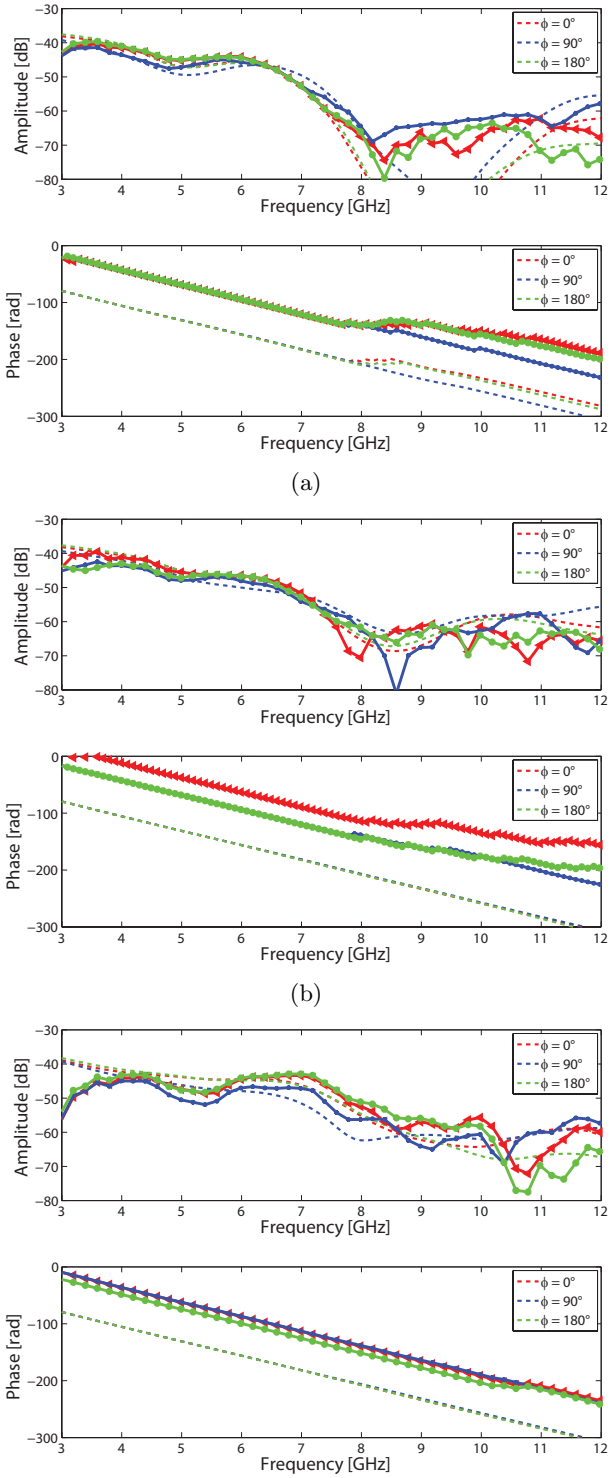

(a)

(b)

(c)

Figure 4.17.: Simulated (dashed lines) and measured (solid lines) transfer function at $\phi = 0°, 90°$ and $180°$, $\theta = 90°$: (a) Monopole A, (b) Monopole B, (c) Monopole C.

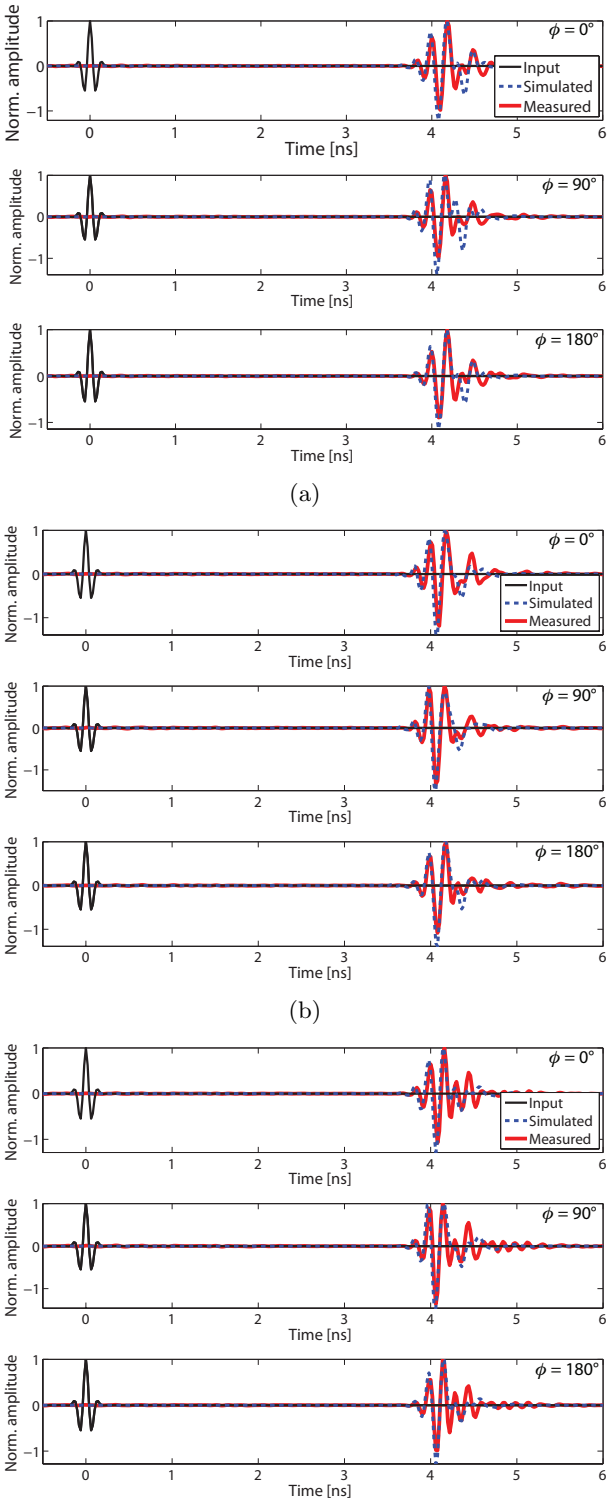

Figure 4.18.: Tx signal and Rx signal (simulated and measured): (a) Monopole A, (b) Monopole B, (c) Monopole C.

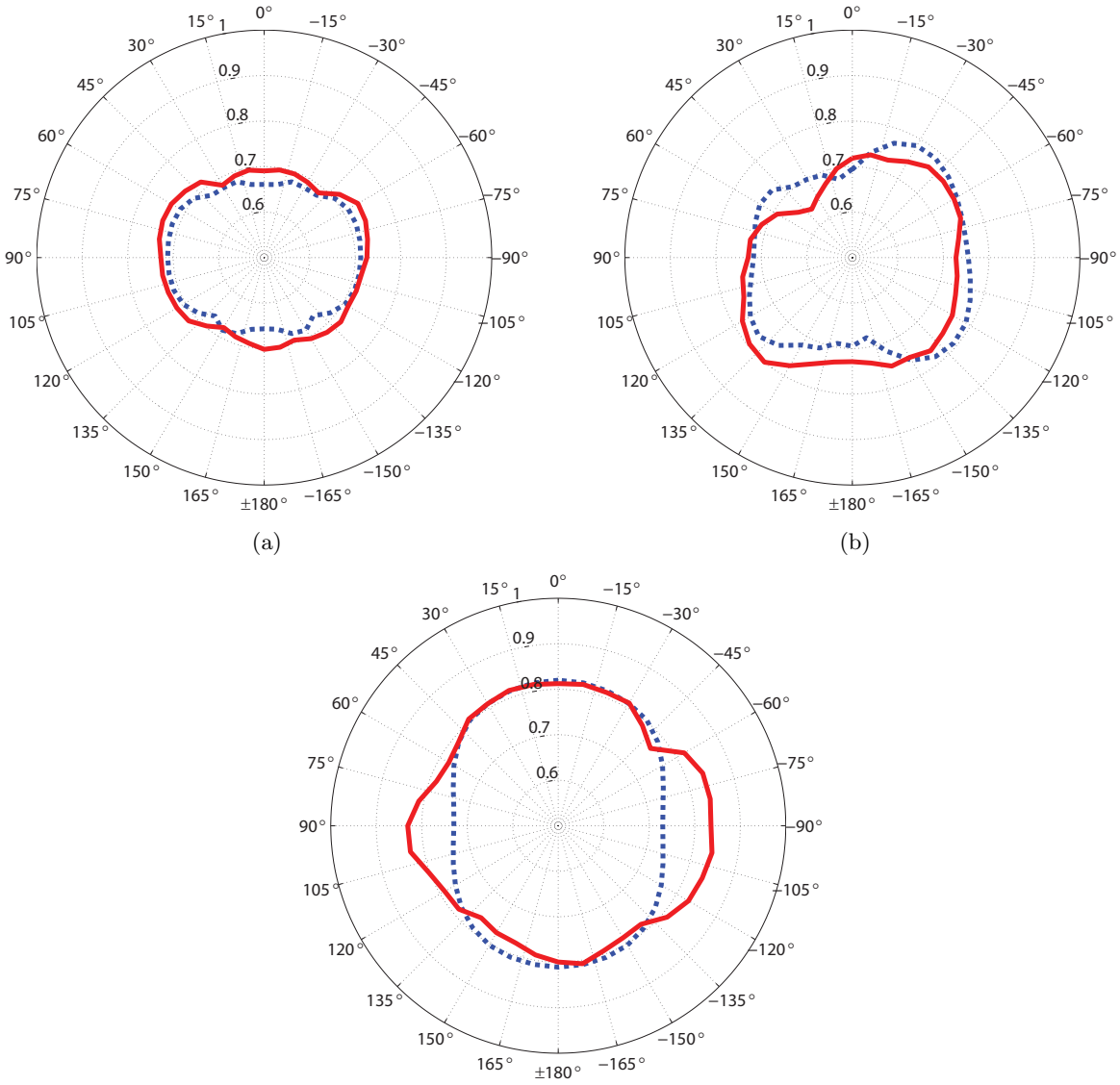

Figure 4.19.: System Fidelity Factor in function of angle ϕ ($\theta = 90°$): Simulated (dashed lines) and measured (solid lines). (a) Monopole A, (b) Monopole B, (c) Monopole C.

both curves a dip is seen between $\phi = 0°$ and $\phi = 90°$. The lowest SFF values are found there as well. The front and backward radiation are asymmetrical as well, which is only seen in this antenna. The A and C antennas have a symmetric SFF seen from both x and y planes.

Antenna C presents the highest SFF in the front and back directions. A difference of 10% is found between simulations and measurements at the sides ($\phi = \pm 90°$). The reason of this behavior is not very clear, as the simulated transfer function at $\phi = 90°$ (plotted in Fig. 4.17(c)) does not differ much from measurements. On the other hand, the simulated time domain signal at this point (Fig. 4.18(c)) is wider than the measured one. The time resolution to obtain the $IFFT$ of the pulse is limited. Limited resolution added to phase inaccuracy of the simulator leads, in this case, to miss an important point of the time domain signal (a ripple is missed and the pulse seems to be wider). The same occurs in other cases, but the position of the point is not very crucial (is not inside the main pulse) and the SFF is not affected considerably.

4.5.6. Vivaldi-Monopole Systems

In this subsection the SFF of three antenna systems, each composed of a transmitting Vivaldi antenna and a receiving monopole, will be calculated and discussed. The antenna system setup is depicted in Fig. 4.20.

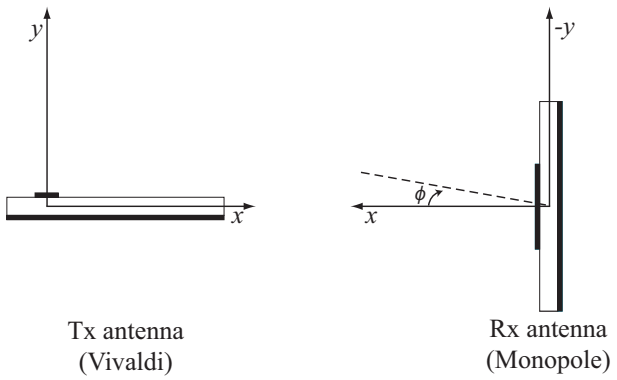

Figure 4.20.: Upper view of Vivaldi-Monopole system setup.

4.5.6.1. Transfer Function

The Vivaldi antenna has an almost constant gain at bore-sight over the whole frequency band. At frequencies above 6GHz, its gain is slightly higher than at lower frequencies. On the other hand, the three monopoles have lower gains at high frequencies. Therefore, using the Vivaldi antenna as a transmitter will improve the performance of the system, if the same monopole is used as a receiver. This is first seen when calculating the system transfer functions (Fig. 4.21). The magnitude $|H(\omega)|$ is higher than that of the monopole-monopole systems and is almost

constant over the whole band. The dips found in Fig. 4.17 are only slightly appreciated, and $|H(\omega)|$ looks almost constant for some angles. Phase nonlinearities are still present, but their position in frequency and intensity are different.

4.5.6.2. Time Signal

Comparing the receiving signals of the Vivaldi-monopole systems with those of the monopole-monopole systems by looking at the results in Fig. 4.22 and Fig. 4.18 only is not evident. The received pulses in Fig. 4.22 are slightly delayed and narrower than those in Fig. 4.18, but again the simulated signals overlap perfectly with the measured ones.

4.5.6.3. System Fidelity Factor

The high directivity and constant gain of the Vivaldi antenna are indices of a non dispersive UWB transmission. The Vivaldi antenna working as the Tx antenna helps to normalize the SFF. As the Tx antenna is the same for all the systems, the performance of the monopoles working as Rx antenna can be compared. This is not the case for the monopole-monopole system situation, where the transmission characteristics of each monopole are as well considered.

The SFF plot of Monopole A (Fig. 4.23(a)) is clearly improved in all directions. An increase of 20% on the sides and 10% on the front and back directions is achieved. This shows that the antenna has a better UWB performance on the $\phi = \pm 90°$ than at $\phi = \pm 180°$.

Monopole B has again a non-symmetric pattern seen from both x and y planes. The increase on the SFF is about 10% in every direction, reaching values of 0.9 at several points. The improvement on the SFF plot is high but still less than the one achieved by Monopole A.

The improvement on Monopole C SFF is not as important as for the other two monopoles but it is the only having a real omnidirectional behavior. The SFF is higher than 0.8 in all directions, but does not reach the 0.9 value that is achieved by Monopoles A and B. The agreement between measurements and simulations is very good.

Monopoles A and B have a large ground plane and a non omnidirectional SFF. Monopole C, on the other hand, has a small ground plane and omnidirectional SFF which is lower than the other monopoles. It can be concluded that monopole C has the best transmission characteristics at $\phi = 0°$, whereas the other monopoles have their best transmitting performance at other angles.

If the antennas are used in a mobile network system, the monopole-monopole case should be studied. Using Monopole C will assure a good transmission of the UWB pulse in every direction, while Monopole A might have bad performance at some directions. Monopole B could be interesting to use when asymmetries of the radio or the environment are present. If the radios are to be connected to a base station, the abnormalities of radiation of the mobile

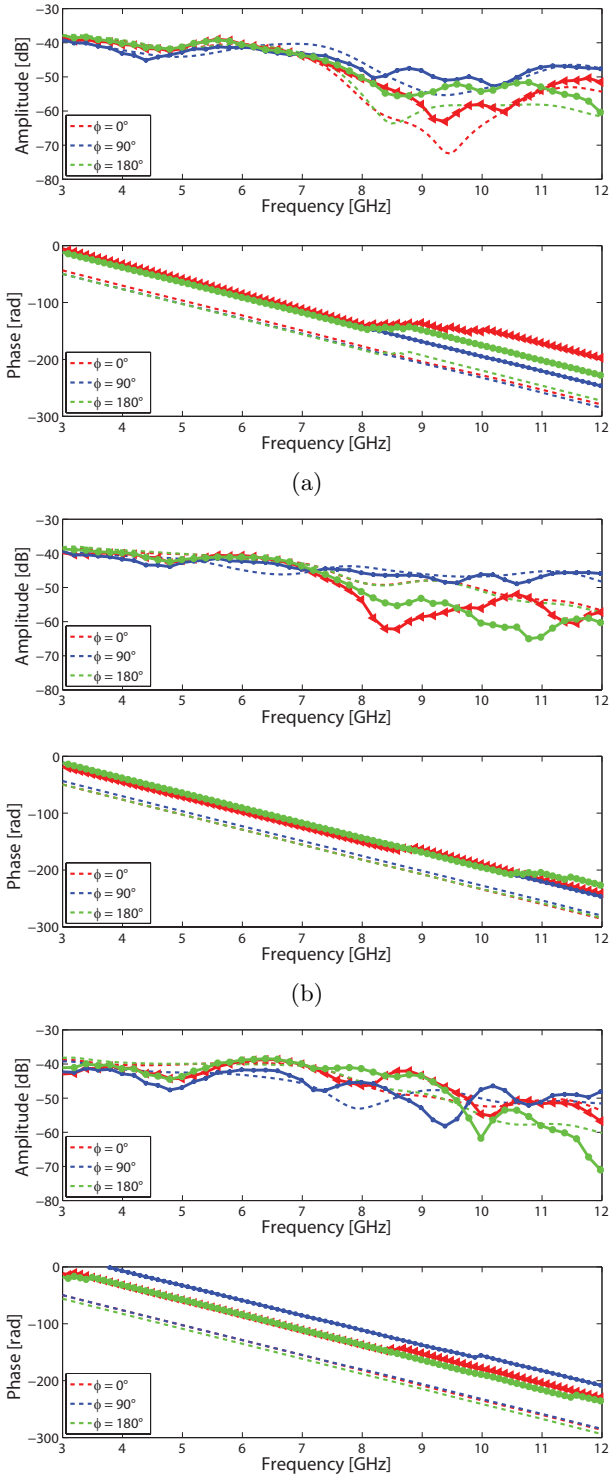

(a)

(b)

(c)

Figure 4.21.: Simulated (dashed lines) and measured (solid lines) transfer function at $\phi = 0°, 90°$ and $180°$, $\theta = 90°$: (a) Vivaldi-Monopole A, (b) Vivaldi-Monopole B, (c) Vivaldi-Monopole C.

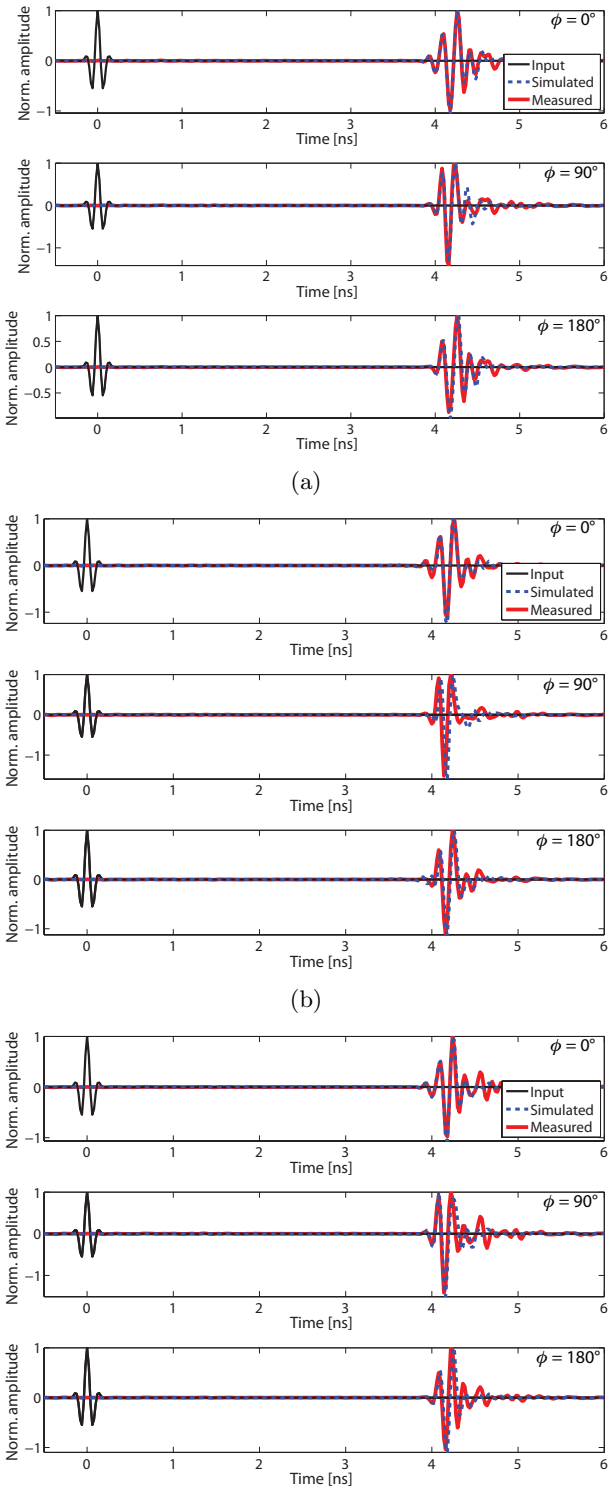

Figure 4.22.: Tx signal and Rx signal (simulated and measured). (a) Vivaldi-Monopole A, (b) Vivaldi-Monopole B, (c) Vivaldi-Monopole C.

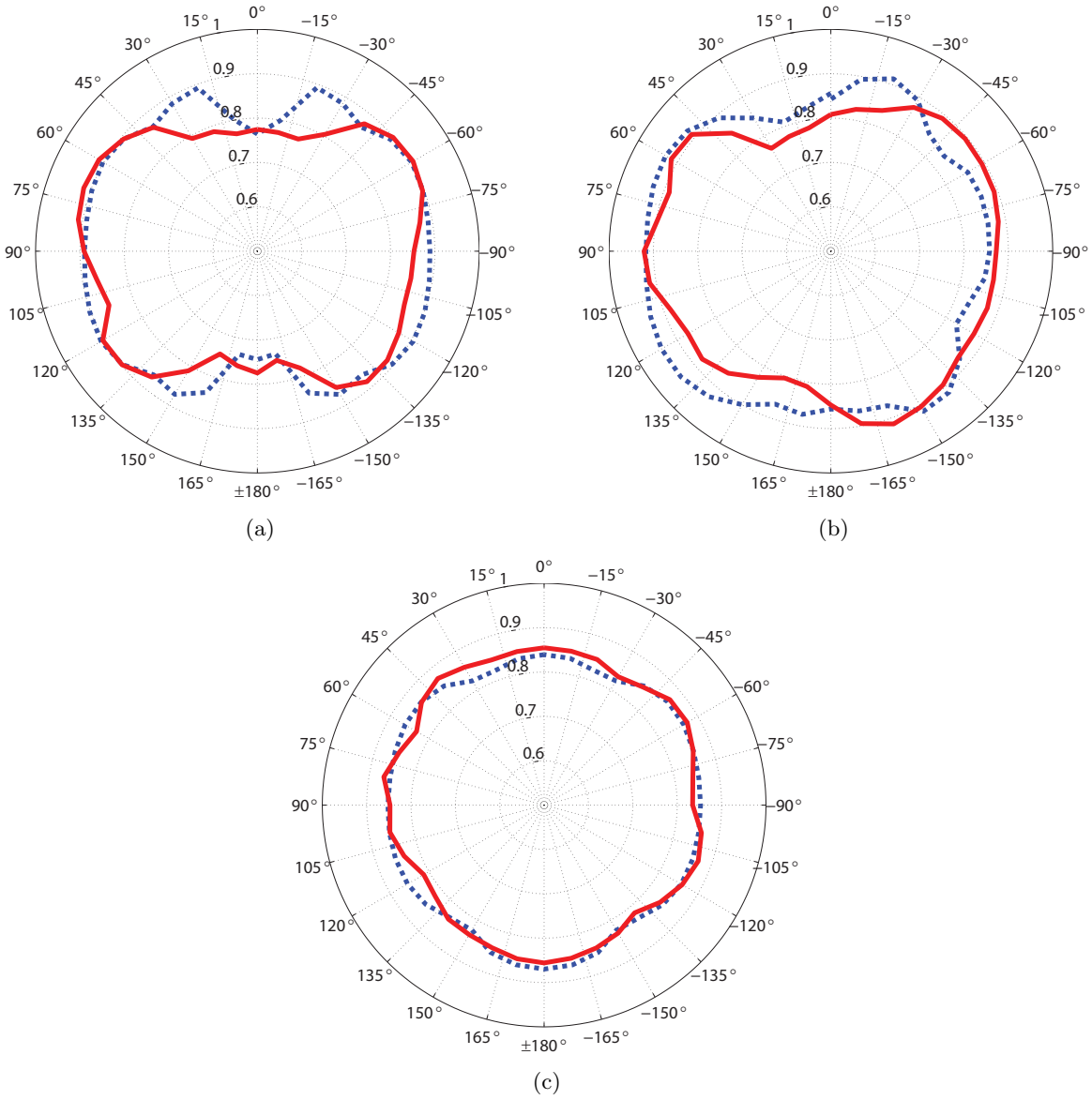

(a) (b)

(c)

Figure 4.23.: Vivaldi-Monopole System Fidelity Factor in function of angle ϕ ($\theta = 90°$): Simulated (dashed lines) and measured (solid lines). (a) Vivaldi-Monopole A, (b) Vivaldi-Monopole B, (c) Vivaldi-Monopole C.

antenna could be canceled if a good directive antenna is used at the base station, like in the Vivaldi-monopole case. Optimal pairing could be found by analyzing the SFF of the two antennas.

4.6. Conclusion

In this chapter the System Fidelity Factor was described and later applied to various antenna systems. The main purpose of the SFF is to incorporate frequency and time domain characteristics of an antenna system into a comparison method for UWB antennas. The SFF is an interesting tool because both simulations and measurements can be done in a simple and straight forward manner. Simulations of a single antenna are combined into a two antenna system analysis by means of a simple post-processing.

To calculate the SFF, the transfer function of the antenna system has to be obtained and from it the received pulse in the time domain. The transfer function was described in the time domain (impulse response) and in the frequency domain. The Friss transmission equation approach was chosen because because of the following reasons: 1) familiarity of antenna designers with frequency domain techniques, 2) simple and direct calculation of the required antenna parameters from simulations, and 3) flexibility to decompose the transfer function in three (H_{Tx}, H_{Rx} and H_{CH}) having with this one degree of freedom more than with the effective height approach. This allows the combination of any two antennas and channel. The free-space channel that is used for typical antenna characterization, can be replaced with any other channel, as it is independent of the antennas.

The simulation and measurement methods to calculate it were presented. The simulation method converts the frequency data of one antenna into the transfer function of a two-antennas system. The received signal in the time domain is obtained after post processing of the input signal and the transfer function. The SFF is finally calculated from the cross-correlation between the two pulses.

Using the System Fidelity Factor, a fair and systematic comparison of UWB antennas can be done in a complete and low time consuming manner, taking in consideration both frequency and time domain radiation characteristics of the antennas. The SFF was calculated for two cases: 1) antenna systems composed of two identical monopoles, 2) antenna systems with a vivaldi antenna at transmission and a monopole at reception. A good agreement between simulations and measurements was achieved in both cases.

References

[1] D. Lamensdorf and L. Susman, "Baseband-pulse-antenna techniques," *IEEE Antennas Propag. Mag.*, vol. 36, no. 1, pp. 20–30, Feb. 1994.

[2] Q. Wu, R. Jin, J. Geng, and M. Ding, "Pulse preserving capabilities of printed circular disk monopole antennas with different grounds for the specified input signal forms," *IEEE Trans. Antennas Propag.*, vol. 55, no. 10, pp. 2866–2873, Oct. 2007.

[3] A. V. Oppenheim and A. S. W. with Ian T. Young, *Signals and Systems*, A. V. Oppenheim, Ed. Prentice-Hall, 1983.

[4] A. Shlivinski, E. Heyman, and R. Kastner, "Antenna characterization in the time domain," *IEEE Trans. Antennas Propag.*, vol. 45, no. 7, pp. 1140–1149, Jul. 1997.

[5] D. M. Pozar, "Closed-form approximations for link loss in a UWB radio system using small antennas," *IEEE Trans. Antennas Propag.*, vol. 51, no. 9, pp. 2346–2352, Sep. 2003.

[6] C. A. Balanis, *Antenna Theory. Analysis and Design.*, Third ed. Wiley-Interscience, 2005.

[7] D. M. Pozar, *Microwave and RF Design of Wireless Systems.* John Wiley and Sons, Inc., 2001.

[8] D. M. Kerns, *Plane-Wave Scattering-Matrix Theory of Antennas and Antenna-Antenna Interactions*, National Bureau of Standards Std., June 1981.

[9] M. Kanda, "Transients in a resistively loaded linear antenna compared with those in a conical antenna and a TEM horn," *IEEE Trans. Antennas Propag.*, vol. 28, no. 1, pp. 132–136, Jan. 1980.

[10] X. Qing, Z. N. Chen, and M. Y. W. Chia, "Network approach to UWB antenna transfer functions characterization," in *Proc. European Conference on Wireless Technology*, Oct. 3–4, 2005, pp. 293–296.

[11] Z.-A. Zheng and Q.-X. Chu, "A simplified modeling of ultrawideband antenna time-domain analysis," in *Proc. IEEE International Conference on Ultra-Wideband ICUWB 2009*, Sep. 9–11, 2009, pp. 748–752.

[12] Spectrum Elektrotechnik GmbH. [Online]. Available: http://www.spectrum-et.org

[13] HUBER+SUHNER. [Online]. Available: http://www.hubersuhner.ch

[14] W. C. Lee, *Mobile Communications Engineering. Theory and Applications*, 2nd ed. Mc Graw-Hill Telecommunications, 1998.

[15] The MathWorks, MATLAB 7.1.

[16] D.-H. Kwon, "Effect of antenna gain and group delay variations on pulse-preserving capabilities of ultrawideband antennas," *IEEE Trans. Antennas Propag.*, vol. 54, no. 8, pp. 2208–2215, Aug. 2006.

[17] H. Schantz, *The Art and Science of Ultrawideband Antennas.* Artech House, 2005.

[18] H. J. Visser, "Low-cost, compact UWB antenna with frequency band-notch function," in *Proc. Second European Conference on Antennas and Propagation EuCAP 2007*, Nov. 11–16, 2007, pp. 1–6.

[19] N.-W. Chen and Y.-C. Liang, "Coplanar-waveguide fed circular disc monopole antenna with improved radiation characteristics," in *Proc. Second European Conference on Antennas and Propagation EuCAP 2007*, Nov. 11–16, 2007, pp. 1–6.

[20] J. G. Qi Wu, Ronghong Jin, "A single-layer ultrawideband microstrip antenna," *Antennas and Propagation, IEEE Transactions on*, vol. 58, no. 1, pp. 211 –214, Jan. 2010.

[21] F. Merli, J.-F. Zurcher, A. Freni, and A. Skrivervik, "Analysis, design and realization of a novel directive ultrawideband antenna," *Antennas and Propagation, IEEE Transactions on*, vol. 57, no. 11, pp. 3458 –3466, Nov. 2009.

[22] P. Gibson, "The vivaldi aerial," in *Microwave Conference, 1979. 9th European*, 17-20 1979, pp. 101 –105.

[23] A. Hood, T. Karacolak, and E. Topsakal, "A small antipodal vivaldi antenna for ultrawide-band applications," *Antennas and Wireless Propagation Letters, IEEE*, vol. 7, pp. 656 –660, 2008.

[24] P. Cerny, J. Nevrly, and M. Mazanek, "Optimization of tapered slot vivaldi antenna for uwb application," in *Applied Electromagnetics and Communications, 2007. ICECom 2007. 19th International Conference on*, 24-26 2007, pp. 1 –4.

[25] A. Elsherbini and K. Sarabandi, "Directive coupled sectorial loops antenna for ultrawideband applications," *Antennas and Wireless Propagation Letters, IEEE*, vol. 8, pp. 576 –579, 2009.

[26] J. Liang, L. Guo, C. C. Chiau, and X. Chen, "Time domain characteristics of UWB disc monopole antennas," in *Proc. European Conference on Wireless Technology*, Oct. 3–4, 2005, pp. 289–292.

[27] G. Q. D. de Leon and A. K. Skrivervik, "Analysis of UWB antennas for carrier-based UWB impulse radio," in *Proc. Second European Conference on Antennas and Propagation EuCAP 2007*, Nov. 11–16, 2007, pp. 1–5.

[28] W. Sorgel, C. Waldschmidt, and W. Wiesbeck, "Transient responses of a vivaldi antenna and a logarithmic periodic dipole array for ultra wideband communication," in *Antennas and Propagation Society International Symposium, 2003. IEEE*, vol. 3, 22-27 2003, pp. 592 – 595 vol.3.

5. Novel Antenna Designs

5.1. Introduction

This chapter exposes the contributions done in UWB antenna design. All the designs were done in planar substrates using both symmetric and asymmetric feeding lines. The characterization methods described in Chapter 3 and Chapter 4 are used to analyze their performance. The antennas have omnidirectional radiation as they are meant for mobile communications and this type of antenna is best for this application.

The first antenna is a monopole consisting of a tapered radiator and a tapered ground plane. Two different feeding lines were used: microstrip line and coplanar waveguide, in order to get a better insight into their effects on the radiation of an UWB pulse. The design was implemented to analyze the increase of substrate permittivity (ϵ_r) as a miniaturization technique for UWB antennas. Three substrates with different ϵ_r are used to implement the monopoles. A total of 6 antennas were simulated and measured. Conclusions were derived about the ground effect and the impact of the feeding lines on antenna radiation performance.

The second antenna consists of an elliptical dipole fed by coplanar strip lines. The design is of special interest because of its peculiar feeding system. A method to calculate the antenna impedance is proposed. An UWB balun, designed specially for this application is introduced, and compared to literature. The antenna transfer function is then calculated after de-embedding the measurements of the antenna with balun and compared with the simulated values of the antenna without balun. The de-embedding method is shown to be accurate, as simulations agreed with measurements.

As seen in Chapter 2, the European UWB mask diverges largely from the one established by the FCC. Therefore different antenna models should be implemented in order to match the ECC restrictions. The last antenna presented in this chapter was designed for a specific application developed for the European market, working in the ECC band (6−8.5 GHz). It consists of a dipole with a short-circuit line connecting both arms. The dipole arms are formed by half circle-half ellipse elements which are by nature broadband elements. The short-circuit then reduces the bandwidth of operation to achieve less than the 2.5 GHz bandwidth of the ECC mask. The total area is less than 20 $\times$ 10 mm, which folded can fit in a 1 cm^3 cube. Simulations and measurements of the flat and folded dipoles are shown, together with the microstrip-to-paired strips balun needed for the measurements.

Some important tips and advices that make an efficient UWB design were derived from the designs, and are explained in the end of the chapter. This will help the reader to understand what should and should not be done when designing an UWB antenna. A summary will be given at the end of the chapter.

5.2. Tapered monopole with small ground

UWB communication systems require small antennas to be placed into low power devices. The omnidirectional radiation of a monopole antenna makes it optimal for mobile applications. Moreover planar monopoles are of special interest because of their reduced size and low complexity. UWB monopole antennas have been studied and many designs have been implemented in the last years [1],[2],[3], however size is still a big issue for the increasing demand of miniaturized systems.

The most evident technique to miniaturize an antenna is to increase the permittivity of the substrate. However this only applies to narrowband antennas. For UWB antennas, this is not a trivial solution, since the frequency is inversely proportional to the square root of the substrate permittivity [4].

To analyze the effect of different permittivity values in the antenna performance, commonly used substrates with different permittivities were chosen. The characteristics of these substrates is given in Table 5.1.

Table 5.1.: Substrates Characteristics

Substrate	ϵ_r	**tanδ**	**h [mm]**
FR4	4.4	0.02	0.8
Duroid6006	6.15	0.0019	0.635
Duroid6010	10.2	0.0024	0.635

5.2.1. Antenna description

Fig. 5.1 shows the two different monopole architectures that have been studied. On the left side (Fig. 5.1(a)) the monopole is fed by a coplanar waveguide and by a conventional microstrip line on the right side (Fig. 5.1(b)). In order to achieve a better matching over the UWB band, both the ground plane and the monopole radiators have a tapered shape. The substrate surrounding the antennas, of about 1 mm, is used to improve the matching.

The CPW-fed monopole was designed for the three different substrates mentioned above, the same was done for the microstrip-fed antenna. In total six antennas were fabricated, simulated and measured. The maximum size of the antennas' substrate is 23 $\times$ 25 mm. As each substrate has different characteristics, small changes in the antennas were done to obtain the desired return loss at the input of the SMA connector. The main difference between the antennas lays in the width of the transmission line. The values of **d** and **ws** used for each antenna is shown in Table 5.2.

The length of the antenna **L** was set to 25 mm. This was the smallest value that could give a good matching on all the antennas over all the UWB band. The simulated (dashed line) and measured (continuous line) return loss of the CPW-fed antennas in Fig. 5.2(a) and the microstrip-fed antennas is shown in Fig. 5.2(b).

The antennas with the highest permittivity substrate (RT6010) do not have a reflection

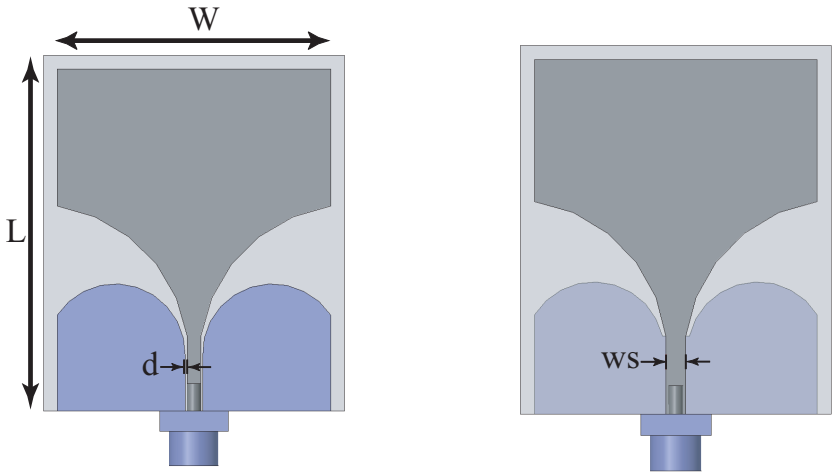

Figure 5.1.: Tapered monopoles: (a) Coplanar waveguide fed, (b) Microstrip line fed.

Table 5.2.: Feeding Lines

	Microstrip	**CPW**	
Substrate	**ws [mm]**	**ws [mm]**	**d [mm]**
FR4	1.4	1.1	0.14
Duroid6006	1	1.1	0.2
Duroid6010	0.6	1.2	0.4

coefficient under the specified requirements (−10 dB) over all the UWB band. They were more difficult to match than the other antennas. The return loss is very sensitive to small changes in width **ws** and gap **d** (in the CPW antennas). Therefore the high S11 level of the measured antennas can be due to under etching produced during fabrication.

5.2.2. Radiation Pattern

An important characteristic of UWB antennas is the constant gain over all the band. This characteristic could be harder to obtain in an omnidirectional antenna, as the gain should be constant at every angle of radiation. As known from [5], antenna gain is proportional to directivity, and directivity is proportional to the antenna effective area (A_e). This can be applied only in narrow band antennas, as the effective area is given in wavelengths and therefore is proportional to frequency. The A_e of an UWB antenna at the highest frequency (10.6 GHz) is more than 3 times the A_e at the lowest limit (3.1 GHz). Therefore the antenna gain cannot be the same over the UWB band when using conventional design methods.

The studied antennas are etched on different permittivity substrates, therefore the A_e will not be the same for all antennas. The monopoles will have several resonances in the UWB frequency band. The number of resonances ($\lambda_{eff}/2$) in the FR4 antennas will be lower

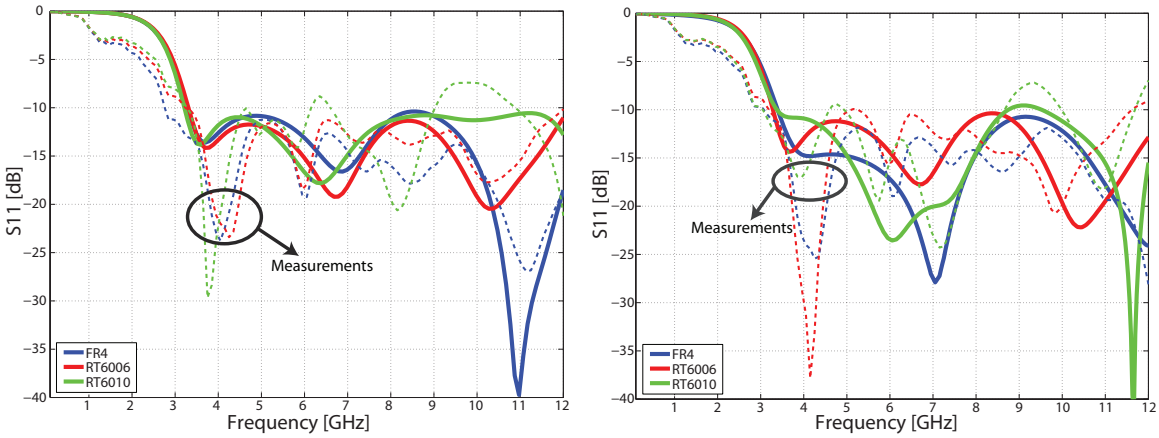

Figure 5.2.: Simulated and Measured reflection coefficient: (a) CPW-fed antennas, (b) Microstrip-fed antennas.

than the resonances found in a RT6010 antenna. At every resonance the surface currents in the antenna will be different, therefore changes in the radiation pattern are expected as frequency increases. To better understand these changes, radiation patterns on the azimuthal plane of the six antennas were measured. Measurements were done in an anechoic chamber at five frequencies equally spaced inside the UWB band. The radiation patterns are shown in Fig. 5.3.

At the lowest frequency, all the antennas have an omnidirectional radiation. As expected, the pattern changes with increasing frequency. The RT6010 monopoles has a considerable different radiation at 10.6 GHz. At this frequency the monopole radiates more to the sides, or $\phi = \pm 90°$, and the gain is not much lower than at 3.1 GHz. At the middle frequencies (8.725, 6.85 and 4.975 GHz) the gain (at $\phi = \pm 90°$) is considerably lower. These gain inequalities will be traduced in a time domain distortion of the radiated pulse in this direction.

The CPW-fed monopoles show as well an interesting change in radiation intensity at $\phi = \pm 180°$. The microstrip-fed antennas radiation in this direction (back direction) is almost constant over all the band, assuming by constant a change no larger than 2 dB. The RT6010 CPW antenna has a decrease of almost 5 dB at 10.6 GHz. This again is expected to produce a distortion in the radiated pulse.

5.2.3. Fidelity Factor

The fidelity factor (FF) of an antenna can be calculated following the procedure described in [6]. This gives a comparison based on a cross-correlation between the radiated E-field and the input or transmitted pulse. The FF was calculated for each antenna and plotted in Fig. 5.4. The FR4 and RT6006 antennas have a similar FF in all directions. The RT6010 monopole has a considerable decrement in the FF between $\phi = \pm 60°$ and $\phi = \pm 120°$. As seen in Fig. 5.3,

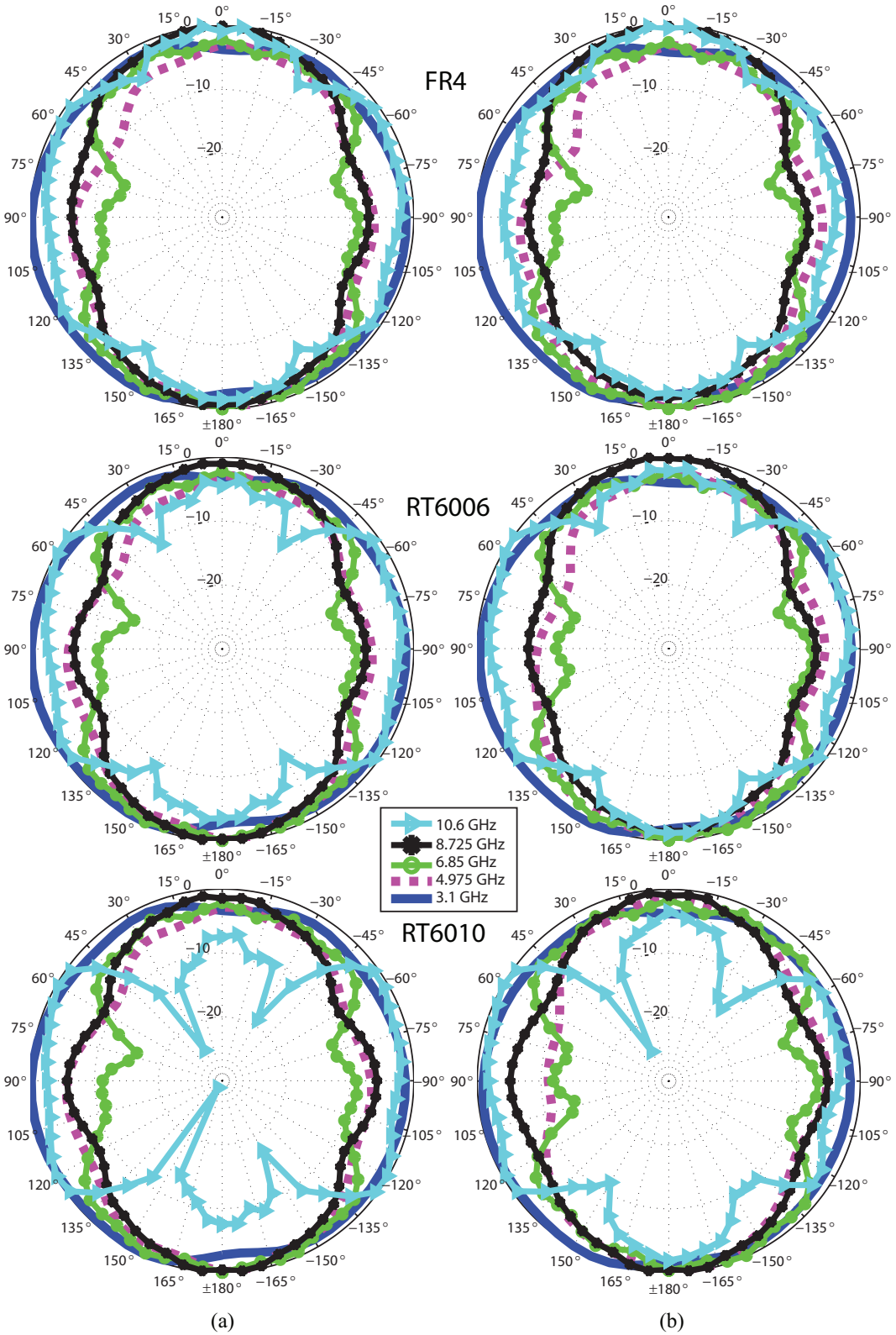

Figure 5.3.: Radiation Pattern. a) CPW-fed antennas, b) Microstrip-fed antennas

the RT6010 antenna has a strongest change in radiation at this angle. The FF for all the antennas is higher than 0.9 in the azimuth plane, which indicates a good correlation between the radiated E-field and the input signal at the antenna port.

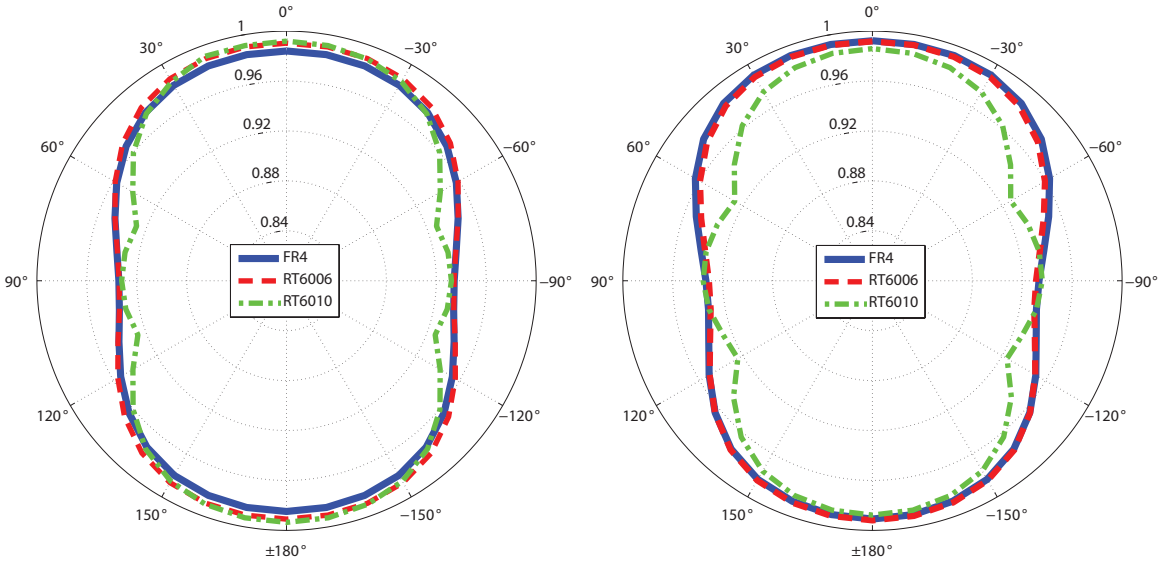

Figure 5.4.: Fidelity Factor: a) CPW-fed antennas, b) Microstrip-fed antennas.

5.2.4. System Fidelity Factor

The simulated SFF in Fig. 5.5 is lowest in the side direction ($\phi = 90°$) for all the antennas. As expected, the FF alone is higher than the SFF, where the distortion produced by both antennas and the transmission channel are taken in consideration.

It has been shown in the previous section that high permittivity antennas change their radiation orientation at high frequencies. This radiation characteristic will affect the SFF result. The SFF considers all the frequency band at once, as opposed to the radiation pattern. Therefore the optimum SFF is obtained when the radiation is constant over all the frequency band of interest. It is also important to notice that only one antenna system combination was studied, having the Tx antenna radiating at bore-sight. The SFF plot will change when changing the direction of the Tx antenna. Therefore some combinations could present its highest SFF values at other angles. For example, it is interesting to consider the SFF when the Tx antenna is oriented at $\phi = \pm 90°$. From simulations, it can be seen that the worst SFF will be found in this case.

Measurements of the SFF were realized using the method proposed in Chapter 4. The results were not as expected, diverging largely from simulations. Several factors may have influenced these results. The first one is, as for most small antennas, the currents induced in the cable. This induced current depends mostly on the antenna configuration, and are

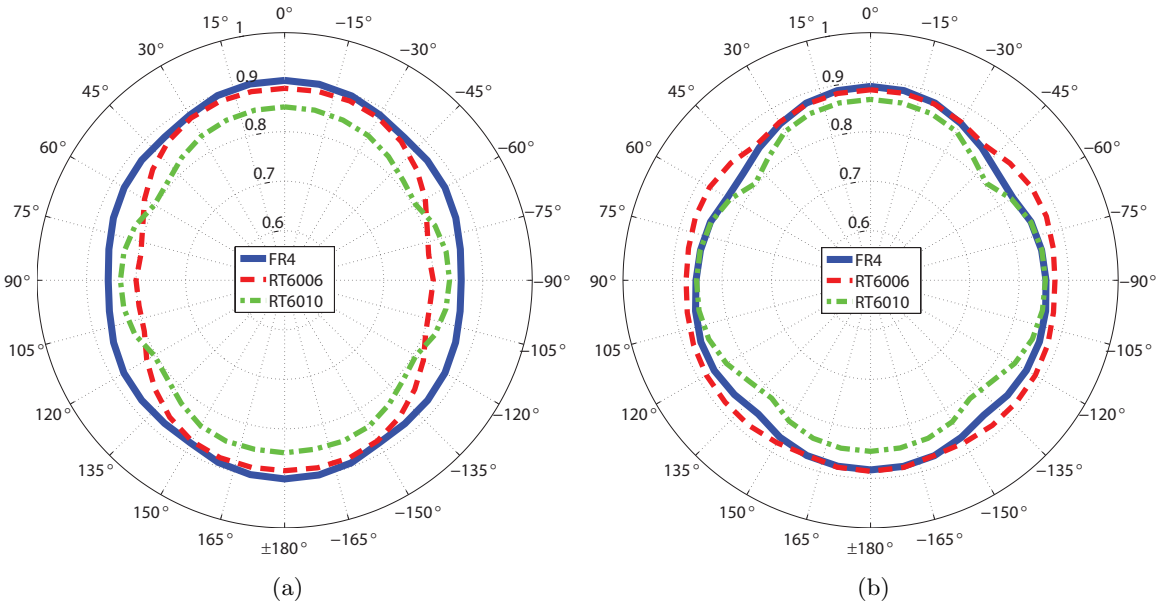

Figure 5.5.: Simulated System Fidelity Factor: a) CPW-fed antennas, b) Microstrip-fed antennas.

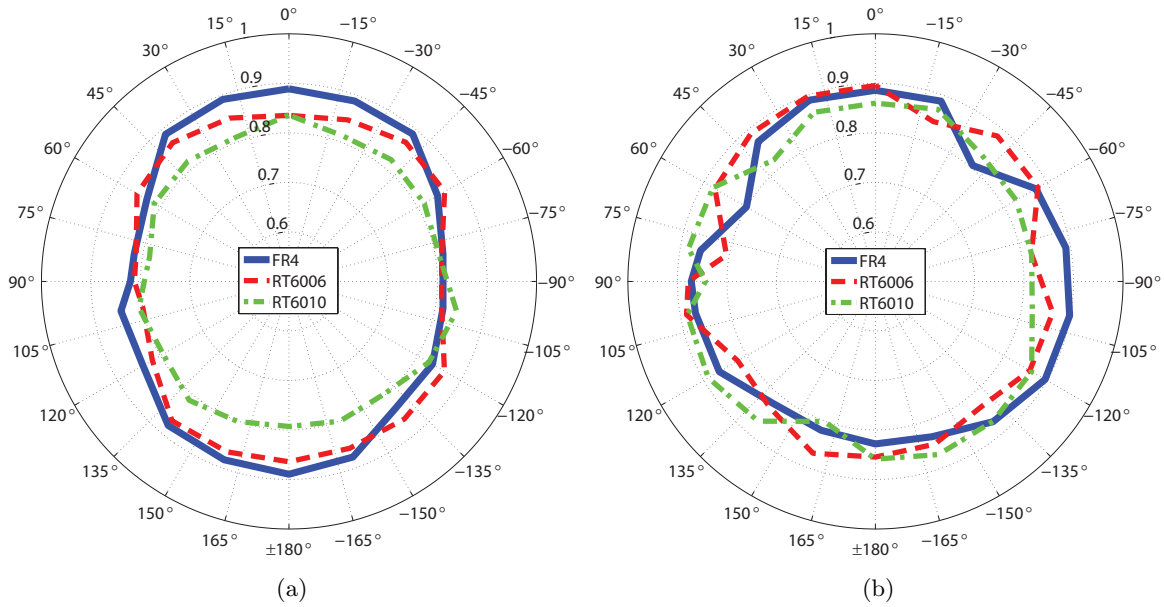

Figure 5.6.: Measured System Fidelity Factor: (a) CPW-fed antennas, (b) Microstrip-fed antennas.

more common in antennas fed by an unbalanced line having a small ground plane [7],[8]. The tapered monopoles have a ground plane that is smaller than the radiator. Hence the magnitude of the currents on the border of the ground plane (close to the cable) is high, increasing the probability of having induced currents in the cable. This might also explain the differences between simulations and measurements found in the reflection coefficient in Fig. 5.2.

The SFF of the CPW-fed antenna (Fig. 5.6(a)) has a similar shape to simulations. The SFF is lower at the sides ($\phi = \pm 90°$) and higher at ($\phi = 0°, 180°$). The measurement results of the RT6010 antenna show an SFF of 0.8 in every direction, which is 10% less than the simulated value. This antenna was expected (from simulations) to have the highest SFF in the front and back radiation, but in the measurements this is not the case.

The measured SFF of the microstrip-fed antennas (Fig. 5.6(b)) resemble less to the simulated SFF values. The plots are not symmetric and strange "ripples" were found at different angles.

From these results, we can arrive at a conclusion considering the ground plane configurations of UWB antennas. First of all, its size is crucial for doing correct measurements. It has to be large enough in order to avoid induced currents in the measuring cable, or special equipment (chokes, absorbers) needs to be used. The second important conclusion is the difference between CPW and microstrip-fed antennas. It has been shown that for microstrip-fed antennas the SFF are less symmetric than for CPW-fed antennas. This is somehow obvious, as the CPW line is symmetric in every direction, where as the microstrip line not. The effect of the ground on the pulse dispersion is higher for microstrip antennas.

5.3. Dipoles

Dipole antennas are of interest to system designers for two main reasons: 1) their differential (or balanced) input, and 2) the avoiding of ground plane. Digital systems are taking advantage of differential antenna connections due to their simplicity to match to the the system components (amplifiers, op-amps, etc.). Information from balanced lines is doubled, as each line contains the signal with a 180°phase shift, which can be directly used for BPSK modulation. The elimination of the ground plane reduces the total size of the system in most of the cases. Spurious currents coming from the ground plane are very disturbing for the system circuits; a well designed dipole will not have any common mode currents therefore will not affect other components.

These are some of the reasons why two different UWB dipoles were designed and are shown in the following sections. The first dipole was designed for transmitting signals in the FCC band (3.1 – 10.6 GHz) and the second dipole was designed for the European ECC band (6 – 8.5 GHz).

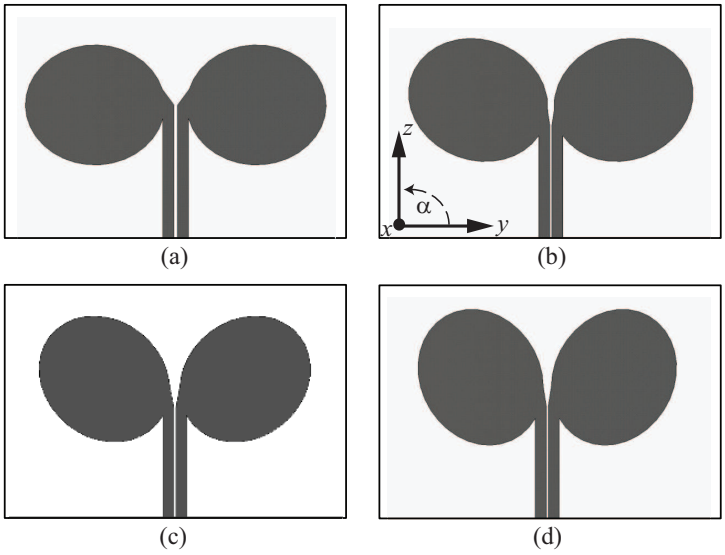

Figure 5.7.: Planar elliptical dipoles with different rotation angle α. a)$\alpha = 0°$, b)$\alpha = 20°$, c)$\alpha = 40°$and d)$\alpha = 60°$.

5.3.1. Planar elliptical dipole

Differential antennas are becoming of great interest for UWB systems because of the simplicity to connect them to an input amplifier. This type of antenna can be connected directly to the system without using an external balun, or balanced to unbalanced transition, thus reducing size and complexity of the UWB system [9]. Most of differential antennas reported in literature are fed with coaxial cables perpendicular to the antenna plane [10], [11]. This could be of use for some applications, but it may be a problem for systems with strong space limitations.

Planar Elliptical Differential (PED) UWB antennas fed by coplanar striplines (Appendix B)were studied. The chosen feeding line allows the antenna to be in the same plane as the circuit board, reducing the size of the system, and facilitating the connection to the input amplifier or LNA. However radiation towards the system will occur as it is in the radiation axis of the dipole.

The original dipole has its ellipses perpendicular to the feed lines (Fig.5.7(a)), its radiation is expected to be omnidirectional in the X-Z plane. A possible method to enhance radiation outwards the radio system is to rotate the dipole ellipses. Three antennas having this rotation for angles α of 20°, 40° and 60°, were studied and are shown in Fig. 5.7(b), (c) and (d) respectively.

The size of the ellipses was found to be the most critical value to obtain a good matching of the antenna. To make a fare comparison of the dipoles, the same ellipses were used. The ellipse size that gave the best matching for all the elements was chosen, it has a semi-major axis of 9.5 mm and a semi-minor axis of 8.075 mm. The total surface of the dielectric used (Rogers RO4003, 0.508 mm thick) is 50 × 34 mm.

The rotation on the ellipses promote a more directive radiation pattern, having its higher

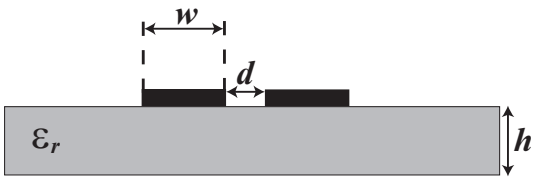

Figure 5.8.: Transveral cut of a CPS line.

radiation in the z direction [6]. A deeper study was done only on one of the antennas, the dipole with $\alpha = 40°$. This dipole showed an optimal compromise between directivity and a good matching. Directivity of the $\alpha = 60°$ is higher, but its return loss was not below -10 dB over all the band. While the $\alpha = 20°$ antenna does not have a considerable increase in directivity.

A coplanar stripline structure is shown in Fig. 5.8. The substrate used is Rogers RO4003 with 0.508 mm thickness and $\epsilon_r = 3.38$. The impedance of the lines was calculated using the equations in Appendix B. An impedance of 107 Ω is obtained setting $\mathbf{d} = 0.25$ mm and $\mathbf{w} = 1.5$ mm.

5.3.1.1. Differential Return Loss

Measurements of a differential antenna cannot be made directly with a conventional Vector Network Analyzer (VNA). A VNA has typically 2 coaxial cables connected at each port. The coaxial cables are unbalanced whereas the antenna to be measured has a balanced input. To obtain the differential return loss of the PED antenna, each line of the CPS line is connected to a port of the VNA. Treating each line as an unbalanced port, a post calculation of the differential return loss is done using the following equation:

$$S_{diff} = 20log\left|\frac{1}{2}(S_{11}^2 + S_{22}^2) - \frac{1}{2}(S_{12}^2 + S_{21}^2)\right| \tag{5.1}$$

The CPS lines cannot be connected directly to the VNA ports. A two-port measurement jig was implemented, as described in [12]. The antenna connected to the jig is shown in Fig. 5.10(a). The measurements obtained at the VNA ports contain as well the information of the jig. In order to eliminate the effect of the jig, a de-embedding has to be done to obtain the return loss at the antenna reference plane.

A schematic representation of the S-matrix of the antenna with the jig is shown in Fig. 5.9. P1 and P2 represent the ports at the jig, which are connected to the VNA. The lower lines represent the ground or outer part of the cable. The impedance of the cables are Z_{C1} and Z_{C2}, while the impedance of the VNA ports are considered to be 50 Ω. γ is the propagation constant and d the total length of the jig lines. Ideally Z_{C1} and Z_{C2} are identical and known, but γ_1 and γ_2 are unknown. The cables were cut with a very fine precision, in order to have $d_1 = d_2$. Only the inner part of the cables were connected to the antenna lines, the CPS line where we want to obtain the port information.

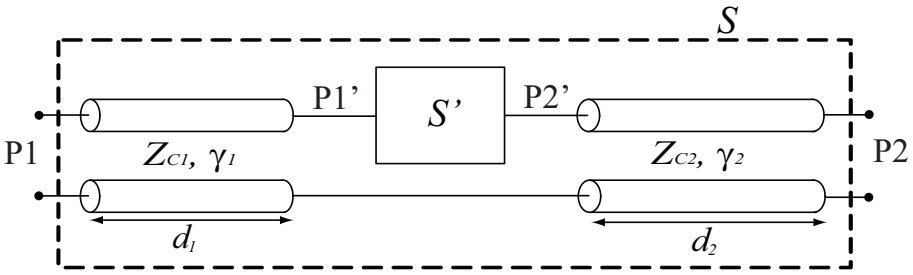

Figure 5.9.: Schematic of the jig.

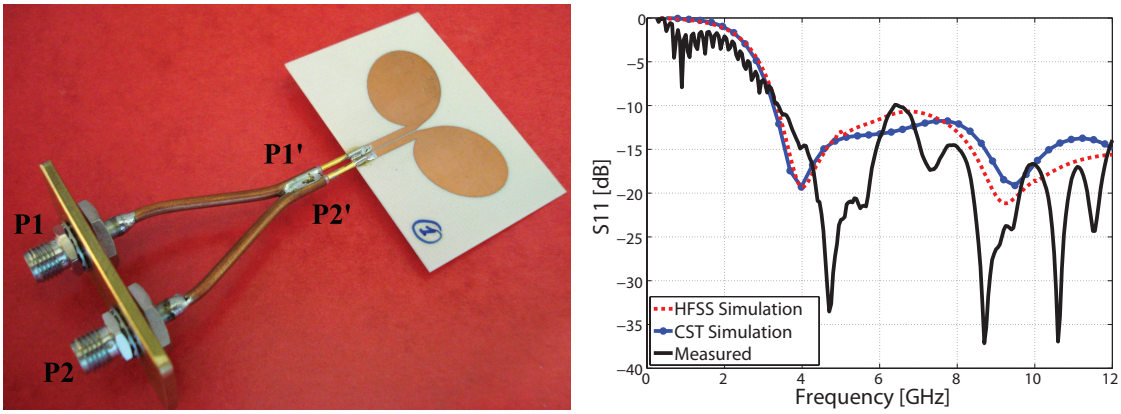

(a) PED Antenna with jig

(b) Measured and simulated S_{11}

Figure 5.10.: Differential Port deembedding.

The scattering matrix of the antenna (S') at ports P1' and P2' can be calculated using the following matrix [13]:

$$S' = \begin{bmatrix} S_{11}e^{2\gamma_1 d_1} & S_{12}e^{(\gamma_1 d_1 + \gamma_2 d_2)} \\ S_{21}e^{(\gamma_2 d_2 + \gamma_1 d_1)} & S_{22}e^{2\gamma_2 d_2} \end{bmatrix} \tag{5.2}$$

The transmission characteristics of the lines (attenuation α and phase β) can be obtained by short-circuiting the two terminals of the jig to the cables' ground. Assuming a perfect short circuit and symmetry of the jig terminals, $S'_{11} = S'_{22} = -1$ (total reflection). Then γ can be obtained from:

$$S_{11} = -e^{-2(\alpha - j\beta)d} = -e^{-2\gamma d} \tag{5.3}$$

$$\gamma d = -\frac{ln(-S_{11})}{2} \tag{5.4}$$

The differential return loss of the antenna is calculated substituting the values of the S'

matrix in equation (5.1). In Fig. 5.10(b) the measured S_{11}, obtained after de-embedding, is plotted together with simulation results from HFSS and CST Microwave Studio. Measurements and simulations are in good agreement. They are below -10 dB in the UWB band. The measured return loss has ripples in the entire band, which is commonly found in S_{11} measurements of UWB antennas. This is due to the small size of the antenna and the standing waves produced by the antenna currents in the cable.

5.3.1.2. UWB Balun: Microstrip-to-CPS line

In order to measure the transmission between two antennas, an external balun was used to correctly feed the dipole using the VNA port. The balun published in [14] was taken as a model, and a first study was done where the design was implemented and measured. The balun consists of a tapered step line which increases the impedance of the microstrip line. This line forms one of the CPS lines when the ground plane ends. The electric field from this first line is coupled to the second line via a radial stub. The radial stub together with the tapered line continuously transform the unbalanced electric field configuration (microstrip line) to a balanced electric field (CPS line).

The implementation of the balun made by Tu and Chang was done using only 3 matching sections in the microstrip transformer. The balun and its dimensions are shown in Fig. 5.11. The measured S-parameters were not as expected. A strange behavior at 7 GHz was found which looked like a resonance. The first guess was that the resonance was coming from the CPS-line and a new balun with longer L_cps was built. This time two resonances appeared, one at 5.5 GHZ and the other at 8.5 GHz. These resonances were not found in simulations and no direct explanation can be given. The S-parameters of both baluns (L_cps = 20 mm and 30 mm) are shown in Fig. 5.12.

A new balun was designed, where the radial stub was replaced by a half circle stub. The tapered line was reduced to obtain a good matching at the ports. The balun was fabricated and measured, obtaining good results that correspond to simulations. Two different L_cps lengths were used and the results were similar. The dimensions and architecture of the balun are shown in Fig. 5.13, and the S-parameters of the novel balun in Fig. 5.14.

5.3.1.3. Balun de-embedding

The transmission coefficient between two PED antennas was measured using the measurements setup described in Section 4.2.5. The antennas were positioned at each side of the foam support, transmitting and receiving in the $+z$ direction. The balun has a large impact in the measured S_{21}, and we are only interested in the effect of the antennas. In order to eliminate the effect of the balun, the S-matrix of the balun (back-to-back) was subtracted from the whole S-parameters measurement of the two antenna system. Fig. 5.15 shows the antenna with balun together with the balun back-to-back.

Fig. 5.16 shows the measured S-parameters of the antenna with balun. They are compared with the simulated values obtained from HFSS.

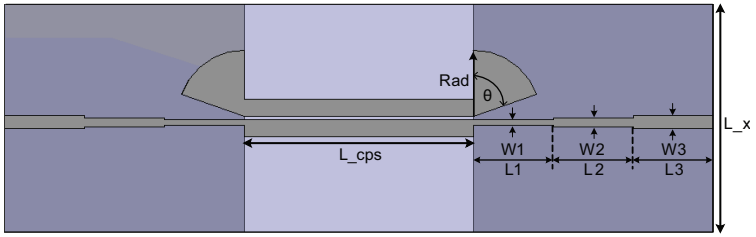

Rad	θ	W1	W2	W3	L1	L2	L3	L_x
5.82 mm	70.5°	0.5 mm	0.8 mm	1.15 mm	7 mm	7 mm	7 mm	20 mm

Figure 5.11.: Tu and Chang balun architecture and dimensions.

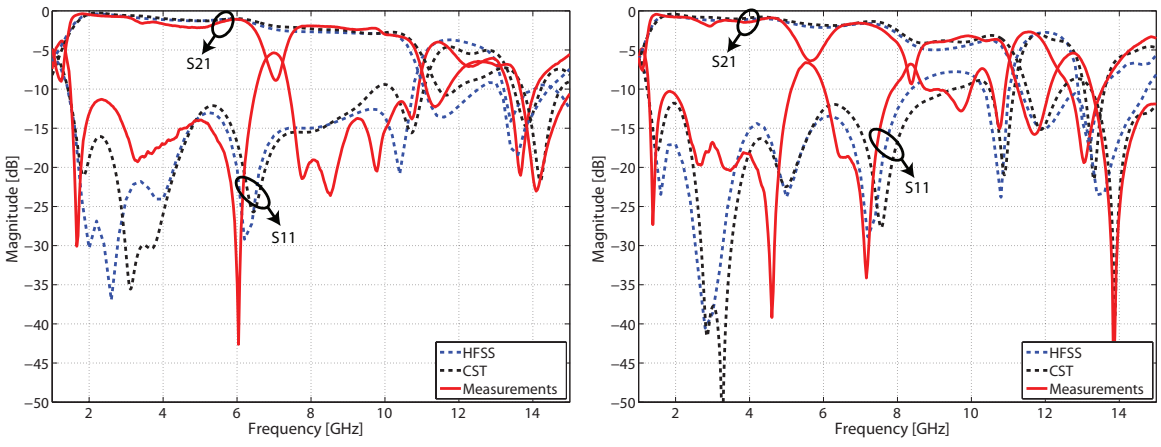

Figure 5.12.: Tu and Chang balun. (a) short CPS-line (20mm), (b) large CPS-line (30mm).

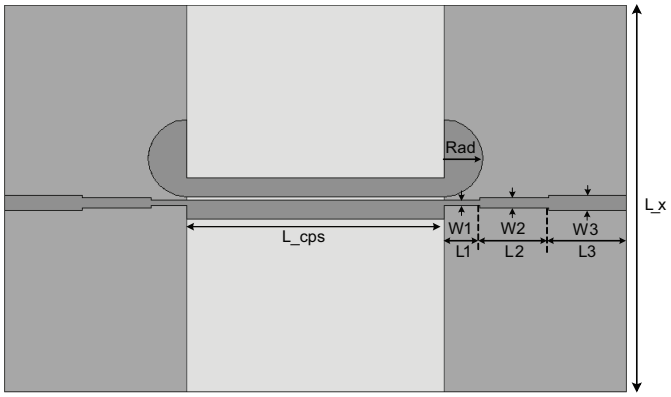

Rad	W1	W2	W3	L1	L2	L3	L_x
3 mm	0.45 mm	0.8 mm	1.15 mm	2.75 mm	5.4 mm	4 mm	30 mm

Figure 5.13.: Half circle balun architecture and dimensions.

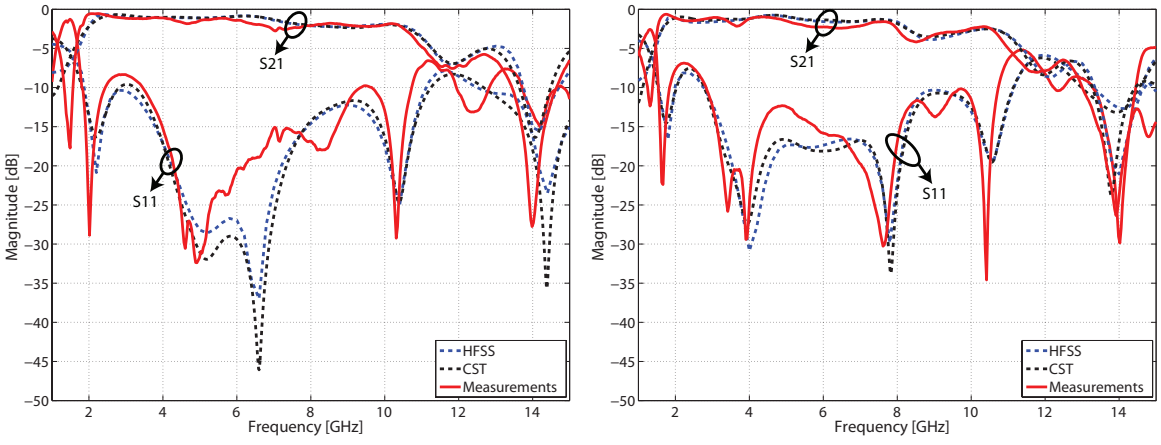

Figure 5.14.: Novel balun. (a) short CPS-line (20mm), (b) large CPS-line (30mm).

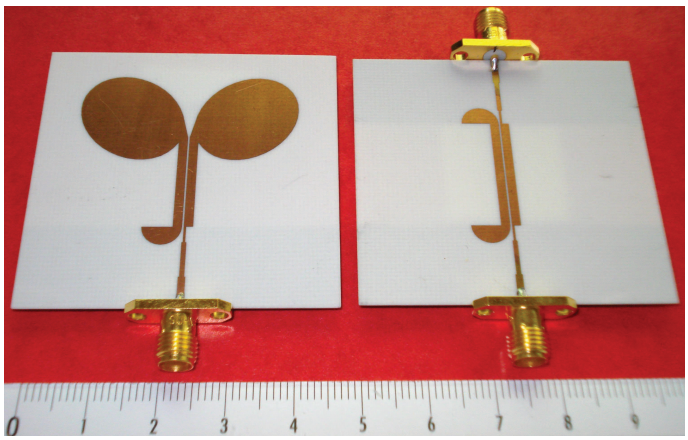

Figure 5.15.: Antenna with balun and balun back-to-back.

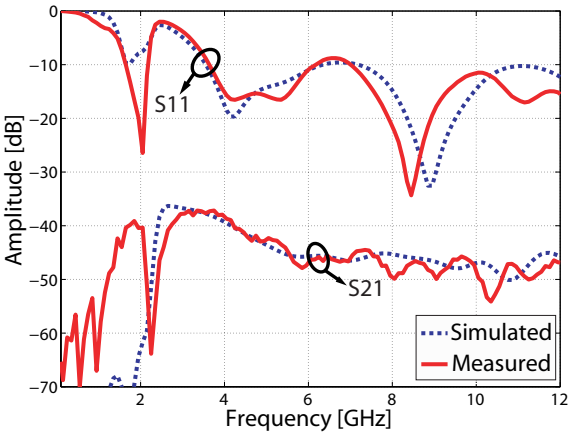

Figure 5.16.: S-parameters of PED antenna system with balun.

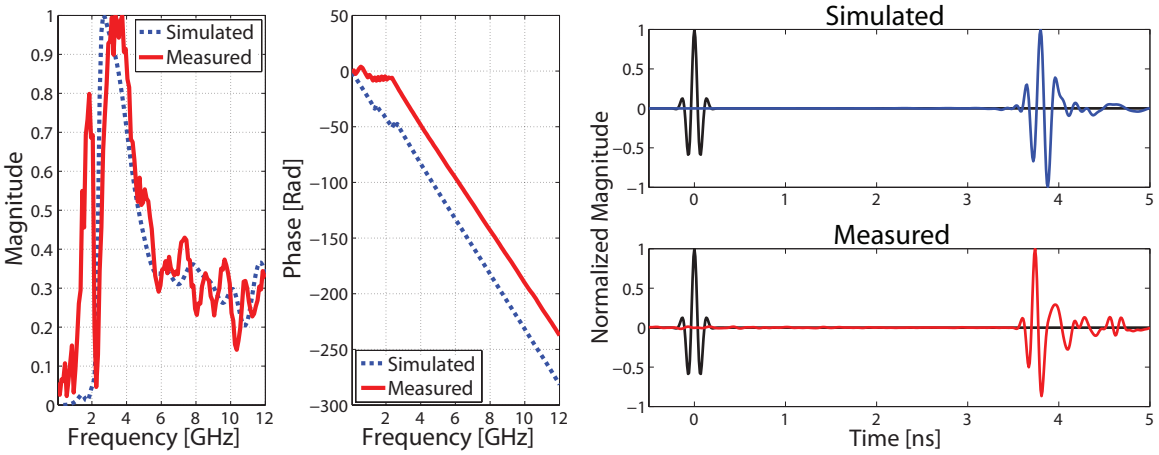

(a) PED antenna with balun Transfer Function, amplitude and phase.

(b) Time domain signal simulated and measured.

Figure 5.17.: Transfer function and received pulse

Fig. 5.17(a) shows the transfer function (S_{21}) of the antenna system in amplitude and phase along with the measured values. The phase shows to be linear in the UWB band. A good agreement between measurements and simulations can be seen. To illustrate this, the signal in time domain is plotted in Fig. 5.17(b), where the input signal is compared to the simulated and measured received signals (right of the figure). We notice that there is indeed only a small dispersion and distortion of the signal.

The S-parameters of the PED antenna system (without balun) were obtained after de-embedding of the half balun at each antenna. The balun de-embedding was done considering the whole antenna system as in Figure 5.18. The S-matrices of the whole system $[T]$ and of the back to-back-baluns $[B_1][B_2]$ are directly obtained from measurements and from simulations. Matrix $[A]$ of the antennas without balun, can be as well calculated from simulations. Therefore the de-embedding is only needed to obtain $[A]$ from measurements.

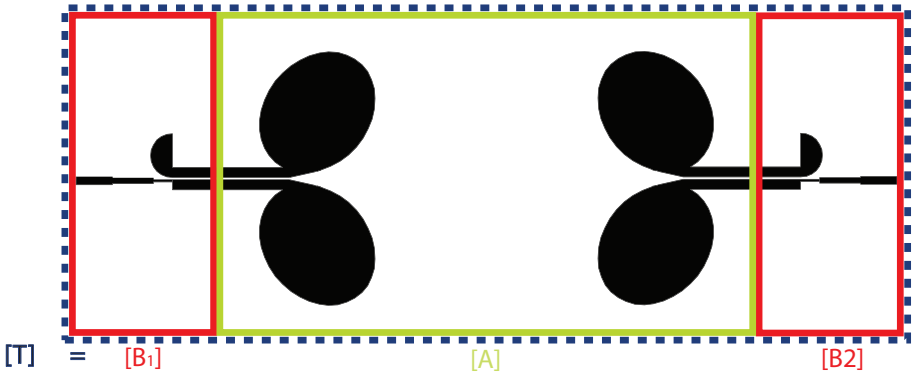

Figure 5.18.: De-embeding of PED antenna with balun.

Matrix $[A]$ can be written as:

$$[A] = [B_1]^{-1}[T][B_2]^{-1} \tag{5.5}$$

$$\begin{bmatrix} S_{11}^A & S_{12}^A \\ S_{21}^A & S_{22}^A \end{bmatrix} = \begin{bmatrix} S_{11}^{B_1} & S_{12}^{B_1} \\ S_{21}^{B_1} & S_{22}^{B_1} \end{bmatrix}^{-1} \begin{bmatrix} S_{11}^T & S_{12}^T \\ S_{21}^T & S_{22}^T \end{bmatrix} \begin{bmatrix} S_{11}^{B_2} & S_{12}^{B_2} \\ S_{21}^{B_2} & S_{22}^{B_2} \end{bmatrix}^{-1} \tag{5.6}$$

All the values of $[S^T]$ are known. This is not the case for $[S^B]$, as the transmission parameters S_{21}^B and S_{12}^B cannot be directly obtained from measurements. Reciprocity can be applied between the two ports. The transmitted power is assumed to be half. A perfect transmission from the balun to the antenna port is assumed, meaning no reflection in the internal ports of the balun. Therefore, the following assumptions are done:

$$\begin{aligned} S_{11}measured &= S_{11}^{B_1} \\ S_{22}measured &= S_{22}^{B_2} \\ 0 = S_{22}^{B_1} &= S_{11}^{B_2} \\ S_{21}measured = \sqrt{S_{21}^{B_1}} &= \sqrt{S_{12}^{B_2}} \\ S_{12}measured = \sqrt{S_{12}^{B_1}} &= \sqrt{S_{21}^{B_2}} \end{aligned}$$

In order to facilitate the computation of the final result, the matrices were changed into ABCD-parameters. Having as reference impedance $Z_C = 50\ \Omega$. The resulting S-parameters are plotted in Fig. 5.19(a) together with the simulated values. The measured value is above -10 dB after 6 GHz, which is clearly an effect of the balun. As seen in Fig. 5.14, the insertion loss of the balun increases after 6 GHz.

The received pulses in time domain (Fig. 5.19(b)) show that the measured received pulse is more dispersed than the simulated one. This is due to the balun de-embedding, as it is not possible to totally eliminate the effects of the balun on the antenna. On the other hand, the received pulses are clearly less dispersed than the pulses in Fig. 5.17(b), showing that the dispersion inside the balun is high.

The de-embedding method can give a good approximation of the antenna performance without balun. In order to improve it, the real S-parameters of the balun should be found, unfortunately they cannot be directly obtained with the measurement equipment available at our lab. A differential VNA would be required to obtain the parameters at the CPS lines.

5.3.1.4. Gain and Radiation Pattern

The measured gain of the PED antenna without balun was obtained from its transfer function (S_{21}) in Fig. 5.19(a), and calculated using equation (4.25). The gain of the antenna without balun was calculated directly from measurements. In Fig. 5.20, the gains are plotted, showing

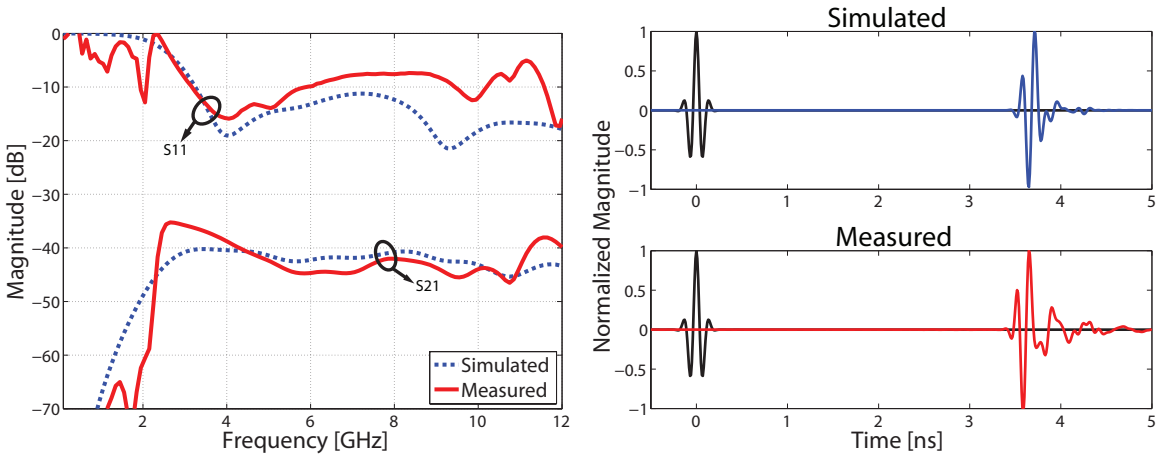

(a) PED antenna system S-parameters.

(b) Time domain signal simulated and measured.

Figure 5.19.: Transfer function and received pulse

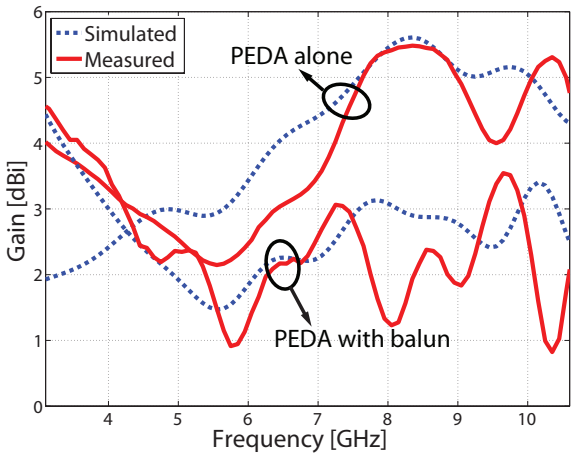

Figure 5.20.: PED antenna Gain in the UWB band (3.1 - 10.6 GHz).

good concordance between simulation and measurements. The gain of the PED antenna with balun is lower than the PED antenna (without balun) after 5.5 GHz, which is due to the mismatch of the balun.

Radiation pattern measurements were done with the PED antenna with balun inside an anechoic chamber. The measurements show that antenna radiation is stronger in the $+z$ direction. The radiation in the $-z$ direction is 5 dB lower than in the $+z$ direction, showing with this the increased directivity of the PED antenna with respect to a classical elliptical dipole. The pattern is symmetric in the X-Z plane as expected, but the Y-Z plane is clearly asymmetric. Two assumptions on the cause of this asymmetry can be done: 1) it is due to radiation produced by the balun, 2) the balun is not feeding the antenna in a perfect symmetrical way.

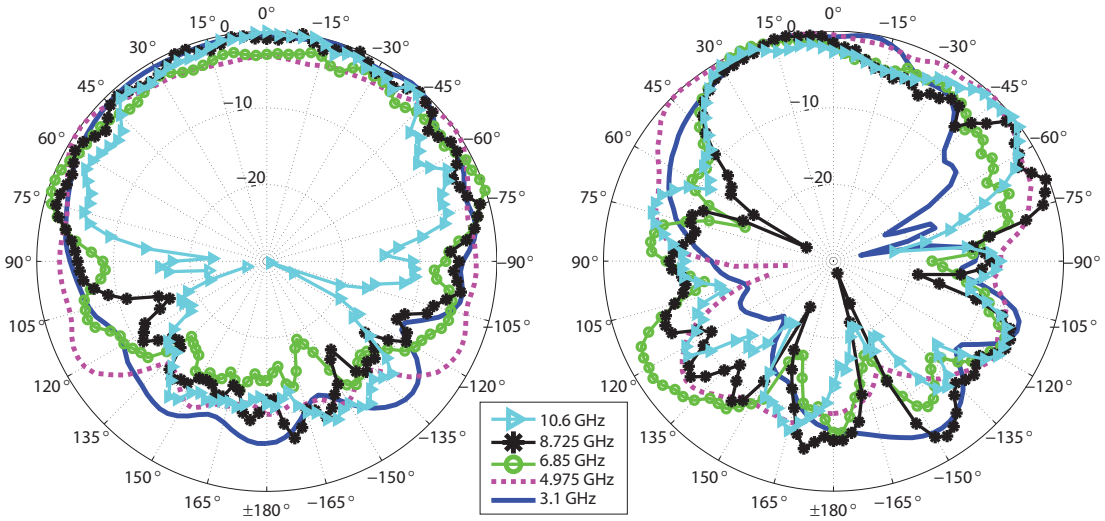

Figure 5.21.: Radiation pattern: a) X-Z plane and b) Y-Z plane.

5.3.2. Dipoles for ECC UWB

The European Electronic Communications Committee (ECC) assigned a band that is narrower than that assigned by the FCC for UWB communications. The broadest usable bandwidth is between 6 and 8.5 GHz, as described in Section 2.4. The bandwidth is considerably smaller than the one proposed by the FCC. For the specific application, the required bandwidth is 1 GHz, centered at 6.5 GHz. It was shown in [15] that transmitting a pulse with the given specification will result in a small distortion of the pulse (if the antenna gain and phase of the transfer function are constant over the band). The antenna distortion is therefore expected to be much less than when transmitting a pulse in the FCC band.

5.3.2.1. Antenna description

The antenna was designed for a specific application which required to be near the human body. The size was the main constraint, as it should fit in a $10 \times 10 \times 10$ mm cube. A large number of designs were studied but only the final design is shown here.

The antenna consists of a circular-ellipsoidal dipole, as the radiators are made by uniting a half circle and a half ellipse. This shape was chosen to reduce the antenna size but keeping the tapering of the structure in order to achieve a large bandwidth. A short-circuit line between the two radiators is used to reduce its size and to make the impedance stable. It was noticed that when the dipole (without the short-circuit line) was located near the skin, the impedance reduces by a factor of two. Short-circuiting the dipole arms have been previously studied by [16] and lately analyzed in bowtie and biconical antennas in [17] and [18] respectively.

Two structures were fabricated in order to analyze the behavior of the antenna. The

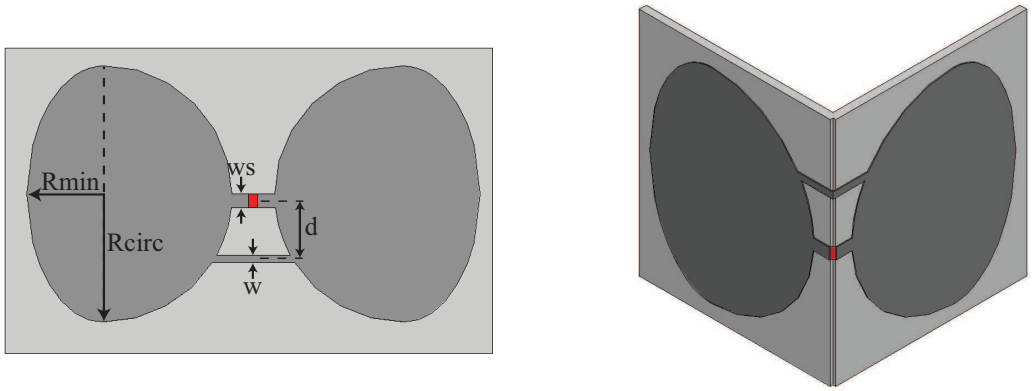

(a) (b)

Rcirc	Rmin	ws	w	d
4.9 mm	2.94 mm	0.45 mm	0.25 mm	3 mm

Figure 5.22.: Flat and folded dipole and dimensions.

dipole was first designed in a planar substrate, covering a total surface of less than 20×10 mm As the available size was very small, the only way to put the dipole in the walls was to fold the dipole arms. The radiators are located in a 90°angle from each others in order to fit each radiator in a wall of the specified cube.

The flat version of the dipole in Fig. 5.22 was elaborated to compare the effect of folding the radiators. The same parameters were used for both folded and flat versions. They were fabricated in a 0.3 mm thick FR4 substrate. The distance between the two feeding lines is the same as the substrate, as a microstrip-to-paired strips balun was used to feed the dipoles.

5.3.2.2. UWB Balun: Microstrip-to-paired strips

The best method to correctly feed the dipole is to use paired strips, each strip connected to a dipole arm. Paired strips is the name given to this type of transmission line in [19], and is the nomenclature used in Appendix B.

The transition between a microstrip line and paired strips is simple to implement. While the microstrip line continues to form one strip, the ground plane becomes the other strip by a smooth tapered reduction in width. The back-to-back balun and its dimensions are shown in Fig. 5.23. The width of the line in the center of the balun **ws** is transversally connected to the dipole terminals in Fig. 5.22, and therefore the value is the same. The microstrip line width $\mathbf{w}_0$ was chosen to have a 50 Ω impedance. The impedance of the paired strips (71 Ω) was calculated using equations in Appendix B. The thickness of the substrate (**h**) was chosen according to the material available and the impedance required to have a good matching of the antenna.

Even though the antenna design was made for the $6 - 8.5$ GHz band, the balun covers a broader spectrum. As shown in Fig. 5.26 the balun back-to-back has an S_{11} of -10dB and an

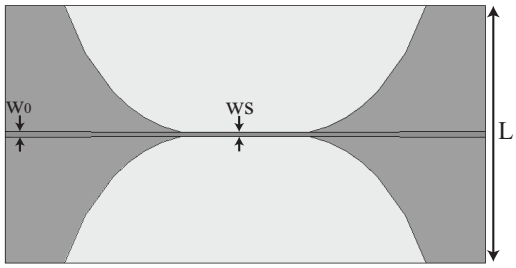

ws	w_0	L
0.45 mm	0.58 mm	30 mm

Figure 5.23.: Microstrip-to-paired strips Balun and dimensions.

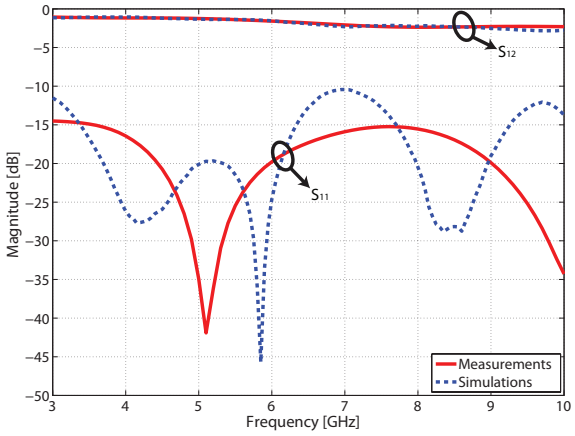

Figure 5.24.: S-parameters of Microstrip-to-paired strips balun.

almost constant insertion loss S_{21} over all this band. The lowest value is -2dB at the lower frequencies, while at higher frequencies this is -3 dB.

5.3.2.3. Results

Reflection Coefficient

The antennas and the balun were fabricated in FR4 substrate and glued together. The flat dipole was printed on one piece of substrate, while the folded dipole needed two pieces. The folded dipole arms are at 90°with respect to each other and 135°from the balun. The gluing and soldering processes were very delicate, as the mentioned angles were crucial for the correct feeding of the antenna. The short-circuited line was as well manually glued, connecting each of the substrate pieces with an external wire and soldering them together to do a perfect connection. The gluing process took several days, allowing the glue to dry correctly in the different parts it was applied. The fabricated antennas are shown in Fig. 5.25

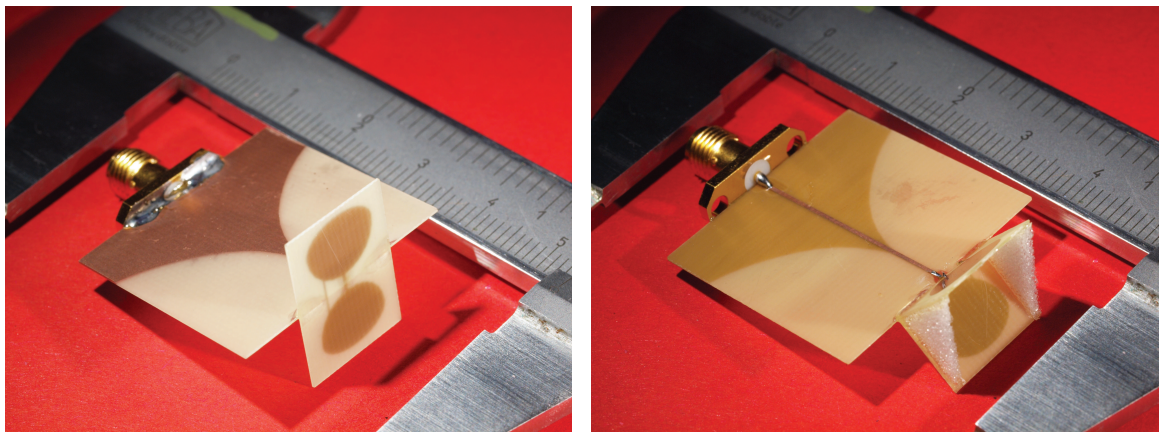

(a) (b)

Figure 5.25.: Measured dipoles connected to the balun and SMA connector. (a) Flat dipole, (b) Folded dipole.

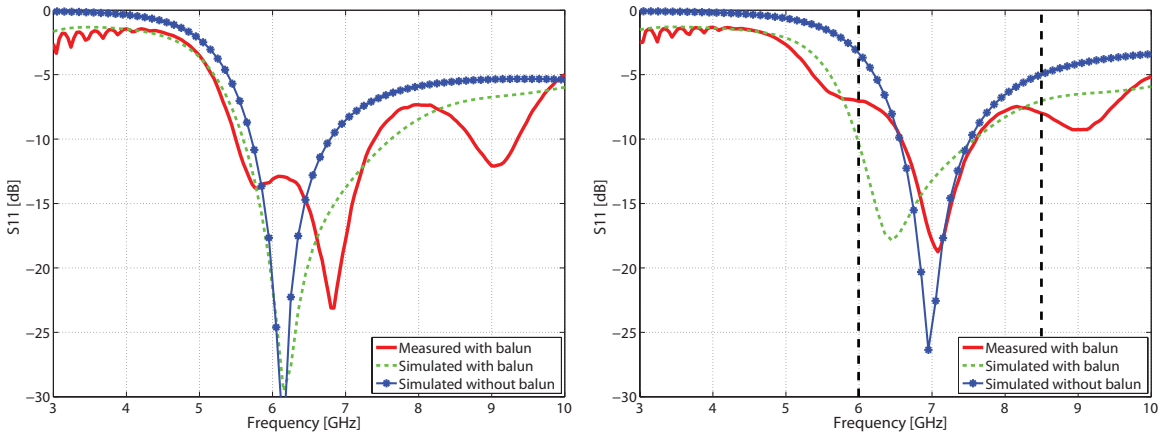

(a) (b)

Figure 5.26.: Reflection coefficient of: (a) Flat dipole, (b) Folded dipole.

The reflection coefficient (S_{11}) of the folded and flat antennas is shown in Fig. 5.26. Simulation results from HFSS are plotted together with measurements for the sake of comparison. The resonant frequency of the folded dipole (Fig. 5.26(b)) is 1 GHz higher than that of the flat dipole (Fig. 5.26(a)). This was already seen in simulations of the dipoles without balun. The flat dipole has a larger bandwidth than the folded dipole, which is almost 2 GHz for the flat dipole and only 1 GHz for the folded dipole.

Flat dipole

Simulations of the flat dipole with and without balun were done using the same bandwidth as for the other antennas ($0.05 - 20.05$ GHz). This was decided in order to have a good comparison between all the studied elements. The input pulse, on the other hand, had to be adapted to the special requirements and characteristics of the antenna. It is a gaussian pulse with center frequency $f_C = 6.5$ GHz and 0.154 fractional bandwidth (1 GHz). The pulse spectrum is shown in Fig. 5.27(a), together with the transfer function of the antenna system. The gain and radiated E-field phase were obtained over the omnidirectional plane of the dipole (ϕ).

In Fig. 5.27(c), the input time signal is compared to the received pulse, showing almost no difference at any angle. The signals of the dipole with balun are a bit retarded from those of the dipole without blaun, which is an obvious effect of the dipole. Still, no difference between the pulses can be recognized. The same time delay is found in Fig. 5.27(b), where the delay at each angle (dipole with balun system) can be more clearly seen. The small distortion of the pulses, at every direction, is clear when seeing the SFF plot in Fig. 5.27(d), being larger than 0.95 in every direction.

The gain pattern of the dipole with balun is shown in Fig. 5.27(e) and of the dipole without balun in Fig. 5.27(f). For both dipoles the gain is constant in the $5.5 - 6$ GHz. The dipole with balun has a very low gain at frequencies below 4 GHz (notice that the scales are not equal), it could be attributed to the balun mismatch at these low frequencies.

Folded dipole

The plane of analysis is the same as for the flat dipole, the symmetry plane between the dipole arms. The plane is normal to the port and the dipole arms are 45°rotated from this plane. The $\phi = 0°$ direction is between the two dipole arms, the direction where a higher directivity is expected.

The simulation results in Fig. 5.28 show important differences from the flat dipole. The folded dipole has a smaller effective area than the flat dipole. This could be translated to an increase on the frequency of operation. The transfer function in Fig. 5.28(a) is shifted to higher frequency, compared to the transfer function of the flat dipole in Fig. 5.27(a). This was as well expected from the reflection coefficient results shown in Fig. 5.26.

No difference can be appreciated directly from the time domain signals in Fig. 5.28(c), which may lead to the assumption that the same distortion as with the flat antenna is produced. The SFF plot in Fig. 5.28(d) helps to verify this hypothesis. The SFF of the folded dipole is also above 0.95 for every azimuth angle, but at some directions the value is higher than at other directions. This is as well a factor of the increased directivity compared to the flat dipole.

The difference in the gain patterns is clear. The antenna gain is constant in the $5.5 - 7$ GHz band, and higher at $\phi = 0°$ than at $\phi = \pm 180°$ (Fig. 5.28(e) and Fig. 5.28(f)). This shows an increase of directivity in that direction. This is a similar effect as the one found

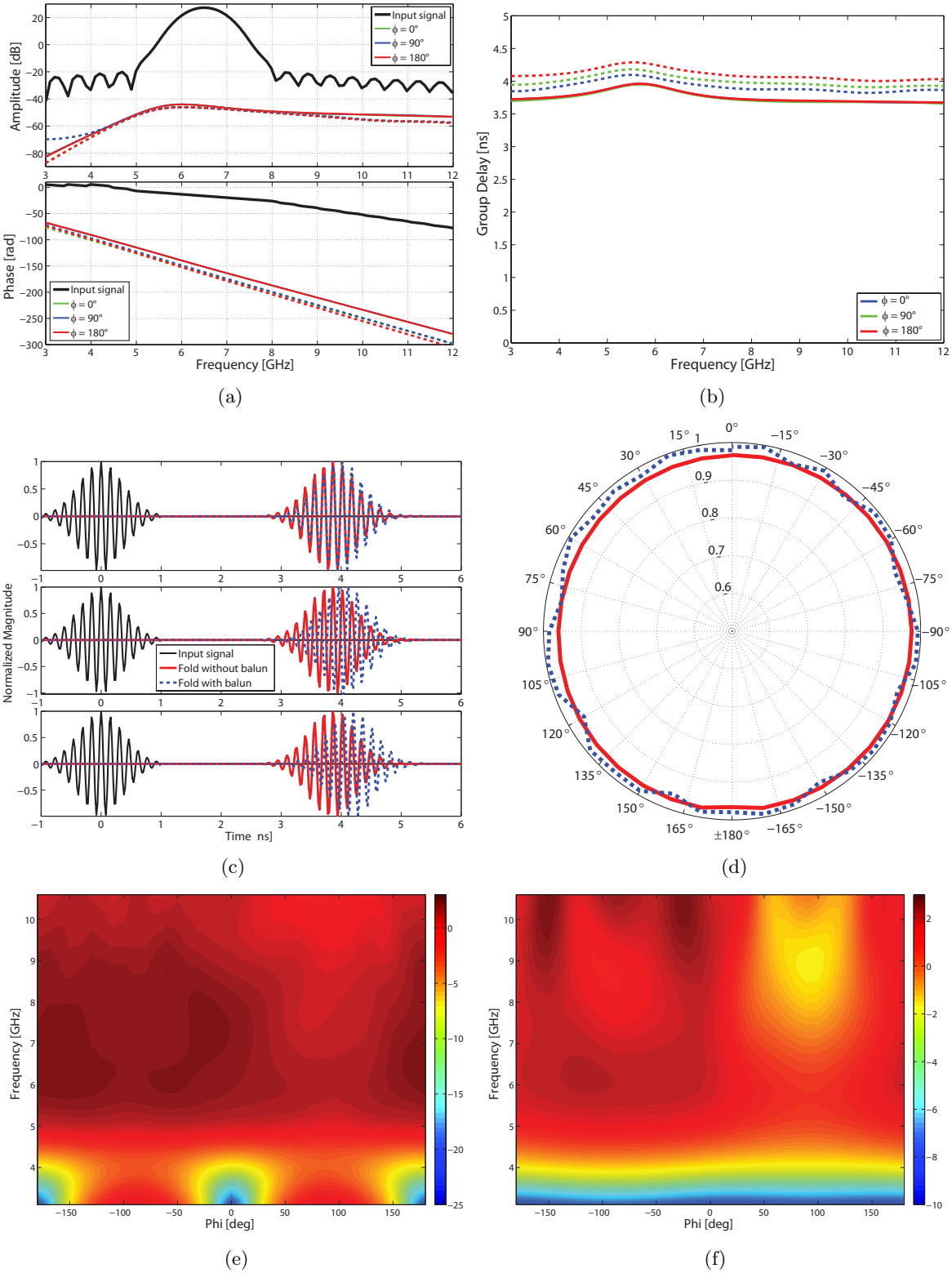

Figure 5.27.: Simulated results of flat dipole with (dashed lines) and without balun (solid lines). (a) System transfer function and impulse pulse spectrum(at $\phi = 0°, 90°$ and $180°$), (b) Group Delay (at $\phi = 0°, 90°$ and $180°$), (c) Time signals at 3 different directions ($\phi = 0°, 90°$ and $180°$), (d) System Fidelity Factor, (e) Gain Pattern (with balun), (f) Gain Pattern (without balun).

in the PED antenna on the previous section.

Results from both antennas predict a small pulse distortion, confirming that a 1 GHz pulse suffers from small distortion if compared to an UWB pulse from the FCC regulations (7.5 GHz bandwidth). These results were satisfactory and no further measurements of the SFF were done, considering that results would be similar to simulations.

A question may arise about the increase directivity of the antenna produced by the folding of the dipole arms. This increase in directivity is not seen in the SFF. The antenna gain is higher at $\phi = 0°$ according to Fig. 5.28(f), but it should not be forgotten that the SFF does not compare the radiated power, as the pulses are normalized. Therefore the SFF is omnidirectional, which means the amount of distortion produced by the antenna is the same in every angle of radiation, even if the pulses might have a different magnitude at some directions.

If measurements are required, the effect of the balun should be considered as with the PED antenna in Section 5.3.1. A balun de-embedding can be done as well following the same procedure as in the mentioned section.

5.4. Tips and hints for UWB antenna designers

Some general recommendations for UWB antennas design were derived from the experience acquired in this thesis. The tips given in this section are valid for monopoles and dipoles in general. There might be other important tips that apply only to some specific designs, but we will focus on generalities. The idea of this section is to give some introductory basis for designers to easily implement an UWB antenna. Based on these starting tips, the designer is free to play with his/her creativity and build a good design from the base.

- **Tapered structures** promote a wide antenna bandwidth. Schantz in [20] says the fundamental UWB antenna principle: "fatter is better". The optimum connection between an input line and the fat dipole or monopole element is a tapering transformation. An impedance matching can be easily obtained by applying this technique.
- **A large ground plane** is required to avoid spurious currents in the cable when measuring a monopole antenna. The ground plane should be at least the same size of the monopole radiator in order to eliminate these currents. Reducing the ground plane to reduce the total size of the antenna, leads to incorrect measurements. In a real application, the total size of the system will be larger than the antenna. The system itself works as a ground plane, therefore it is important to consider it when doing the measurements. If this is not possible, precautions should be taken to eliminate the currents from the cable. This could be done by using absorbers or chokes.
- **Short-circuit line connecting dipole arms** reduces the dipole size as well as its bandwidth. To obtain the maximum bandwidth, a tapered or large area of the arms is required. The input impedance of the short-circuited dipoles is four times larger than that of the ordinary dipole [21].
- **Rotate dipole arms**, do not stay in the conventional definition of a dipole. Rotating

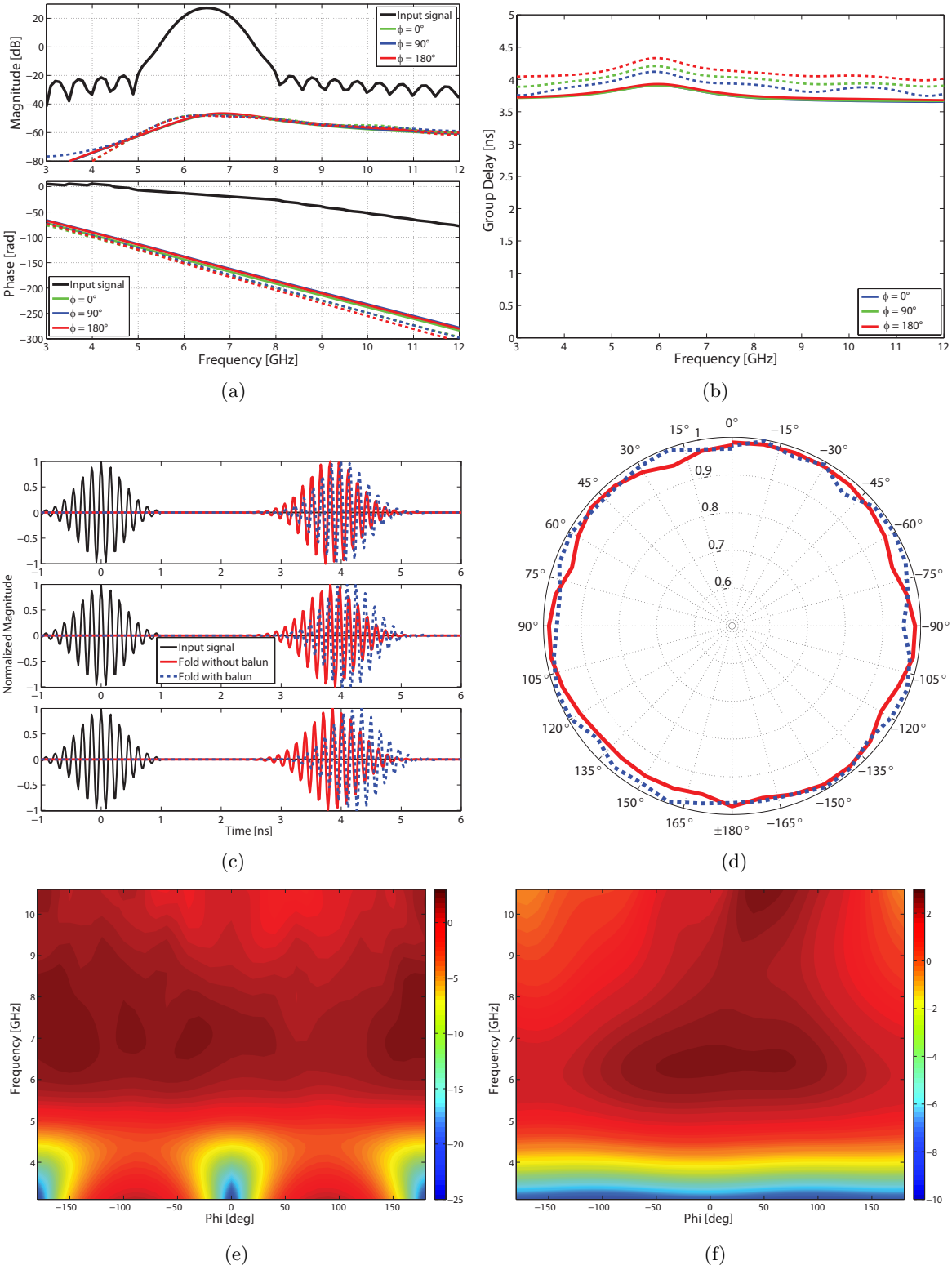

Figure 5.28.: Simulated results of folded dipole with balun (dashed lines) and without balun (solid lines). (a) System transfer function and input pulse spectrum (at $\phi = 0°, 90°$ and $180°$), (b) Group Delay (at $\phi = 0°, 90°$ and $180°$), (c) Time signals at 3 different directions ($\phi = 0°, \phi = 90°$ and $180°$), (d) System Fidelity Factor, (e) Gain Pattern (with balun), (f) Gain Pattern (without balun).

the arms with respect to their own center (as in Section 5.3.1) increases its directivity. This is a good option for the cases where we do not want to loose radiation towards a given direction. Rotating the arms with respect to the feeding point (as in Section 5.3.2) allows it to be placed in smaller areas, as it can be literally cut in half. According to [21], the input impedance is generally less than that of a straight dipole of the same length.

5.5. Conclusion

Three novel UWB antennas were presented in this chapter. The antennas were characterized using the conventional antenna methods described in Chapter 3. Antenna systems composed of identical antennas were studied, calculating its transfer function, received pulse and the system fidelity factor. With the SFF plots, an efficient comparison of the antennas was realized.

The tapered monopoles in Section 5.2 showed that the SFF reduces (in all directions) when increasing the permittivity of the substrate. From the measurements we showed the importance of having a large plane, thus no spurious currents in the cable, in order to have accurate results.

In Section 5.3.1 a method to calculate the differential return loss from a CPS line fed dipole was shown. A novel balun design was implemented, showing better performance than others found in literature. The PED antenna showed low dispersion of the pulse in the studied direction $+z$ and a 5 dB higher directivity at $+z$ than at $-z$.

The small dipoles designed for the ECC mask showed a very good performance in the simulations. The reflection coefficient was measured with the help of a balun, and it correspond well to the simulated values. The dipoles showed a constant gain over the desired band and a constant group delay, which are important parameters that promote a good radiation of the pulse. It is with the SFF plot that the dipole is shown to be really omnidirectional when transmitting the 1 GHz pulse. The balun affecting few in the performance of the antenna.

From the antenna designs presented, some interesting tips and advices were derived and explained. The tips describe antenna characteristics that an antenna designer should have in mind when starting a new design. These advices together with the characterization methods proposed in this thesis help to obtain good UWB antenna performances.

References

[1] Y. Lee, J. Sun, and W. Huang, "A study of printed monopole antenna for ultra wideband applications," *Microwave and Optical Technology Letters*, vol. 49, pp. 1435 – 1438, 2007.

[2] Y. J. Y. Zhao, and, G. Zhao, L. Zhang, Y. Song, and Z. Wong, "Compact planar monopole UWB antenna with band-notched characteristic," *Microwave and Optical Technology Letters*, vol. 50, pp. 2656 – 2658, 2008.

[3] Y. C. Lee and J.-S. Sun, "A tapered monopole antenna with band notch function for ultra-wideband communication," in *The 2nd International Conference on Wireless Broadband and Ultra Wideband Communications*, August 2007.

[4] J. S. McLean, "A re-examination of the fundamental limits on the radiation Q of electrically small antennas," *IEEE Trans. Antennas Propag.*, vol. 44, no. 5, p. 672, May 1996.

[5] C. A. Balanis, *Antenna Theory. Analysis and Design.*, Third ed. Wiley-Interscience, 2005.

[6] G. Quintero and A. K. Skrivervik, "Analysis of planar UWB elliptical dipoles fed by a coplanar stripline," in *Proc. IEEE International Conference on Ultra-Wideband ICUWB 2008*, vol. 1, Sep. 10–12, 2008, pp. 113–116.

[7] T. W. Hertel, "Cable-current effects of miniature uwb antennas," in *Proc. IEEE Antennas and Propagation Society International Symposium*, 2005, pp. 524–527.

[8] J. F. Zürcher, O. Staub, A. K. Skrivervik, and M. Hermanjat, "Accurate measurement of the maximum gain of electrically small antennas," *Microwave and Optical Technology Letters*, vol. 23, pp. 328–331, 1999.

[9] G. Quintero, J. F. Zürcher, and A. K. Skrivervik, *Ultra-Wideband, Short-Pulse Electromagnetics 9 (UWB SP 9) book.* Springer, 2010, ch. 29. Planar Elliptical Differential Antenna for UWB Applications, pp. 269 – 278.

[10] Z. Chun-Qing, W. Jun-Hong, and H. Yu-nan, "Coupled planar dipole UWB antenna design for wearable computer," in *Proc. International Conference on Microwave and Millimeter Wave Technology ICMMT '07*, Apr. 18–21, 2007, pp. 1–4.

[11] J. Powell and A. Chandrakasan, "Differential and single ended elliptical antennas for 3.1-10.6 GHz ultra wideband communication," in *Proc. IEEE Antennas and Propagation Society International Symposium*, vol. 3, Jun. 20–25, 2004, pp. 2935–2938.

[12] K. D. Palmer and M. W. van Rooyen, "Simple broadband measurements of balanced loads using a network analyzer," *IEEE Trans. Instrum. Meas.*, vol. 55, no. 1, pp. 266–272, Feb. 2006.

[13] R. E. Collin, *Foundations for Microwave Engineering*, 2nd ed. Mc Graw-Hill, 1992.

[14] W.-H. Tu and K. Chang, "Wide-band microstrip-to-coplanar stripline/slotline transitions," *IEEE Trans. Microw. Theory Tech.*, vol. 54, no. 3, pp. 1084–1089, Mar. 2006.

[15] G. Quintero, J. F. Zurcher, and A. Skrivervik, "Omnidirectional pulse dispersion of planar circular monopoles," in *Proc. IEEE International Conference on Ultra-Wideband ICUWB 2009*, Sep. 9–11, 2009, pp. 395–399.

[16] R. Bourtoutian, C. Delaveaud, and S. Toutain, "Differential, shorted dipole antenna for european uwb applications," in *Antennas and Propagation, 2007. EuCAP 2007. The Second European Conference on*, nov. 2007, pp. 1 –5.

[17] H. Wong, K.-M. Mak, and K.-M. Luk, "Wideband shorted bowtie patch antenna with electric dipole," *Antennas and Propagation, IEEE Transactions on*, vol. 56, no. 7, pp. 2098 –2101, july 2008.

[18] A. Amert and K. Whites, "Miniaturization of the biconical antenna for ultrawideband applications," *Antennas and Propagation, IEEE Transactions on*, vol. 57, no. 12, pp. 3728 –3735, dec. 2009.

[19] B. C. Wadell, *Transmission Line Design Handbook*. Artech House, 1991.

[20] H. Schantz, *The Art and Science of Ultrawideband Antennas*. Artech House, 2005.

[21] W. L. Stutzman and G. A. Thiele, *Antenna Theory and Design*. John Wiley and Sons, Inc., 1981.

6. Conclusions and Future Work

6.1. Summary and Discussion

Even if Ultra-wideband is a relatively new technology, much development and research has been done in the last few years. This thesis has contributed to this research with the implementation of a new characterization method for UWB antennas, as well as with novel antenna architectures from which interesting advices for designers were driven.

In the first part of the thesis, a review of the technology was done, emphasizing the most important concepts for antenna designers. It is often the case that standards and regulations are very difficult to read. This is why, we synthesized the information contained in them, mentioning the parameters and constraints that are closely related to the antenna, and which are therefore most useful for antenna designers. Such is the case of radiated power measurements, which can be sometimes confusing to read from the different sources and regulations. Hence we described the spectrum analyzer settings needed to elaborate the measurements and fulfill the requirements established by the standards.

The third chapter gives a detailed list of the characterization methods available today to analyze UWB antennas. A thorough description of how to calculate them by measurements or simulations was given. This facilitate the task of future designers as well, having all these methods together. However, we found that with the methods studied, a full characterization of an UWB antenna is not possible. The methods focus either on the frequency or time domain, and are limited to only one direction of operation of the antenna. The main objective of this thesis is to characterize omnidirectional antennas, and it was found that with the conventional parameters this is not an easy task. They give important information about antenna performance, but do not manage to make a full analysis which could be used to compare antennas in a given plane.

This was the reason why we implemented a new characterization method that could contain all the frequency and time domain characteristics of an antenna over its omnidirectional plane. This can be done with the simulation and measurement tools available in the lab (which are as well common for most antenna designers) and within a reasonable amount of time. The System Fidelity Factor fulfills these requirements.

Another contribution of this thesis is the method to obtain the simulated transfer function of a two identical antenna system. The method uses the simulated values of a single antenna and computes the transfer function of the system in a given plane. The transfer function of the system can be separated in the transfer function of the transmitting antenna, the receiving antenna and the channel. This gives freedom to choose any antenna and use it as a

transmitter or a receiver. It also allows the designer to use a channel different from free space, e.g. for indoor UWB applications a multipath environment might be interesting to analyze. This leads to some interesting applications that will be discussed in the following section.

The process to obtain the receiving pulse from the transfer function and the input pulse was described. The SFF is then obtained by the correlation of both the received and input pulses. The SFF is plotted in a polar plot, containing the angular and time characteristics of the receiving antenna compared to a fix transmitting antenna. This allows an easy and fair comparison between different antenna systems.

An excellent agreement between simulations and measurements was achieved. This was shown using first some well known UWB antennas. The SFF was also used to compare the performance of the novel antenna designs which are a further contribution of this thesis.

Using the SFF we could confirm that antennas with a bandwidth smaller than 1 GHz, produce very small distortion on the transmitted pulse. This is also true for an UWB antenna sending a narrow pulse (BW $<$ 1 GHz), as long as the gain of the transfer function is constant and its phase linear over the frequency band of the transmitted pulse.

6.2. Perspectives

The SFF, as presented in this thesis, is an antenna characterization method used to compare antennas in an ideal environment. The antennas were simulated in free space and the transfer function measured in an anechoic chamber. These are standard characterization environments used on antenna analysis in our days. Nevertheless, it is important to characterize an antenna system in its real environment. As mentioned in the previous sections, a great advantage of the proposed method is that the transfer function can be separated. If we want to characterize the antenna in other a than free- space environment, only the transfer function of the channel has to be modified. The transfer function of the antennas will remain the same as it only depends on the antenna gain and the phase distortion inside the antenna structure.

Channel simulations are out of the scope of this thesis, but it could be easily implemented in future applications. Summations of the channel might be quite problematic, as in a real world environment multiple reflections occur and they are different at every direction, hence a different channel should be used for every angle of radiation. This might be difficult but not impossible to implement by a highly motivated channel expert.

Measurements of the SFF in a real world environment can be done in the same way as in the anechoic chamber, the only restriction being the length of the high quality cables of the VNA. The SFF could then be used to measure the channel on a multipath environment. The antennas transfer functions are known, so the only unknown left is the channel.

The input signal at the Tx antenna terminals was used as a reference signal which was compared with the receiving pulse. This was done to show only a general case of the SFF. However, the reference signal might be chosen according to the specific application, i.e. the reflected input signal inside a room. Furthermore, the pulse itself might not be interesting for

some applications, but the envelope of the pulse or its peak power. The reference signal can be easily modified using the described pulse, and many combinations are possible where only the time-signal reference has to be changed. Again this will give more realistic results with a higher level of information for system designers.

The SFF has a great potential to be used as a standard characterization method of UWB antennas. In this thesis, mainly the characterization of the antenna system was done. In order to compare only the characteristics of one antenna, a reference Tx antenna should be used. This antenna should have excellent UWB characteristics in the direction of transmission. The method would then be similar to the case, given in this thesis, where the Vivaldi antenna was used at transmission and three circular monopoles at reception. With the standard Tx antenna the characterization method is homogenized and a direct comparison between the receiving antennas can be done.

The first two antenna designs shown in Chapter 5 were developed with no specific application in mind. Nevertheless, the PED antenna has excellent characteristics to be used in a planar circuit with differential input. The last antenna design presented is part of an interesting project that might be completed in the following years. The antenna is meant to work in a body area network, hence it was simulated as well near human tissue, showing an excellent performance. The results were not presented in this thesis due to confidentiality reasons, but its small size, UWB performance and good radiation in proximity of the skin, make it an excellent candidate for this application.

Using the SFF to analyze the antenna performance will facilitate the realization of novel antennas to the designers. This parameter could be used together with the other characterization methods described in this thesis to make a full UWB characterization. These methods together with the tips given in the last chapter make this thesis a good reference for UWB antenna designers.

A. Antenna Reciprocity Theorem

Maxwell's equations in the differential form are defined as [1]

$$\begin{aligned} \nabla \times \mathbf{E} &= -\frac{\partial \mathbf{B}}{\partial t} \\ \nabla \times \mathbf{H} &= \mathbf{J} + \frac{\partial \mathbf{D}}{\partial t} \\ \nabla \cdot \mathbf{J} &+ \frac{\partial \rho}{\partial t} \\ \nabla \cdot \mathbf{B} &= 0 \\ \mathbf{B} &= \nabla \times \mathbf{A} \end{aligned}$$

where $\mathbf{A}$ is the vector potential.

Lorentz' reciprocity theorem of the antenna system in Fig. A.1 can be written in the time domain as [2]

$$\int\int_V (\mathbf{J}_1 \cdot \mathbf{E}_2 - \mathbf{J}_1 \cdot \mathbf{E}_1) dV dt = \int\int_S (\mathbf{E}_1 \times \mathbf{H}_2 - \mathbf{E}_2 \times \mathbf{H}_1) dS dt \tag{A.1}$$

Assuming that the sources are positioned within a finite region and the fields are observed in the far field, the electric field is related to the vector potential $\mathbf{A}$ via

$$\mathbf{E}(\mathbf{r}, t) = -\partial_t \mathbf{A}_{||}(\mathbf{r}, t) \tag{A.2}$$

where $||$ denotes the transverse component relative to the observation direction $\hat{\mathbf{r}}$ $[\mathbf{A}_{||} = \mathbf{A} - \hat{\mathbf{r}}(\hat{\mathbf{r}} \cdot \mathbf{A})]$. The right part of Lorentz' theorem equals zero, thus simplifying to

$$\int\int_{V_1} \mathbf{J}_1 \cdot \tilde{\mathbf{E}}_2 dV dt = \int\int_{V_2} \tilde{\mathbf{J}}_2 \cdot \mathbf{E}_1 dV dt \tag{A.3}$$

where $\mathbf{E}_1$ is the field due to $\mathbf{J}_1$ while $\tilde{\mathbf{E}}_2$ is the *adjoint field* due to $\tilde{\mathbf{J}}_2$. V_1 and V_2 are the supporting volumes of $\mathbf{J}_1$ and $\mathbf{J}_2$ respectively. The adjoint current $\tilde{\mathbf{J}}_2$ is considered to be zero from a certain time on, whereas $\mathbf{J}_1$ is zero up to a certain time [3].

The radiating vector potential $\mathbf{A}_1(r, t)$ is given by the *retarded potential integral*, whereas $\tilde{\mathbf{A}}_2$ is given by the so called *adjoint potential integral*

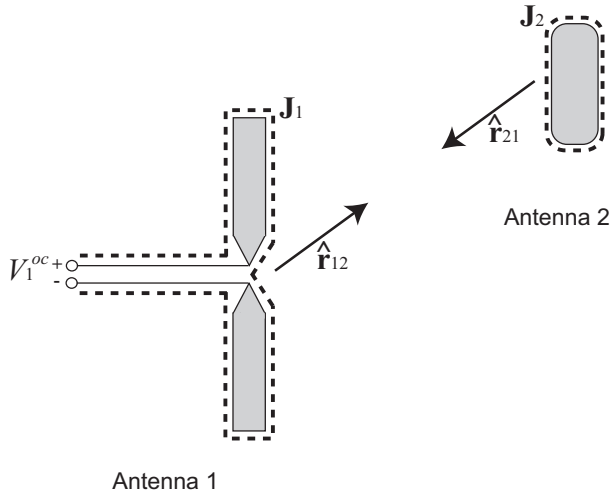

Figure A.1.: Time-domain reciprocity. (Figure adapted from [3])

$$\mathbf{A}_1 = \frac{\mu}{4\pi}\int_V \frac{\mathbf{J}_1(r', t - |\mathbf{r} - \mathbf{r}'|/c)}{|\mathbf{r} - \mathbf{r}'|} dV \tag{A.4}$$

$$\tilde{\mathbf{A}}_2 = \frac{\mu}{4\pi}\int_V \frac{\tilde{\mathbf{J}}_2(r', t + |\mathbf{r} - \mathbf{r}'|/c)}{|\mathbf{r} - \mathbf{r}'|} dV \tag{A.5}$$

$|\mathbf{r} - \mathbf{r}'| = R$ is the absolute distance between antenna 1 and antenna 2. Both the retarded and adjoint potentials are proper solutions of Maxwell's equations, but the adjoint solution does not satisfy the causality theorem. As explained in [1], it represents a wave radiating outward from the source with the time running backward or a wave collapsing on its source with time going forward.

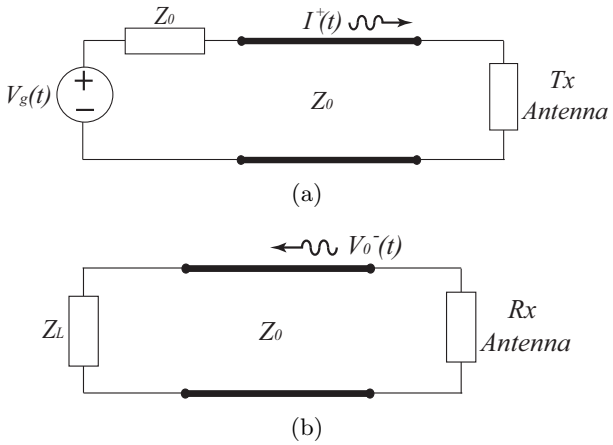

Figure A.2.: Tx and Rx antenna circuits.

Lorentz' theorem could be interpreted in two different ways: 1) considering $\mathbf{J}_1$ as the induced current in the antenna, hence the antenna structure as part of the medium, and 2) considering $\mathbf{J}_1$ as an independent source radiating in free space. Both cases are applied to the left side of (A.3) to obtain the relation between the radiating and receiving effective heights.

1) Lets consider now the antenna circuit in Fig. A.2(a). Antenna 1 is working at transmission, $\mathbf{J}_1$ is the source at the antenna ($I_1(t)$) and $\tilde{\mathbf{E}}_2$ is computed in presence of the antenna structure. The left-hand side of (A.3) is then

$$\int I_1(t)dt \int \tilde{\mathbf{E}}_2(\mathbf{r},t)ds = -\int I_1(t)\tilde{V}_1^{oc}(t)dt \tag{A.6}$$

$\tilde{\mathbf{E}}_2(\mathbf{r},t)$ is the field due to I_2 when $I_1 = 0$, therefore the open-circuit field, and the voltage induced at antenna 1 terminals due to $\tilde{\mathbf{E}}_2(\mathbf{r},t)$ is

$$\tilde{V}_1^{oc}(t) = -\int_-^+ \tilde{\mathbf{E}}_2^{oc}(\mathbf{r},t)ds$$

We can now calculate the input current at the transmitting antenna 1, considering the time-domain reflection coefficient $\Gamma_1^t(t)$, then the current is

$$I_1(t) = [\delta(t) - \Gamma_1^t(t)] * I_1^+(t) \tag{A.7}$$

Assuming now antenna 1 to be receiving (Fig. A.2(b)), then the voltage at the antenna terminals is given by

$$[\delta(t) - \Gamma_1^t(t)] * V_1^{oc}(t) = 2V_1^-(t) \tag{A.8}$$

Substituting (A.8) and (A.7) in (A.6) and knowing that $\tilde{V}_1^{oc}(t) = V_1^{oc}(-t)$, the right hand side of (A.6) becomes

$$-2\int I_1^+(t)V_1^-(-t)dt \tag{A.9}$$

and from the definition of convolution and effective height in (4.9) we obtain

$$2\int I_1^+(t)dt \int \mathbf{E}_0(t')\cdot\mathbf{h}_1^r(\hat{\mathbf{r}}_{12},-t-t')dt' \overset{-t'=t}{\longleftrightarrow} 2\int I_1^+(-t')\mathbf{E}_0(-t)\cdot\mathbf{h}_1^r(\hat{\mathbf{r}}_{12},t'+t)dt' \tag{A.10}$$

$$-2\int \mathbf{E}_0(t)\cdot\mathbf{h}_1^r(\hat{\mathbf{r}}_{12},-t'-t)I_1^+(t')dt' = -2\int \mathbf{E}_0(t)\cdot[\mathbf{h}_1^r(\hat{\mathbf{r}}_{12},-t)*I_1^+(-t)]dt' \tag{A.11}$$

2) In the second case the induced current over the antenna structure $I_1(t)$ is considered as an independent source, hence $\mathbf{J}_1$ is assumed to radiate in free space. $\mathbf{E}_2$ is the incident field $\tilde{\mathbf{E}}_2^i = \mathbf{E}_0(-t-\hat{\mathbf{r}}_{21}\cdot\mathbf{r}/c)$, where $\hat{\mathbf{r}}_{21}$ is the unit vector direction from antenna 1 to antenna

2 and is equal to $-\hat{\mathbf{r}}_{12}$.

$$\int\int_{V_1} \mathbf{J}_1(\mathbf{r},t)\tilde{\mathbf{E}}_2^i(\mathbf{r},t)dtdV = \int \mathbf{E}_0(t) \int_{V_1} \mathbf{J}_{||_1}(\mathbf{r}, -t + \hat{\mathbf{r}}_{21}\cdot\mathbf{r}/c)dV \tag{A.12}$$

where $\mathbf{J}_{||_1}$ is the component of $\mathbf{J}_1$ transverse to $\hat{\mathbf{r}}_{21}$.

Using (A.2), the effective height can be described as:

$$\mathbf{h}^t(\hat{\mathbf{r}},\tau) = -\partial_\tau \int \mathbf{J}_{||}^\delta(\mathbf{r}', \tau + \hat{\mathbf{r}}\cdot\mathbf{r}'/c)dV' \tag{A.13}$$

where $\mathbf{J}^\delta$ $[1/\mathrm{m}^2\mathrm{s}]$ is the current distribution due to an impulse input current $I^+(t) = \delta(t)$

Substituting (A.13) in (A.12) we obtain

$$\int \mathbf{E}_0(t)\cdot[\partial_t^{-1}\mathbf{h}_1^t(\hat{\mathbf{r}}_{12}, -t) * I_1^+(-t)]dt' \tag{A.14}$$

∂_t^{-1} denotes an integration. Both (A.14) and (A.10) are derived from the left-hand side of Lorentz' reciprocity in (A.3), we derived then the relation between the transmitting and receiving effective heights:

$$\frac{1}{2}\mathbf{h}^t(\hat{\mathbf{r}},t) = \partial_t \mathbf{h}^r(\hat{\mathbf{r}},t) \tag{A.15}$$

References

[1] W. Welch, "Reciprocity theorems for electromagnetic fields whose time dependence is arbitrary," *IRE Transactions on Antennas and Propagation*, vol. 8, no. 1, pp. 68–73, Jan. 1960.

[2] C. A. Balanis, *Antenna Theory. Analysis and Design.*, Third ed. Wiley-Interscience, 2005.

[3] A. Shlivinski, E. Heyman, and R. Kastner, "Antenna characterization in the time domain," *IEEE Trans. Antennas Propag.*, vol. 45, no. 7, pp. 1140–1149, Jul. 1997.

B. Transmission Lines

The equations to calculate the impedance of the transmission lines and the nomenclature used refers to [1]. Their calculation is out of the scope of this thesis, but they are an important parameter on any dipole design.

B.1. Coplanar Strip line (CPS)

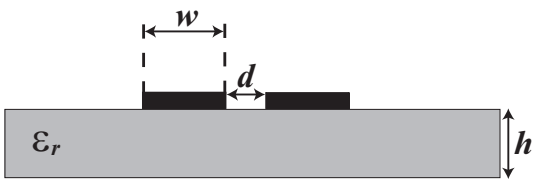

Figure B.1.: Transveral cut of a CPS line.

$$k = \frac{d}{2w + d} \tag{B.1}$$

$$k' = \sqrt{1 - k^2} \tag{B.2}$$

$$k_1' = \sqrt{1 - k_1^2} \tag{B.3}$$

$$k_1 = \frac{sinh\left(\frac{\pi d}{4h}\right)}{sinh\left(\frac{\pi(2w+d)}{4h}\right)} \tag{B.4}$$

$$Z_0 = \frac{\eta_0}{\sqrt{\epsilon_{eff}}} \frac{K(k)}{K(k')} \tag{B.5}$$

$$\epsilon_{eff} = 1 + \frac{\epsilon_r - 1}{2} \frac{K(k')K(k_1)}{K(k)K(k_1')} \tag{B.6}$$

where $\eta_0 = \sqrt{\mu_0/\epsilon_0}$ and K is the complete elliptic integral of the first kind defined as

$$K(k) = \frac{\pi}{2a_N} \tag{B.7}$$

where

$$a_n = \frac{a_{n-1} + b_{n-1}}{2} \tag{B.8}$$

$$b_n = \sqrt{a_{n-1} b_{n-1}} \tag{B.9}$$

to calculate this integral, one should start with the initial values ($a_0 = 1, b_0 = \sqrt{1-k^2}, c_0 = k$) and iterate until $c_N = 0$.

B.2. Parallel Strips or Paired Strips

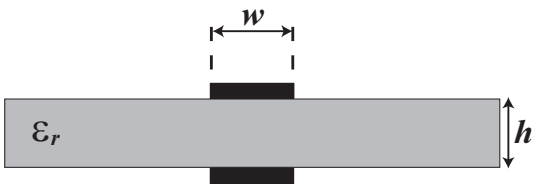

Figure B.2.: Transveral cut of Parallel Strips.

We must first define

$$a = \frac{w}{2}$$

$$b = \frac{h}{2}$$

$$\epsilon = \epsilon_0 \epsilon_r$$

For wide strips ($a/b > 1$):

$$Z_0 = \frac{\eta_0}{\sqrt{\epsilon_r}} \left(\frac{a}{b} + \frac{ln(4)}{\pi} + \frac{\epsilon_r + 1}{2\pi\epsilon_r} ln\left[\frac{\pi\epsilon(a/b + 0.94)}{2} \right] + \frac{\epsilon_r - 1}{2\pi\epsilon_r^2} ln\frac{\epsilon\pi^2}{16} \right)^{-1} \tag{B.10}$$

For narrow strips ($a/b < 1$):

$$Z_0 = \frac{\eta_0}{\pi\sqrt{\epsilon_r}} \left(ln\frac{4b}{a} + \frac{1}{8}\left(\frac{a}{b}\right)^2 - \frac{\epsilon_r - 1}{2(\epsilon_r + 1)} \left[ln\frac{\pi}{2} + \frac{ln(4/\pi)}{\epsilon_r} \right] \right) \tag{B.11}$$

References

[1] B. C. Wadell, *Transmission Line Design Handbook*. Artech House, 1991.

Curriculum Vitae

Gabriela Quintero was born in Chicago, U.S.A., from Mexican parents. She lived in Mexico City until she received her B.Sc. degree in Electronics and Communications Engineer from the Tecnológico de Monterrey, Campus Ciudad de México (ITESM-CCM) in 2003. During her Bachelor studies she participated in an international exchange program at Tampere University of Technology, in Finland (Spring semester 2002).

She moved then to Sweden, where she obtained her M.Sc. degree in Electrical Engineer from Chalmers University of Technology, Göteborg, Sweden in 2005. She attended the international Master's Programme in Hardware for Wireless Communications and did her Master's thesis at Saab Ericsson Space AB (now RUAG Space AB).

In 2006 she started her Ph.D. in the Laboratory of Electromagnetics and Acoustics (LEMA) at the Ecole Polytechnique Fédérale de Lausanne (EPFL), where she has been research and teaching assistant. Her research interests include applied electromagnetism, UWB antennas, measurements and characterization models.

As a research assistant she was involved in the project: "*Very low radiated power UWB communication*" from the National Competence Center in Research on Mobile Information and Communication Systems NCCR-MICS, a center supported by the Swiss National Science Foundation SNFS.

As a teaching assistant she has been involved in the supervision of Bachelor and Master projects. She has as well been assistant in the exercises of the courses on *Electromagnetics* I and II and *Antennas and Propagation*.

List of Publications

JOURNAL PAPERS

1. G. Quintero, J.F. Zürcher, and A.K. Skrivervik, "Planar elliptical differential antenna for UWB applications", in *Ultra-wideband, short-pulse electromagnetics 9*, Springer, 2010, accepted for publication.
2. G. Quintero, J.F. Zürcher, and A.K. Skrivervik, "System Fidelity Factor: A new method for comparing UWB antennas", *IEEE Transactions on Antennas and Propagation*, under review.

CONFERENCE PAPERS

1. G. Quintero, J.F. Zürcher, and A.K. Skrivervik, "Omnidirectional pulse dispersion of planar circular monopoles", *Proc. IEEE International Conference on Ultra-Wideband, ICUWB 2009*, Vancouver, Canada, Sept. 2009. pp. 395-399.
2. G. Quintero, J.F. Zürcher, and A.K. Skrivervik, "Impact of substrate permittivity on the performance of UWB monopoles'", *Proc. 3rd European Conference on Antennas and Propagation, Eucap2009*, Berlin, Germany, March 23-27, 2009. pp. 2567 - 2570
3. G. Quintero, and A.K. Skrivervik, "Analysis of planar UWB elliptical dipoles fed by a coplanar stripline", *Proc. IEEE International Conference on Ultra-Wideband, ICUWB 2008*, Hannover, Germany, Sept 2008 pp. 113-116.
4. G. Quintero, J.F. Zürcher, and A.K. Skrivervik, "Analysis of UWB antennas for carrier-based UWB impulse radio", *Proc. of the 2nd European Conference on Antennas and Propagation, EuCAP 2007*, Edinburgh, U.K., Nov. 11-16, 2007 , pp. 1-5, 2007.